Université Libre de Bruxelles

Faculté des Sciences
Département des Sciences de la Terre et de l'Environnement
Unité de Glaciologie

Marine ice formation in rifts of Antarctic ice shelves

A combined laboratory study and modeling approach

Ala Khazendar

Travail présenté en vue de l'obtention du
grade académique de Docteur en Sciences
Novembre 2000

16. 11. 2000

Université Libre de Bruxelles

Faculté des Sciences

Département des Sciences de la Terre et de l'Environnement

Unité de Glaciologie

Marine ice formation in rifts of Antarctic ice shelves

A combined laboratory study and modeling approach

Ala Khazendar

Travail présenté en vue de l'obtention du grade académique de Docteur en Sciences

Novembre 2000

To those who have offered me the passage from a world darkened by oppression and war to one of freedom and hope:

Henri Hurwitz

François de Kerchove

Jacques Peeters

Jean Salmon

Mayté Tassenoy

Ignace Van Steenberge

Contents

Acknowledgments

Recognition first goes to those who through the years I have become to identify collectively as the *trinity* of the Laboratory of Glaciology at the ULB: Professor Roland Souchez, Professor Regi Lorrain and Dr. Jean-Louis Tison (all questions regarding the holiness, or otherwise, of this particular trinity are strictly beyond the scope of this work).

I have the dubious privilege of probably being Prof. Souchez's last graduate student. The attention he has paid for my work and his unfailing support throughout my years in the laboratory went far beyond the traditional responsibilities of a thesis promoter. For that, he has my lasting gratitude.

I have enormously benefited from the tireless and definitely indispensable efforts of Prof. Lorrain which rendered the laboratory a place conducive to fruitful effort. His opinions, scientific or otherwise, were always sharp and to the point. His stoic comradeship through university cafeteria meals was much appreciated.

Because of his outstanding ideas and boundless energy, I am privileged to have had Dr. Tison as a mentor. His unyielding and continuous support was crucial for this work, not to mention that he is the one who had the foresight to collect the two ice cores used in this study at their locations, thus giving me the opportunity, when I later joined the laboratory, to work on what I found to be such an rewarding subject.

I am immensely indebted to Dr. Adrian Jenkins from the British Antarctic Survey. He patiently introduced me into the world of numerical modeling, and was always generous with his brilliant ideas during numerous discussions. While on visits to Cambridge, I was overwhelmed with his hospitality, which was augmented with the added opportunity of exploring his rather different taste in music.

The contributions of Dr. Michela Dini and Dr. Barbara Stenni are gladly acknowledged for having so willingly and diligently carried out the isotopic analyses for this study.

Madame Jaquie Haren and Madame Claire Lelouchier were always there for able help with laboratory and administrative work, interesting discussions and constant encouragement. For that I am very thankful.

The practical and moral support of Dr. Laurent Janssens, Ms. Véronique Verbeke and Ms. Suzanne Sleewaegen are much appreciated.

A. Khazendar

Chapter 1

Context

It is interesting to initiate this dissertation with the following pertinent quote from *Barrett* [1975]:

"Experience suggests that crevassed areas on ice shelves are worth closer examination. In the past they have been regarded as hazards to be avoided, but it is now evident that some crevasses have considerable scientific value as natural access ways to the sea beneath."

The current effort is indeed a closer examination of rifts and bottom crevasses in ice shelves, yet instead of merely exploiting them as access to the sea below, the investigation concentrates on processes taking place in the fractures themselves, processes of which the outcome could have significant effects on the ice shelves in which they occur and on the composition of the water that lies underneath.

1.1 Objective and definitions

The objective of this work is to demonstrate that, when certain conditions are available, rifts and bottom crevasses open in Antarctic ice shelves are filled, at least partially, with marine ice as a result of a local ice pump process.

Marine ice, or marine shelf ice, is a term that was introduced by *Oerter et al.* [1992] to designate a body of ice that forms at the base of an ice shelf as a result of the accumulation and subsequent consolidation of frazil ice crystals. Further information about marine ice is presented in section 1.1.1 below.

Frazil ice, according to *Daly* [1984], is fine spicule, plate or discoid crystals which form when heat is withdrawn from a turbulent body of water at its freezing point, thus rendering it supercooled.

An ice pump is the process by which ice in contact with ocean water is melted at depth and accreted higher in the water column due to the pressure-dependence of the freezing point. section 3.1 below is dedicated to a fuller description of this mechanism.

Rifts and bottom crevasses are fracture features that occur in ice shelves. The former are openings in the ice that span the entire thickness of an ice shelf while the latter are, using the words of *Jezek* [1984], fractures that extend upward into the base of a shelf.

The current study is concerned with rifts and bottom crevasses that have vertical extensions and widths of at least several tens of meters. The word cavity is often used during this work to describe, in a vertical cross section of a rift or bottom crevasse, the water-filled space enclosed between the two side walls of the fracture.

Fracture in Antarctic ice shelves is discussed in more detail in section 1.1.2 below.

1.1.1 Marine ice

The three-decade old quest to recover ice samples from the interface zone between an ice shelf and the ocean has led investigators down several paths. Work was first done on shallower and thus more accessible ice tongues. The objective of earlier efforts was to demonstrate that sea water must be directly freezing on to the base of ice tongues due to upward heat conduction through the ice. *Gow and Epstein* [1972] have provided the first conclusive verification of this assumption. Their work concerned ice cores up to 13 meters deep that had been drilled in the Koettlitz Ice Tongue, Antarctica. The same process, but on a much larger scale, was shown to take place beneath the Ross Ice Shelf by *Zotikov et al.*

[1980] where the bottom-most 6 meters of a 416-meter ice core were composed of frozen sea water. The estimated average freezing-on rate at this location was inferred by *Zotikov et al.* [1980] to be 2 cm per year, which was in good agreement with what *Robin* [1979] had already theoretically suggested for the Ross Ice Shelf. Another source of interface ice was identified when *Kipfstuhl et al.* [1992] and then *Warren et al.* [1993] established the basal ice shelf origin of green icebergs. The latter authors did not hypothesize on the formation mechanism of their green iceberg ice, but they did suggest the possibility that it had accreted at the base of the Amery Ice Shelf. This shelf was earlier the site of a 315-meter deep coring project of which the preliminary results were presented by *Morgan* [1972]. The lowermost 45 meters of this core, known as G1, was composed of what *Morgan* [1972] at the time considered to be freeze-on ice. However, the slow rate of this conduction-driven process made it inadequate to explain such thick accumulations of basal shelf ice. Hence, a second mechanism was introduced when *Robin* [1979] linked for the first time the formation of basal ice at G1 with water circulation patterns in the sub-shelf cavity. The theoretical elaboration of the process was made by *Lewis and Perkin* [1986] through their ice pump model. Later, *Engelhardt and Determann* [1987] explained how frazil ice crystals would form in thermohaline circulation and subsequently accrete to the bottom of an ice shelf and consolidate. Modeling of the process has been further improved in the recent years by several authors [e.g. *Hellmer and Jacobs*, 1992; *Determann and Gerdes*, 1994; *Jenkins and Bombosch*, 1995; *Bombosch and Jenkins*, 1995].

The number of available marine ice samples and cores still remains limited. This could be explained in part by the relatively recent interest in the subject. Then, there are the difficulties associated with the two possible sources of shelf basal marine ice samples. Green icebergs are rarely found in nature for the reasons discussed in *Warren et al.* [1993] and in *Grosfeld et al.* [1998]. These include the need for the accreted basal ice to survive any subsequent melting on its way to the front and for the iceberg containing it to capsize in order to reveal the green portion of its structure.

On the other hand, drilling for marine ice at the bottom of ice shelves is confronted with the obvious necessity of having first to penetrate hundreds of meters of meteoric ice. Other than G1, bottom ice accretion has also been found to form the lower 62 meters of the 215-meter core drilled in the Filchner-Ronne Ice Shelf at site B13 [*Oerter et al.*, 1992]. Another 320-meter core recovered further upstream from the same ice shelf at site B15 revealed the presence of a 167-meter thick accretion at the bottom [*Oerter et al.*, 1994].

Specific climatic conditions at certain locations in Antarctica give investigators the opportunity of circumventing this last difficulty by bringing a body of marine ice nearer to the surface as explained in section 2.1 below.

1.1.2 Fracture in ice shelves

A review of the available literature reveals that fracture in ice shelves is not yet an extensively researched topic.

Field observations: On a more general level, investigators have made attempts to relate the occurrence of surface fracture to the prevailing ice flow regimes, and the resulting fracture-inducing stresses, in the zones of ice shelves where rifts and crevasses exist. For example, *Barrett* [1975] explains the opening of a rift he discovered by the shearing and extension of the ice as it flows past the adjacent ice rise. *Swithinbank et al.* [1988] cite a work by *Robin* [1958] in which the latter author concludes that depressions in an ice shelf (and by extension, fractures) could form when diverging flow is too great to be accommodated by the spreading of the ice sheet in the normal course of thinning. On the other hand, *Hughes* [1983] gives examples of crevassing resulting from converging flows. Crevassing could also result at the zone of contact between fast and slow moving sectors of an ice shelf, as explained by *Barkov* [1986]. Such a process is probably at the origin of the highly fractured zone in the Nansen Ice Shelf discussed in the next chapter. A special case of this situation is the shear rupture occurring at the sides of valley glaciers or ice streams joining ice shelves. According to *Barkov* [1986], one such example is the extensive crevassing occurring at the junction between the Jutulstraumen Glacier and the Fimbulisen Ice Shelf, which includes a rift studied in more detail in section 5.1 below. Furthermore, rifts normal to the direction of ice flow near the front, such as the Grand Chasm in the Filchner Ice Shelf, which is discussed in section 5.5, could open as a result of the particular stress regime, analyzed by *Reeh* [1968], prevailing in the frontal region of the shelf. Such rifts are often precursors to calving events as discussed below.

Without exception, when the above investigators refer to the material existing in open rifts, they identify it as sea ice or as a heterogeneous mixture of sea ice, snow accumulations and/or broken fragments of the ice shelf. A good illustration is the account that *Stephenson and Zwally* [1989] give of a rift they observed in the West Ice Shelf where they have detected, using an altimeter, that the ice inside had a freeboard of ten meters. The authors attempt to explain such thickness by assuming that what is inside the rift is "very old" fast ice or that there has been appreciable snow accumulation.

While there is agreement on the fact that rifts start as crevasses in the ice shelf, there is disagreement on the sequence of events that leads to their formation. *Hughes* [1983] advances the idea that they result from the meeting of top and bottom crevasses. On the other hand, *Barkov* [1986] maintains that the majority of large and medium size rifts cut across the ice shelf from the upper surface to the lower. The theoretical model of *Rist* [1996], mentioned below, however, indicates that the opposite is much likely to occur, with bottom crevasses showing a greater tendency to extend upwards than their top counterparts do downwards.

As for bottom crevasses, *Jezek* [1984] explains that the basic process in their formation is related to the fact that below some depth, the pressure in sea water is always greater than the total stress in the ice shelf. Hence, water that penetrates the ice shelf through some preexisting imperfection will act as a wedge that tends to rupture the ice shelf up to a level where the magnitudes of the two stresses are equal.

Basal crevasses have also been observed on various occasions using radio sounding methods. Several authors, such as *Jezek* [1979] and *Shabtaie and Bentley* [1982], have detected them in the Ross Ice Shelf at numerous locations. *Orheim* [1986] observed many bottom crevasses in the Riiser-Larsen Ice Shelf.

Fracture processes in ice shelves have recently started to gain more attention because of the possible link between ice shelf stability on the one hand and potential disintegration through fracture on the other.

Thus, *Hughes* [1983] emphasizes the critical importance of fracture in ice shelf dynamics and its possible role in controlling the disintegration of ice shelves. A compelling case in point is presented by the work of *Doake and Vaughan* [1991] where a series of satellite photographs are used to reconstruct the sequence of events leading to the disintegration of the Wordie Ice Shelf between the years 1974 and 1989. The authors conclude that rifting was responsible for iceberg calving and the weakening of the central region of the ice shelf and the resulting retreat of the ice front. In another account of an important calving event, *Keys et al.* [1990] demonstrate how rifts controlled the calving of the huge B-9 iceberg (154 by 35 kilometers) in 1987 at the eastern part of the Ross Ice Shelf front. A major calving event at the location of these rifts had earlier been predicted by *Shabtaie and Bentley* [1982].

Of great interest to the current work is the role *Doake and Vaughan* [1991] ascribe to the ice filling the rifts as "glue" that could hold ice shelf blocks together. *Stephenson and Zwally* [1989] make a comparable remark when they suggest that "sea ice" within rifts may play a stabilizing role by restraining calving and acting as a "cement" for fractured ice. This topic is further pursued in the theoretical work section below.

One obvious but important implication of the above discussion is how widespread and general the presence of rifts and basal crevasses in Antarctic ice shelves is. Other examples are discussed in more detail in chapter 5.

Theoretical work: The relationship between fracture and calving acquires still more importance, including for general mass balance considerations, when realizing that up to 90% of mass loss in Antarctica is through calving, according to the estimates of *Reeh* [1968]. The more recent discussion by *Paterson* [1994] underlines the difficulty of quantifying this process. Nevertheless, the data compiled by the author from different sources suggest that iceberg calving accounts for 80 to 88% of the total Antarctic mass ablation.

Hence, the attention of investigators has turned to the study of the conditions under which a small initial crack in an ice shelf would propagate to form a much larger fracture, such as a rift or basal crevasse, under the effect of tensile stress.

Vaughan [1993] follows a phenomenological approach by which he attempts to derive a relationship between measurements of strain rates (converted to stresses using a creep law) and observations of the presence or absence of crevassing on the surface of ice masses, including ice shelves.

Concerning ice shelves in particular, *Rist* [1996] applies a two-dimensional fracture mechanics model in a vertical plane to predict the extent of surface or bottom crevasse penetration under different stress regimes.

Rist et al. [1999], on the other hand, combines theoretical and experimental approaches to find a fracture propagation criterion applicable to the occurrence of crevassing in the surface plane of an ice shelf. The authors found that the criterion in question depends on the size of the initial crack, the nature of the applied stress field and the properties of the ice. The latter parameter was evaluated by the authors through laboratory experiments on ice samples recovered from the Ronne Ice shelf.

All of the above-cited theoretical work assumes the initial existence of a crack in the ice. *Rist et al.* [1999] suggest that surface melt water, percolating through the upper firn, could refreeze and expand causing the ice to fracture locally thus creating sharp flaws with the minimum size necessary for propagation predicted by their model. Nothing could be found in the literature as to how the initial cracks at the bottom of an ice shelf could form.

Very pertinent to the question of ice in open rifts is the recent work of *Rignot and MacAyeal* [1998] and *MacAyeal et al.* [1998] which, as they state, reveals for the first time the role of ice in rifts as a binding agent in a fractured ice shelf. These investigators use a series of synthetic aperture radar satellite images to construct interferograms of two calving front locations of the Ronne Ice Shelf. They also compare the real interferograms with others generated by a finite-element ice shelf flow model in their effort to assess the effect of what they call the "ice melange" filling the rifts near the ice front. For the authors, this melange is a heterogeneous mixture of multiyear sea ice, ice shelf fragments and wind-blown snow. In conclusion, *Rignot and MacAyeal* [1998] and *MacAyeal et al.* [1998] strongly emphasize the fact that the ice melange tends to deform coherently in reaction to the flow of the ice shelf and that it has sufficient mechanical strength and integrity to bind large tabular ice shelf fragments to the coast. The authors speculate that it is through the melting of the ice melange that the oceanic and atmospheric environments can control, in part at least, the location of

Antarctica's ice shelf calving fronts. The authors expect that the nearer a rift gets to the front, the more melting takes place and the weaker and thinner the ice melange in the rift becomes as a prelude for calving. Interestingly, their interferograms do not show any such weakness of the melange near the front of the ice shelf. One reason that the authors advance to explain such discrepancy is the possibility of other processes being active, processes they did not consider in their analysis.

1.2 Method

The realization of the objective set above is pursued on two complementary paths. The first approach consists of laboratory analysis of ice samples from the field. Three parameters are considered: crystallography, salinity and isotopic composition. Ice properties thus revealed are sufficient to distinguish, without ambiguity, marine ice from meteoric (continental) ice on the one hand and sea ice on the other.

The second approach is that of mathematical modeling which also concentrates on three parameters: the temperature and salinity of the water in the cavity and the thickness of the ice supposed to be forming in it. These are the quantities which are relatively easier to measure during field work.

1.3 Plan

After delineating the general scope of this work in the first chapter, the results of the laboratory study examined in the second chapter serve to establish the presence of marine ice in rifts and basal crevasses. The process hypothesized to be at the source of this presence, the local ice pump and frazil accumulation, is modeled in chapter three. The fourth chapter examines the conditions necessary for this presence to occur. These conditions, which are the ones referred to in the objective statement above, mainly concern the spatial dimensions of the cavity and the temperature and salinity of the water filling it. The fifth chapter is an area of intersection. Field observations from the literature presented in it serve to support the conclusions of the second chapter while providing the material to apply the model constructed in the third and fourth. General conclusions are drawn in chapter six where the possible implications of this work are summarized.

Chapter 2

Field investigation and laboratory study

The place of this chapter in the overall structure of the current work is crucial. In it, a combination of field observations, laboratory analyses results and comparisons with pertinent published findings permit the formulation of the main hypothesis of this work on solid grounds. This confidence paves the way for the modeling work that follows and helps in explaining or reinterpreting other field observations that could be found in the literature in the light of the new findings of this work.

As part of the 1995-1996 Belgo-Italian collaboration program, two 45-meter ice cores were collected from an area of marine ice of the Nansen Ice Shelf (NIS), which is misleadingly identified as an ice sheet on standard maps. Each core had a diameter of 8cm. The lengths of the NIS cores are comparable to the marine ice segments of both the G1 and B13 cores as can be seen from Table 2.1. The same table provides other information about cores G1, B13 and B15 to which repeated reference is made in the following discussion.

	Ice shelf	*core location*	*coordinates*	*length of marine ice segment*
NIS1	Nansen	7.5km from grounding line	74°51'S, 162°50'E	45m
NIS2	Nansen	24.5km from grounding line	75°00'S, 163°06'E	45m
B13	Ronne	30km from front	76°58'S, 52°16'W	62m
B15	Ronne	180km from front	77°56'S, 55°56'W	167m
G1	Amery	68km from front	not given	45m

Table 2.1: Basic site and size information about the marine ice cores being considered for comparison in this study. The data for B13 and B15 comes from *Oerter et al.* [1994] while the G1 core is described by *Morgan* [1972].

The sections below present the results of high resolution multiparametric measurements showing that the properties of the entire core correspond to the expected profile of marine ice. It is believed that this is the first time that a core of marine ice, with a formation site so relatively near to the grounding line, has been directly collected from the surface of an ice shelf. More importantly, the core's proximity to the grounding line and its specific ice properties prompt the proposal that the accretion of marine ice in basal crevasses or rifts opening where meteoric continental ice gets afloat is an active and previously undocumented process.

2.1 Setting

The Nansen Ice Shelf is located in Victoria Land, East Antarctica as can be seen in Figure 2.1. Its grounding line is thought to be situated beneath the highly

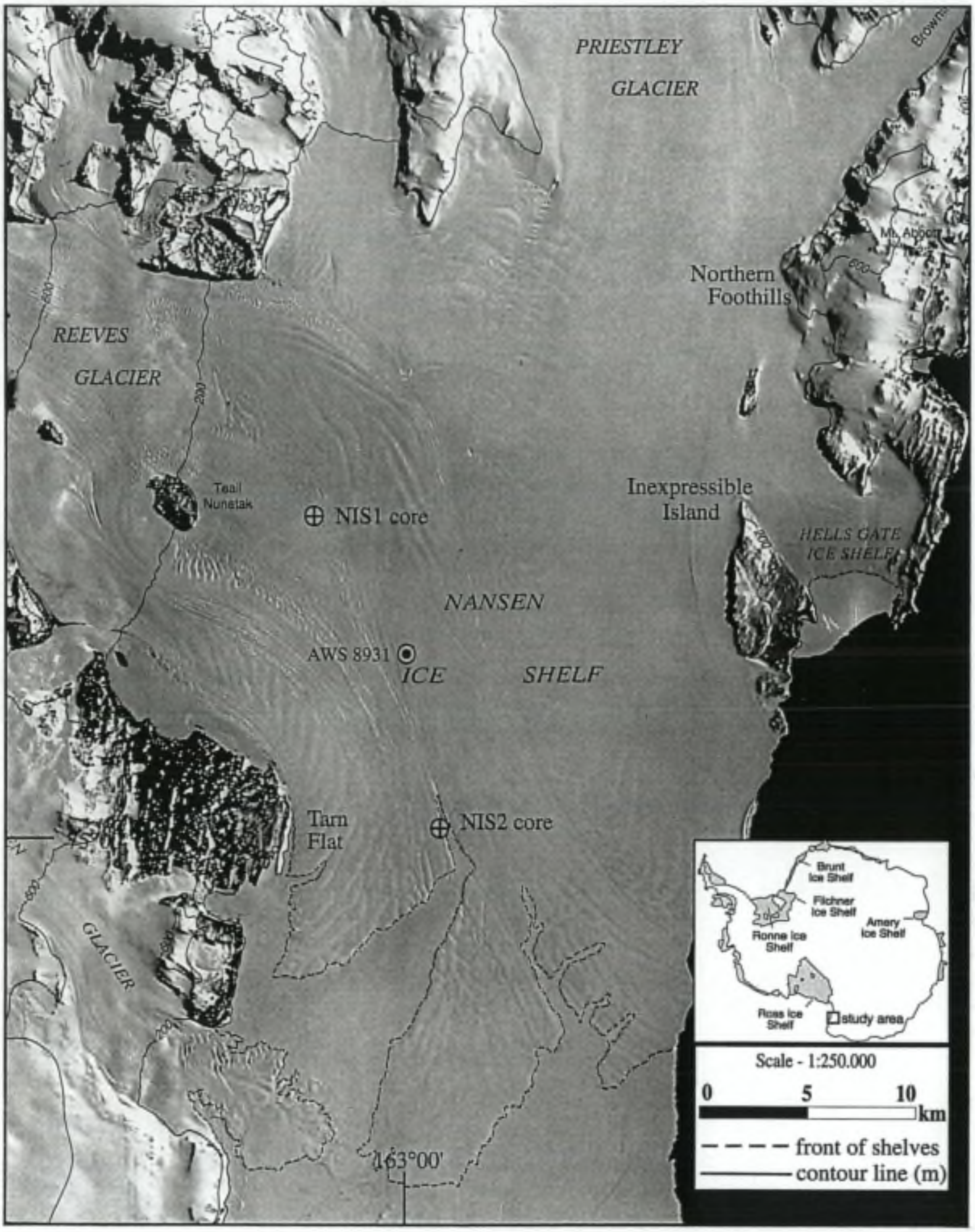

Figure 2.1: Map of the Nansen Ice Shelf showing the main surface features, the location of the drilling sites and that of meteorological station AWS 8931. Background satellite image is taken from *Borfecchia and Frezzotti* [1991].

crevassed area near the point where Teall Nunatak emerges out of the Reeves glacier. Figure 2.2 shows a photograph of that zone.

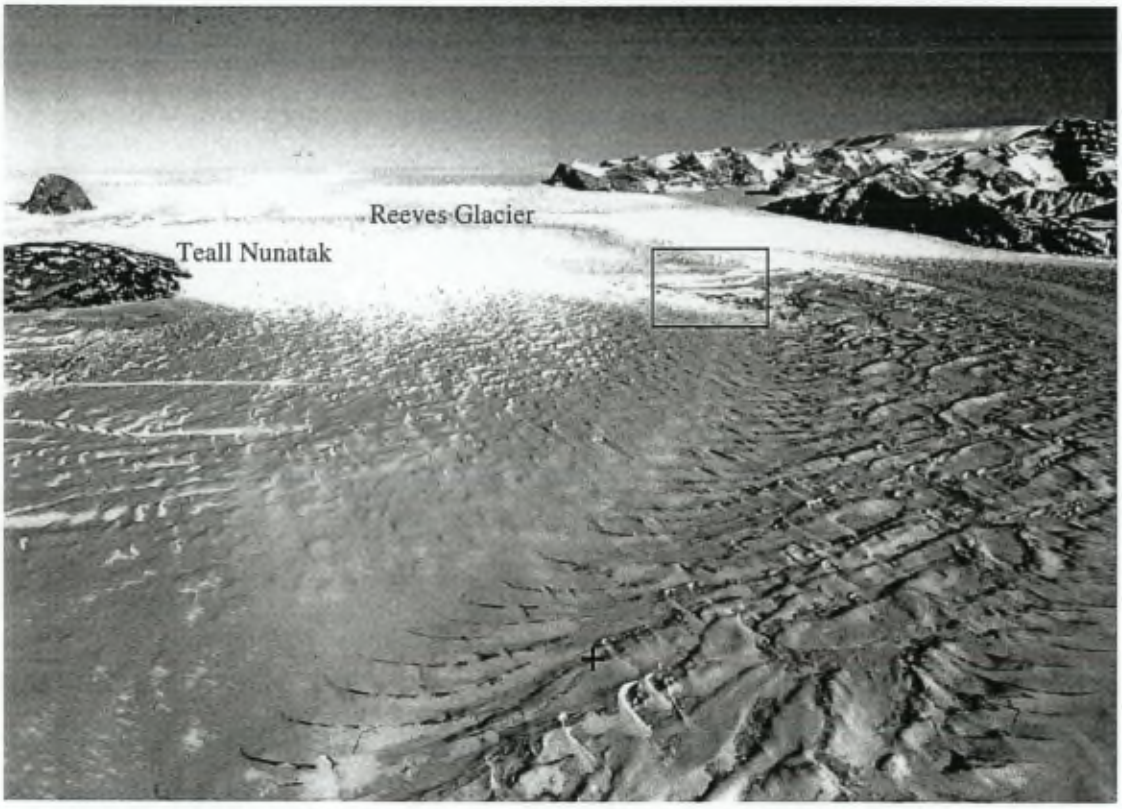

Figure 2.2: An aerial photograph of the NIS1 core site which is marked by the symbol +. The core was taken in one of the marine ice outcrops. These appear on the surface of the ice shelf, distinguished by their crescent-shaped dark forms, in a series that extend all the way to the grounding zone. At that point, the rectangle indicates the area shown in more detail in Figure 2.3 below (photograph by J.-L. Tison, 1996).

From that point the shelf flows out into Terra Nova Bay for about 35 km to the front and is about 25 km across between Tarn Flat and Inexpressible Island. These two bedrock features together with the Northern Foothills laterally constrain the flow. In addition to crevasses, rifts have opened near the grounding line. Some contain "islands" of continental ice chunks that have been frozen in place by the surrounding sea/marine ice (Figure 2.3).

The development of this fracture zone coincides with the occurrence of velocity contrasts among the different streams that feed the ice shelf. This velocity difference is thought by *Frezzotti* [1993] to be related to the friction of the ice shelf against Tarn Flat and Inexpressible Island and to the slopes on the ice surface of the portions fed by the Reeves Glacier (3 m/km) and the Priestley Glacier (2 m/km).

Figure 2.3: A detailed aerial photograph of part of the grounding zone (delineated by a rectangle in Figure 2.2 Above) of the Nansen Ice Shelf. Notice the high degree of fracture which results in several detached pieces of the continental ice being frozen in place by sea/marine ice (photograph by J.-L. Tison, 1996).

Typical ice flow horizontal velocities in the vicinity of the core site were measured by *Frezzotti* [1992] to be about 160 m/yr. In the same paper, the author estimates that the ice shelf covers an area of approximately 1800 km^2. *Frezzotti* [personal communication, 1998] puts the total thickness of the ice shelf at the grounding line at about 600 meters, with no error estimate given on this last figure. Therefore, by Antarctic standards, Nansen could be considered as a small to medium-sized ice shelf.

A first core, which henceforth is designated as NIS1, was taken at coordinates 74°51'S, 162°50'E as close as was logistically possible to the grounding line, about 7.5 km downstream from it. A second core, designated as NIS2, was taken at location 75°00'S, 163°06'E to the northeast of the first one about 17km further downstream.

These two positions were chosen in ice outcrops shown to be of sea water origin by preliminary tests carried on surface samples.

The phenomenon of lower strata of an ice shelf finding their way to the surface due to high ablation rates was first demonstrated in the work of *Gow and Epstein* [1972]. *Souchez et al.* [1991] have invoked such a process to explain the marine ice nature of certain frontal sections of the Hells Gate Ice Shelf (HGIS) in the Terra Nova Bay area. Mass loss at the surface of an ice shelf could be induced either by melting and drainage or sublimation. The latter process is the one most likely to be prevalent in the NIS situation due to the intense and frequent katabatic wind activity. Wind velocity measurements are available from the weather station AWS 8931 (PAT) which is nearest to the core site at coordinates 74°53'S, 163°00'E as can be seen in Figure 2.1. For the years 1989 and 1990, 41.2% of the wind blew from the southwest, the direction of the Antarctic plateau, with wind speeds exceeding 28 knots for more than 39% of the time [*Baroni*, 1996]. This has undoubtedly participated in enhancing the surface ablation rates in the area estimated by Frezzotti [1992] to be around 20-30 cm/yr.

2.2 Investigated parameters and analytical treatment

Traditionally, the three principal parameters used to establish the marine basal shelf identity of a body of ice are crystallography, salinity, and stable isotopes.

All work on the ice cores was done in a cold room kept at -25 °C in the Laboratory of Glaciology of the University of Brussels. Vertical thin sections 7 to 10 cm long were continuously prepared along the entire 45 meters of core length. Sampling for salinity measurements was done at the same frequency. This high sampling rate has never been attempted on previous marine ice core studies, as can be seen from Table 2.2, and it insures a much enhanced insight into the variability with depth of the ice properties and a better chance of detecting any interceding layers of different properties/origin.

	crystallography	*conductivity*	$\delta^{18}O$
NIS1	7-10cm	7-10cm	45cm on av.
NIS2	7-10cm	7-10cm	90cm on av.
B13/B15	1000 cm on av. (+8 thin sections at close spacing & 15 vertical sections for B13)	80cm on av.	not given
G1	was not performed	not given	4 samples

Table 2.2: A comparative look at the resolution of the different measurements carried out on the ice cores being compared in this study. Information on B13m B15 and G1 concerns only their marine ice segments. Data on the former two cores come from *Oerter et al.* [1992], *Eicken et al.* [1994] and *Oerter et al.* [1994] while the G1 core is described by *Morgan* [1972].

The manner in which a piece of ice core was cut is shown in the schematic diagram of Figure 2.4. While treating the ice cores, a certain thickness is lost each time a piece of ice is cut into two as a result of the saw's blade action. A test was performed and the lost thickness was calculated to have an average value of 0.115cm. This has been taken into consideration when plotting parameter profiles with depth.

2.2.1 Crystallography

Crystallographic texture of the ice cores was revealed by preparing thin sections of the ice then viewing and photographing them between crossed polarizers.
The crystal sizes of the two cores were calculated using the linear intercept method, described by *Tison et al.* [1994], which consists of measuring the length of a horizontal traverse across the photograph of each thin section and then dividing it by the number of crystals in the traverse.
Optical properties of ice underlie the possibility of using polarized light to study crystal shapes and orientations. Ice crystals are optically anisotropic, since an incoming light beam will be split into two waves traveling with different, direction-dependent, velocities through the ice lattice.

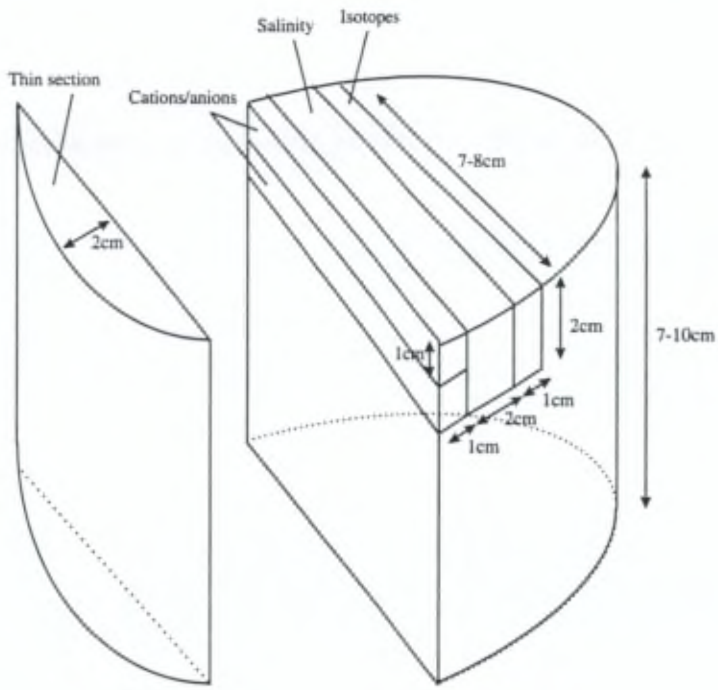

Figure 2.4: The sizes and relative positions of the different ice samples cut from a typical piece of ice core. Each sample is identified by the type of test or manipulation for which it is destined. The diagram shows that samples were also cut for future major cation and anion analysis.

The electric vector of one of the waves will be vibrating along the optic axis of the crystal, the only axis along which the velocities of the two waves are equal, while that of the other wave will be vibrating perpendicular to the axis. Due to their different travel velocities, the two waves will be out of phase when they emerge from the crystal. Hence, if the original beam of light had been polarized in a certain direction, the resultant electric vector of the emerging waves will generally vibrate in a direction inclined to the original polarization direction. Observing this light through a polarizer oriented perpendicularly to the direction of the original filter will block all background light but not the light that passed through the ice crystals. The latter light succeeds in passing because its electric vector has at least a component parallel to the direction of the second polarizer [e.g. *Hobbs*, 1974].

Once crystal shapes and sizes are revealed by the above method, the crystalline structure can then be assessed in terms of the available classifications of sea and marine ice crystallographic types. The relatively recent development of marine ice research meant that investigators borrowed the more established terminology of sea ice. This lead to a degree of confusion concerning terminology and its significance. *Tison et al.* [1998] attempt to address this question by compiling and categorizing the sea and marine ice facies available to date. The authors use the term granular to distinguish a group of facies from the columnar crystalline structure associated with congelation ice. One sub-category of the granular group is a facies known as orbicular, which *Tison et al.* [1998] identify to be of frazil ice origin. According to the photographic examples provided by the authors, the rather rounded shapes of orbicular crystals are easy to distinguish from the angular boundaries characterizing the other sub-category of the granular group known as polygonal. The latter crystal type, when its crystals are not interlocking, is attributed a snow ice origin.

2.2.2 Salinity

Solutions such as sea water reject most of their salt content upon freezing [e.g. *Ozum and Kirwan*, 1976; *Gross et al.*, 1977]. This is because sea water contains very few ions that satisfy the conditions necessary to replace a water molecule and thus be incorporated into the lattice of an ice crystal. According to *Weeks and Ackley* [1982], these conditions are for the ion to possess the right size to fit into the ice lattice, the tendency to form a similar type of chemical bond and an appropriate charge to maintain electrostatic neutrality.

Nevertheless, research on sea ice, which forms, in part at least, as a result of the advancement of freezing front in the ocean, reveals that new sea ice could have a salinity of up to several parts per thousand. The established explanation for this is the process known as constitutional supercooling [e.g. *Lock*, 1990] which originates from the changing composition of the layer adjacent to the ice/water interface as rejected salt accumulates in it. The result is that the interface develops dendritic or cellular morphology, thus bulk entrapment of brine within the growing ice takes place.

Marine ice, which has much lower salinities compared to sea ice, is hypothesized to be forming from the accumulation of frazil crystals in a body of host water and their subsequent consolidation. No published work could be found where the question of the salinity of frazil crystals forming in ocean water is directly addressed. However, investigators seem to accept that the crystals are almost completely desalinated upon their formation [e.g. *Hanley and Tsang*, 1984; *Eicken*, 1998; *Bombosch*, 1998]. Therefore, the salinity of marine ice must be originating from brine entrapped between the crystals during the consolidation process.

The post-genetic mechanisms for desalinating sea ice proposed by *Untersteiner* [1968], such as gravity drainage and brine migration or expulsion, were shown by *Eicken et al.* [1994] to be insufficient to explain the relatively very low salinities of marine ice.

At present, the widely accepted practice is to use the electrical (or electrolytic) conductivity to obtain a quantitative measure of the salinity of an aqueous solution such as sea water or the melt of sea or marine ice. Ions of electrolytes such as NaCl or $CaSO_4$ are separated and hydrated when dissolved in water. The presence of ions in the water gives it the ability to conduct electricity, an ability which is proportional to its ionic content, or salinity. Other than the concentration, the conductivity of a solution depends on the mobility of the ions present in it. The mobility of ions, in turn, depends on factors specific to the types of solute and solvent involved, and one important external factor, the temperature [*Boltz*, 1952]. The higher the temperature of the sample, the greater its conductivity becomes (approximately, 2 percent change in conductivity for each 1°C); whence the importance of correcting for temperature variations during measurements.

In the current study, salinity was obtained by measuring the electrical conductivity of ice samples that had been melted at room temperature. Sampling for the measurements was done at the same frequency as for the thin sections, by cutting, at positions corresponding to the top 2cm of each thin section, a 1.5cm-thick and 8cm-long piece of ice necessary to produce about 15 ml of melt water.

Conductivity was then measured with a *Tacussel CD810* conductimeter used with probe *XE110* (cell constant = 2.01 cm). During the conductivity measurements, the temperature of the melted samples was stabilized at 25.00°C by submerging their containers in a thermal bath. Since the temperature was not allowed to deviate in either direction by more than 0.09°C, the biggest error source was the error on the conductivity of the standard KCl solution used for calibrating the cell. Therefore, we estimate the error on the conductivity readings to be around ±2.5%.

Salinity values were obtained from the conductivity measurements by using a calibration curve based on 40 samples of known salinity. These samples, which had a salinities between 0.02 and 0.30, where obtained by the dilution of an IAPSO (International Association for the Physical Sciences of the Oceans) sea water standard 10L-series provided by *Ocean Scientific International*.

Salinities from the other marine ice studies cited in this work are reported in conductivity units; hence, when making comparisons, the results of the NIS cores will be reported directly in terms of conductivity. Such a comparison is made possible by the fact that conductivities of the B13 and B15 core samples are provided by *Eicken et al.* [1994] and *Oerter et al.* [1994] corrected to 25°C.

In the past, salinities used to be reported using units of per mil. The origin of this practice was the perception of salinity as the grams of dissolved salts per one kilogram of sea water. Then, with the adoption, in 1981, of the Practical Salinity Scale by the Joint Panel on Oceanographic Tables and Standards for general oceanographic use [*Fofonoff and Millard*, 1983] investigators started employing the so called practical salinity units, or psu. However, a later report by the Joint Panel on Oceanographic Tables and Standards [*UNESCO*, 1985] stipulated that in the Practical Salinity Scale, salinity has no units since it is a pure ratio. The ratio in question being that of the electrical conductivity of the sample to the conductivity of a standard solution. This recommendation is now adopted by all international organisms related to oceanography and it is adhered to in this work. Therefore, throughout this work, salinity is reported without units, except in very few places where lack of clarity could result from the absence of a unit.

2.2.3 Stable isotope composition

The magnitude of the phenomenon of isotopic fractionation during chemical or physical processes in nature is proportional to the relative mass difference between isotopes. Therefore, the largest and most interesting naturally occurring isotopic variations are restricted to the light elements [*Bowen*, 1991]. This category of elements contains the two components of the water molecule: hydrogen and oxygen. When water freezes, the resulting ice is enriched in the heavier isotopes of each of the two elements. For the purposes of the current study, sample isotopic content of oxygen is analyzed.

Faure [1977] explains that isotopic fractionation is the consequence of the fact that molecules containing different isotopes of an element in equivalent positions have different energies because of differences in the vibrational components that are mass dependent. A given molecule that contains the lighter of two isotopes has a higher vibrational frequency; thus the bonds it forms are weaker and more easily broken, making such a molecule more reactive than the heavier one.

In marine ice studies so far, the oxygen isotopic content is investigated by considering the ratio of the two most abundant isotopes of this element, namely, $^{18}O/^{16}O$. However, as described by *Clark and Fritz* [1997], measuring an absolute isotopic ratio or abundance is quite complicated and the results of different studies are not easily comparable. Alternatively, what is actually measured is the variations in stable isotope concentrations relative to a certain known reference. This becomes clearer when the so-called delta notation is used which is expressed as:

$$\delta^{18}O_{sample} = \left(\frac{(^{18}O/^{16}O)_{sample} - (^{18}O/^{16}O)_{reference}}{(^{18}O/^{16}O)_{reference}} \right) \cdot 1000 .$$

Since differences due to fractionation are small, they are expressed as parts per thousand, or per mil, which explains the multiplication by 1000 in the above equation.

At present, the internationally accepted reference water, which is also used in the measurements done for this study, is the so called V-SMOW which stands for Vienna Standard Mean Ocean Water. *Bowen* [1991] describes it as hypothetical water of which the composition is close to that of average ocean water and gives the value of its oxygen isotopic ratio as: $(^{18}O/^{16}O)_{V\text{-}SMOW} = (2005.20 \pm 0.45)E\text{-}6$. *Clark and Fritz* [1997] draw attention to the fact that this value is different from that of an older standard water that was in use and which is simply known as SMOW.

Stable isotopes signatures ($\delta^{18}O$ or δD, which is the symbol of deuterium, a heavy isotope of hydrogen) of marine ice have been investigated by several authors [*Morgan*, 1972; *Oerter et al.*, 1992; *Souchez et al.*, 1991; *Tison et al.*, 1993; *Tison et al.*, 1998]. It shows a narrow range of values, which was generally interpreted as the expression, in the frazil ice crystal, of near-equilibrium fractionation from sea water, sometimes slightly modified by glacial meltwater [*Morgan*, 1972; *Oerter et al.*, 1992]. However, even in such a narrow range of values, the variations were significant enough to be used by *Souchez et al.* [1991], *Tison et al.* [1993] and *Tison et al.* [1998] to demonstrate the transfer of marine ice along the ice shelf flow line and to interpret seasonal variations in landfast sea ice forming in front of the Hells Gate Ice Shelf in Terra Nova Bay, Antarctica. Other glaciological applications of the stable isotope method are thoroughly discussed in *Souchez and Lorrain* [1991].

Mass spectrometry analysis of the oxygen isotope composition relative to V-SMOW was carried out in the Laboratory of Isotopic Geochemistry of the University of Trieste, using a *Finnigan Delta-S* mass spectrometer, on 99 samples of NIS1 and 50 samples of NIS2. Sampling was more or less regularly performed along each core's length and guided in part by the salinity results. Measurement accuracy is $\pm$ 0.05 per mil.

2.3 Evidence

This section presents the results of the analyses outlined above. Comparisons with the properties of the other cores are concerned exclusively with the marine ice sections of these cores.

2.3.1 Crystallography

The crystalline structure revealed by the thin sections is conspicuous by its complete lack of bubbles, which, for Antarctic shelf ice, is a strong indication of its non-continental origin. Following the scheme outlined by *Tison et al.* [1998] for the classification of marine ice types, two sub-categories can be used to describe most of the facies exhibited by the crystals of the NIS cores. A first facies, which is attributed a frazil ice origin, is made of small equigranular crystals with rounded boundaries that could therefore be identified as granular orbicular (Figure 2.5).

Figure 2.5: A representative thin section from the NIS1 ice core showing the rather heterogeneous sizes of the dominant orbicular facies. The top of this particular thin section is located at 30.34 meters below the surface (sample 83.b).

One of the mechanisms listed by *Weeks and Ackley* [1982] for the formation of frazil ice is the adiabatic drop in pressure of rising water which occurs in the Deep Thermohaline Circulation processes described above. Cores B13 [*Oerter et al.*, 1992] and B15 [*Oerter et al.*, 1994] also exhibit a granular facies, but some of the crystals show polygonal interlocking structure. According to *Eicken et al.*

[1994], this is probably inherited from the specific time/temperature growth history of the ice crystals as they accrete at the bottom of the ice shelf.

The second facies, which has not been reported for these other cores, is known by *Tison et al.* [1998] as string-lined and presents a striking feature of the NIS cores. Grains belonging to this latter category are noticeable for their elongation which shows a clear preference to occur in a vertical or near-vertical direction. Most of these crystals have a distinct rectangular aspect with an elongation factor of 2.5 to 6 and appear in thin sections throughout the cores (Figure 2.6b and 2.6d), more so in NIS1 than in NIS2. This is in complete opposition to what has been observed in the B13 core. *Eicken et al.* [1994] describe how most grains in the top part of B13 are elongated in a horizontal direction and how this elongation tends to disappear with depth. The occurrence of the string-lined facies in the NIS cores is often accompanied by clear small scale folding that has a wave length and an amplitude both of the order of 4cm (Figure 2.6a). Folding is much more prevalent in NIS1 where it tends to be absent from the core segment between 17 and 27 meters depth.

Few thin sections are observed to exclusively contain one of the facies and for the most part the two facies are observed together in different proportions. Crystal size profiles with depth are plotted in Figures 2.7a and 2.7b, which show that both cores exhibit similar crystal size ranges. The mean NIS core crystal breadth is 1.7mm. If a rounded approximation were to be used, the corresponding average crystal cross sectional area would be 2.7mm^2. This value is distinctly lower than those reported for the marine ice sections of the other cores. While crystal cross sectional areas were not mentioned for G1, *Oerter et al.* [1994] report values that vary mostly between 5 and 60mm^2 for B13 and B15 crystals. Furthermore, with most NIS crystals having cross sectional areas fluctuating between 1.1 and 3.8mm^2, they also exhibit a much more confined range than that of B13 and B15. On the other hand, NIS1 core crystal size does show a slight trend of growing with increasing depth as manifested by the smoothed (11-point running mean) profile of Figure 2.7a. The B13 core [*Eicken et al.*, 1994] shows a similar, albeit much more pronounced, general behavior.

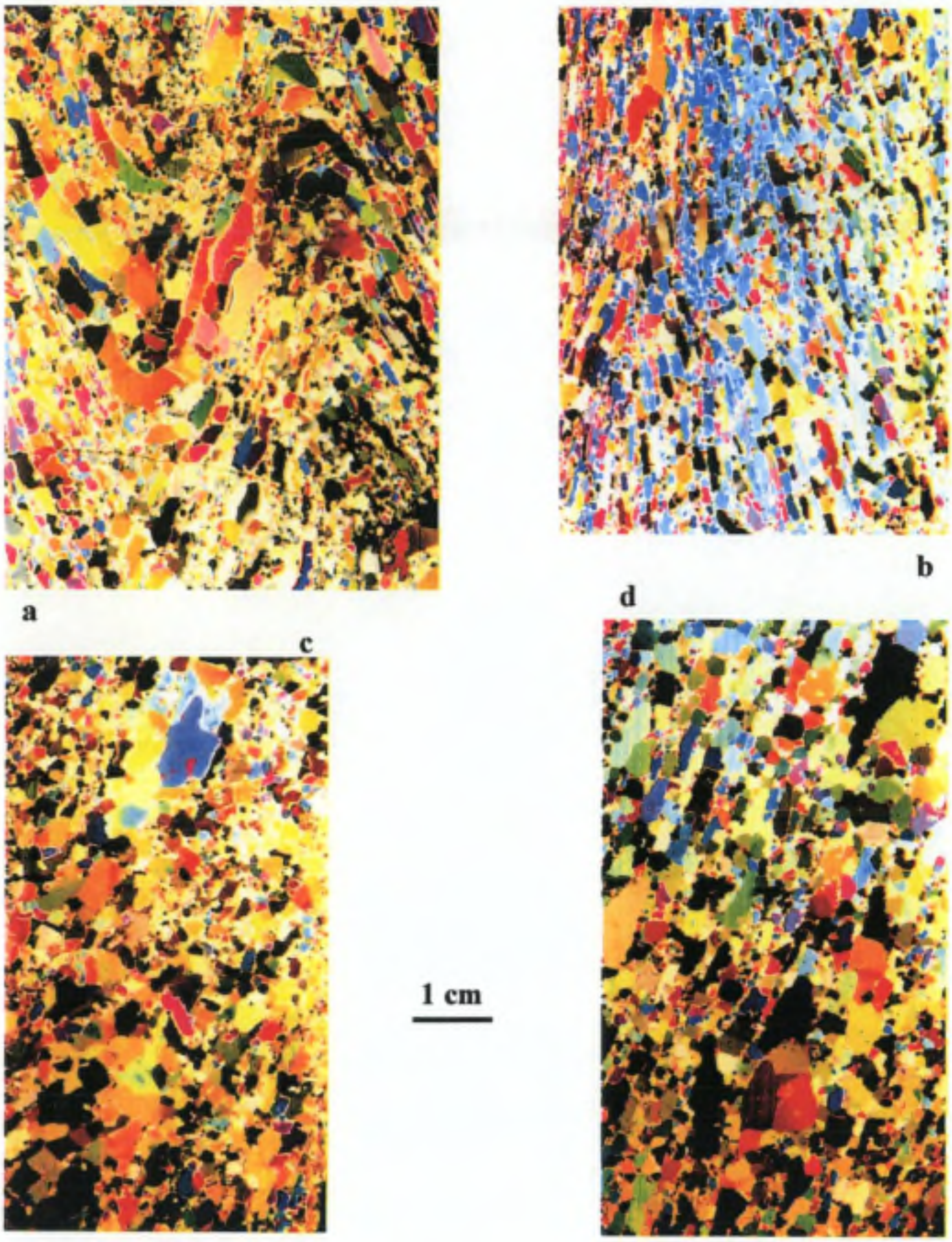

Figure 2.6: Examples of crystalline texture and structure. (a) Thin section, of which the top is located at 42.84 meters depth of NIS1 (sample 118.b), shows a remarkable example of small-scale folding. (b) String-lined facies from 16.56 meters depth of NIS1 (sample 44.e). Notice the vertical alignment of the crystals. (c) A typical thin section from 39.49 meters depth of NIS2 (sample 102.e) showing granular orbicular facies. (d) Another example from NIS2 (sample 79.c at 30.49 meters depth) clearly showing crystals elongated in a near-vertical direction.

Most debris in the NIS cores appear either as particle aggregates or layers. There is no clear pattern for the distribution of debris with depth in either core.

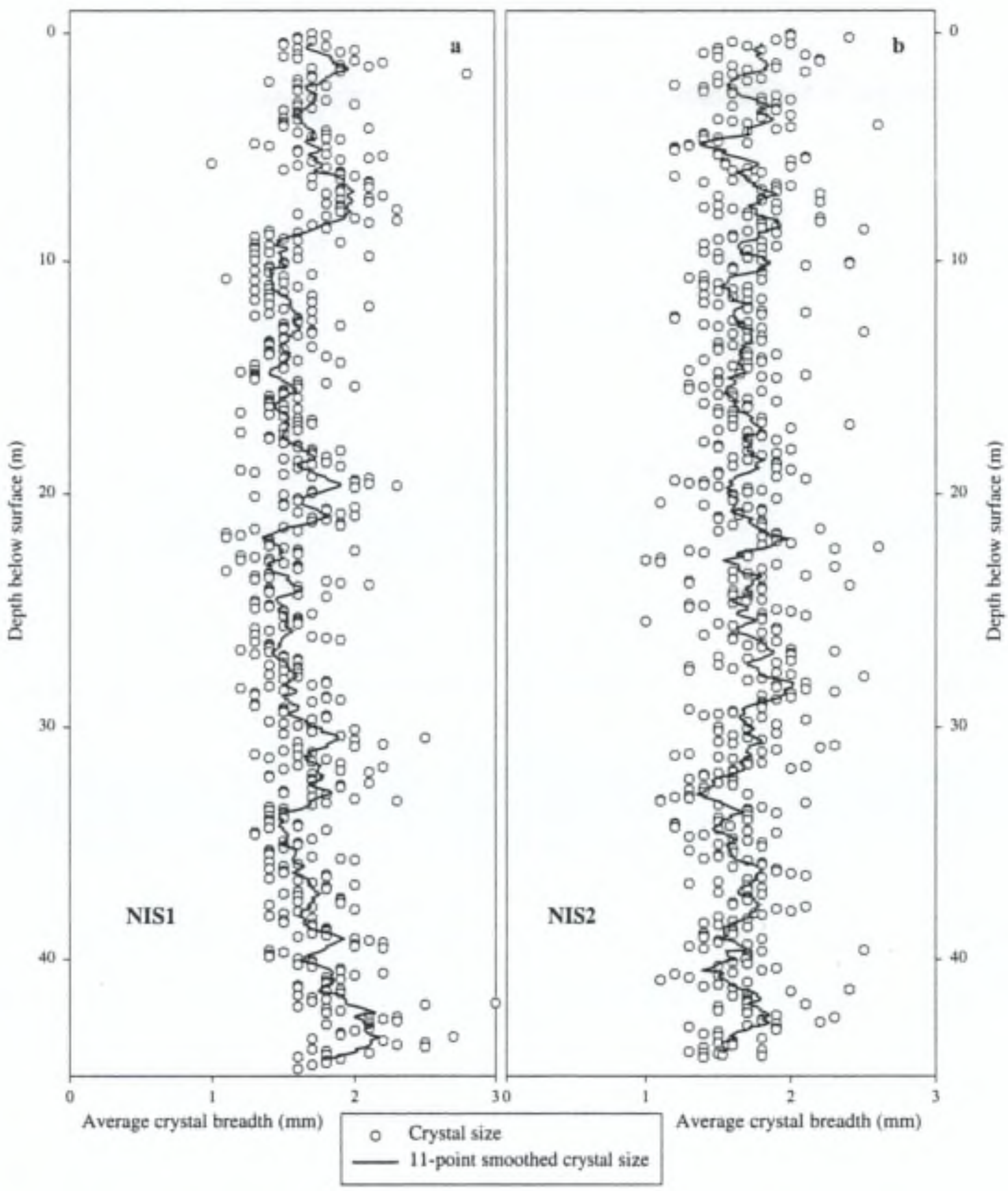

Figure 2.7: Profiles of the average crystal size with depth in (a) the NIS1 and (b) NIS2 cores. In both plots, the solid line represents a 11-point running mean.

While debris occur more frequently in NIS1, folded debris layers appear almost exclusively in NIS2. They have a higher density of particles and are concentrated between the depths of 31 and 34m. Perhaps the most notable difference between the NIS cores and B13 is the orientation of the debris layers. While the inclusions are arranged into horizontal strings and layers in B13 [*Eicken et al.*, 1994], none of the layers in NIS2 is horizontal.

2.3.2 Salinity

Both the quantitative values and the general qualitative behavior of the resulting conductivity profiles with depth conform with those of marine ice. As can be seen from Figures 2.8a and 2.8b, most conductivity readings are clustered in the interval between 80μS/cm (0.035 salinity) and 300μS/cm (0.145 salinity) for NIS1 and between 80μS/cm and 550μS/cm (0.270 salinity) for NIS2. These values are considerably lower than typical sea ice salinities which extend between 3 and 25 [*Weeks and Ackley*, 1982]. Even congelation ice which is thought to have formed beneath the Ross Ice Shelf does not exhibit any salinities below 2 [*Zotikov et al.*, 1980].

On the other hand, the NIS conductivity results do overlap the ranges of 40 to 200μS/cm for B13 [*Oerter et al.*, 1992] and 100 to 210μS/cm for G1 [*Morgan*, 1972]. Furthermore, the general trend of decreasing salinity with increasing depth echoes what has been observed in the above-cited studies. This can be seen from the profiles of Figures 2.8a and 2.8b. On the other hand, it should be noted that the NIS cores, with a maximum measured conductivity of 390μS/cm for NIS1 and 686μS/cm for NIS2, generally exhibits higher salinities than B13 and G1. The B15 core does show, at the top 0.4 meter of its marine ice section, conductivity values as high as 390μS/cm [*Oerter et al.*, 1994], but interaction with particle inclusions abundant in these layers could have occurred. Moreover, its conductivity profile rapidly drops back to a baseline value of around 40μS/cm similar to that of B13 [*Oerter et al.*, 1994]. The NIS cores, on the other hand, have a conductivity baseline value that falls from around 140μS/cm to 90μS/cm with increasing depth (Figures 2.8a and 2.8b). However, significant deviations from the baseline of the salinity/conductivity signal occur as "bumps", each extending over a few meters of depth along each profile.

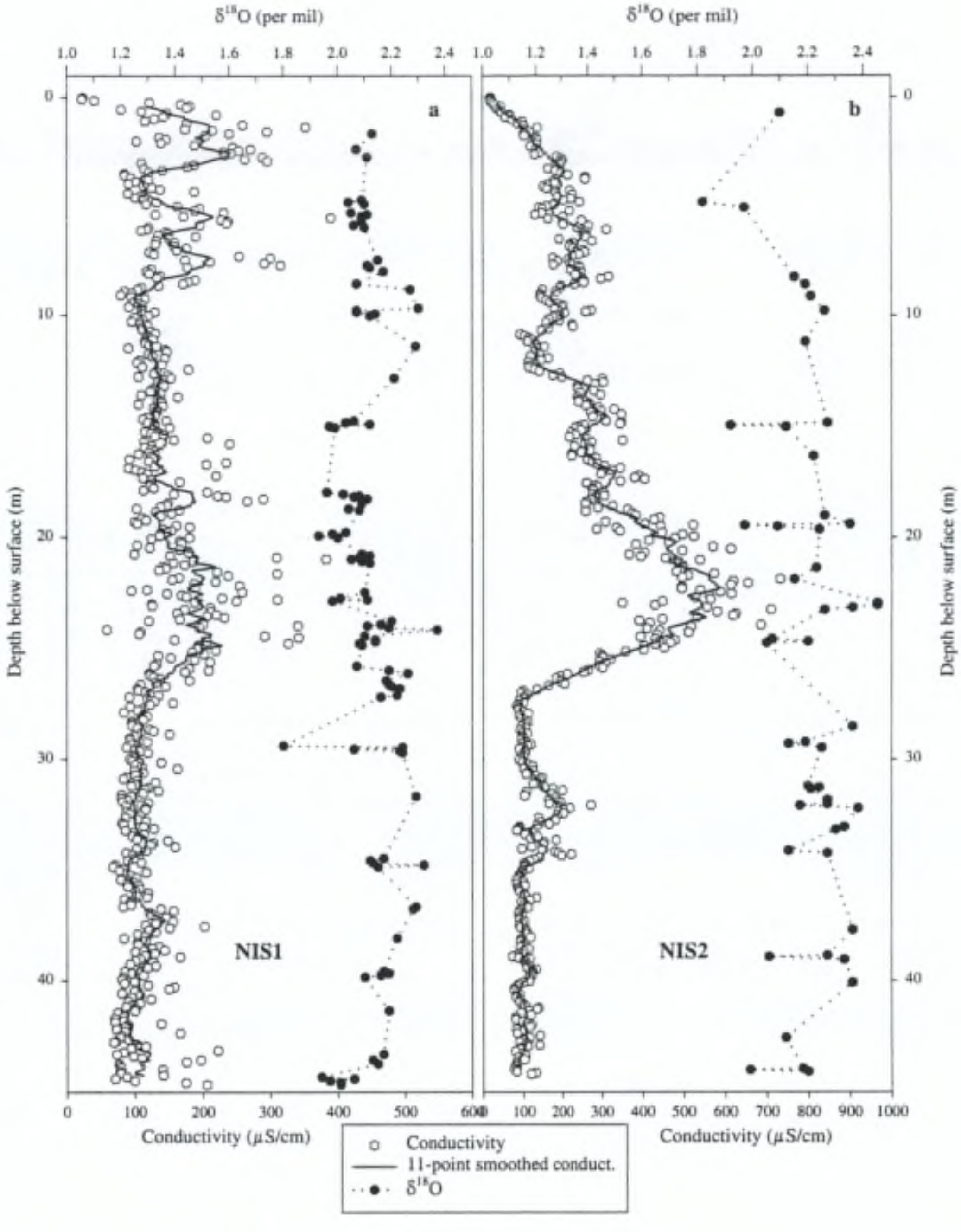

Figure 2.8: The variation of conductivity (salinity), smoothed conductivity (11-point running mean) and $\delta^{18}O$ with depth in (a) NIS1 core and (b) NIS2 core. Notice that the conductivity scale is not the same in the two plots.

Furthermore, the high resolution of sampling has revealed the presence of smaller scale (decimeter) fluctuations in the salinity signal which exceed the measurement error. The amplitude of this variation clearly increases with higher salinity values. Fluctuations have also been observed in sea ice, where *Weeks and*

Ackley [1982] have emphasized the fact that even in the most homogeneous appearing ice there is a small scale, apparently random variation in the salinity.

2.3.3 Stable isotopes

The oxygen isotope composition results which are presented in Figures 2.8a and 2.8b do not show any clearly discernible trend with depth nor do they show substantial variability (standard deviation = 0.09 per mil). Although comparing the profiles of $\delta^{18}O$ and conductivity for NIS1 in Figure 2.8a could suggest a general antipathic behavior between the two, plotting corresponding values in a $\delta^{18}O$/conductivity diagram in Figure 2.9 does not result in a significant correlation ($r^2 = 0.07$, 99 points).

The $\delta^{18}O$ values for both cores cover a range between +1.80 per mil and +2.45 per mil with a mean value of +2.12 per mil for NIS1 and 2.20 per mil for NIS2. This agrees well with the slightly positive values reported for G1 by *Morgan* [1972] and the value of +2 per mil for B13 measured by *Oerter et al.* [1992]. A +2 per mil enrichment of the heavy oxygen isotope is considered by *Eicken et al.* [1994] to be corresponding to that expected from equilibrium fractionation of freezing sea water. *Souchez and Lorrain* [1991] state that the maximum $\delta^{18}O$ value resulting from such a process is +3 per mil. These authors emphasize the contrast between the slightly positive heavy oxygen enrichment of ice of marine origin and its marked depletion in ice of atmospheric origin. This is certainly the case in this study where, for comparison, $\delta^{18}O$ values for continental ice samples from Hells Gate Ice Shelf, which is in the same geographical zone as the Nansen Ice Shelf, cover a range between -26 per mil and -32 per mil [*Ronveaux*, 1992].

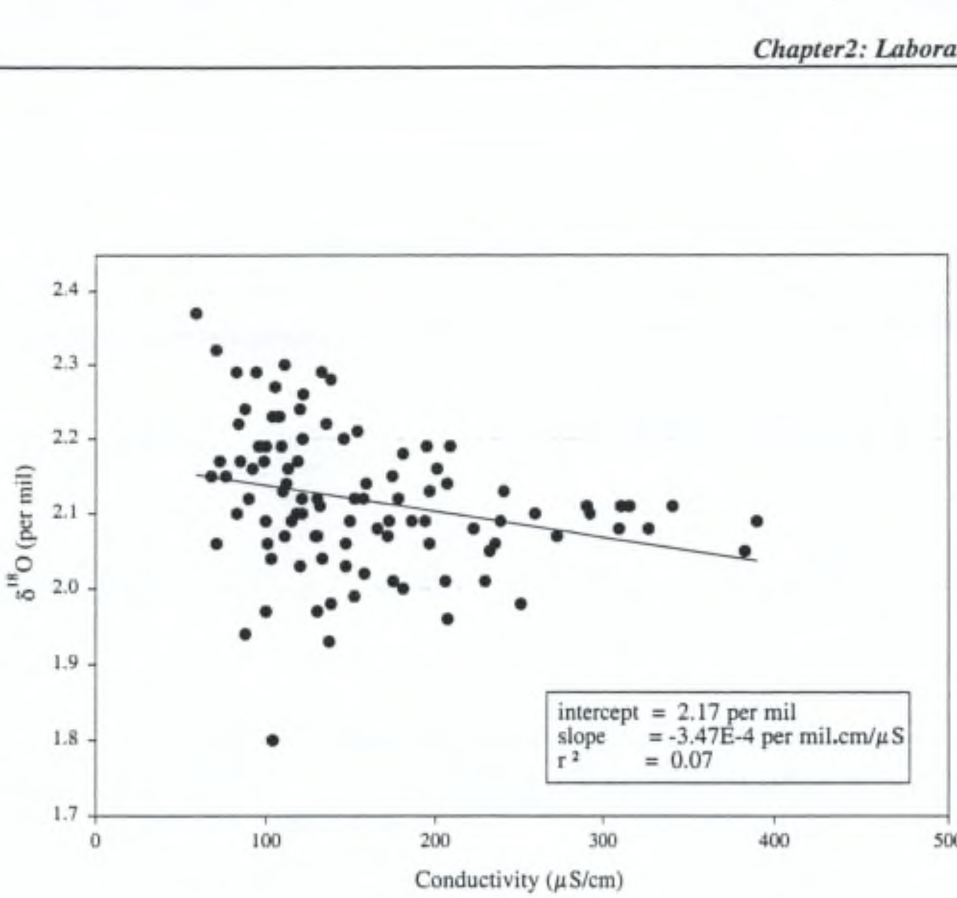

Figure 2.9: The distribution of points in the δ^{18}O/conductivity space for NIS1. The points plotted are the 99 for which both isotopic and conductivity measurements are available. The solid line represents linear regression through all points.

2.4 Discussion and hypothesis

The evidence presented above strongly supports the idea that the NIS cores are entirely composed of marine ice. This conclusion is reinforced by the comparison with B13, B15, and G1. One is thus tempted to directly conclude that the NIS core ice, as was demonstrated for the marine ice sections of the other cores, has formed as a result of the Deep Thermohaline Convection beneath the ice shelf. This circulation includes a phase where fresher and cooler Ice Shelf Water is ascending the lower face of the shelf. Frazil ice crystals are then thought to form as a result of the adiabatic supercooling taking place in the rising water mass. These crystals would thereafter accrete and subsequently consolidate at the bottom of the ice shelf. Such an explanation of the existence of the NIS core ice is however immediately confronted by a basic objection. The same models that were developed by several authors, some of who were cited in the first chapter, to describe these processes predict that the part of the ice shelf/ocean interface nearer to the grounding line is a zone of active melting of ice. This has been shown to be taking place specifically beneath the Nansen Ice Shelf. Measurements conducted by *Frezzotti* [personal communication, 1998] indicate a basal melting rate of the order of 2.4 meters/year between the NIS grounding line and 16 km down-flow, which well includes the NIS1 core site. Therefore, it is difficult to envisage marine ice accreting and surviving under such conditions. Furthermore, a very crude calculation would show that even if marine ice were to form near the grounding line at a depth of around 500 meters it would never have the time necessary to reach the surface at either core location given the prevalent flow velocities and ablation rates. This last point implies that perhaps marine ice is being formed nearer to the surface in some feature of the bottom topography of the ice shelf.

Considering the geographical location near the grounding line of the study area which is cut by several rifts reaching all the way to the bottom of the ice shelf, and that the formation of such deep rifts often requires the presence of bottom crevasses reaching the surface, rifts and basal crevasses are regarded as the most plausible explanation of the above observations. The discussion of the first chapter shows these to be common features of Antarctic ice shelves.

It is therefore proposed here that a rift or a large basal crevasse near the grounding line would provide a sheltered setting permitting the formation of marine ice in the midst of the basal ablation zone. A volume of water, which should become buoyant as a result of shelf ice melting, would enter and ascend the crevasse becoming supercooled in the process. The basal crevasse would eventually, in part at least, become filled with marine ice in a process comparable to the one described in section 1.1.1 above for the formation, accumulation, and subsequent consolidation of frazil ice under ice shelves. An important difference between the two situations is that, in the case of frazil accumulating in rifts or bottom crevasses, consolidation under the influence of a freezing front is a real possibility due to relative proximity to the interface with the atmosphere.

Already in the surface configuration of the field zone where the cores were taken there is a strong indication to the plausibility of the idea proposed above.

Examining the photograph of Figure 2.2, it is possible to note the succession of the crescent-shaped surface features which extend from the location of NIS1, where the core was collected in one of them, all the way to the grounding line. The form of these features and their source at the grounding line are convincing testimony to their origin as crevasses.

Many of the underlined observed discrepancies between the NIS cores and the marine ice segments of the other cores considered actually support the proposed hypothesis. This includes the relatively higher general salinity of the NIS cores compared with B13, B15, and G1. In the situation being suggested here, higher salinity would be explained by the higher freezing rate of the interstitial water existing among the frazil crystals after their accumulation at the top of the water column and before their consolidation. In the case of a basal crevasse, the ambient water/frazil mixture would be nearer to the surface thus resulting in a more rapidly advancing freezing front and hence less efficient rejection of salt upon freezing. As the freezing front descends further away from the surface, the freezing rate would be reduced, resulting in better salt rejection and the observed trend of decreasing conductivity/salinity with depth. The direct relationship between the freezing rate and initial salt entrapment in sea ice is addressed by *Weeks and Lofgren* [1967] and further developed by *Weeks and Ackley* [1982]. Later, it has been coupled to growth-rate calculations from energy balance equations [*Maykut and Untersteiner*, 1971] and gravity drainage/brine expulsion predictions [*Cox and Weeks*, 1988] to model salt flux in sea ice [*Eicken et al.*, 1995]. A similar approach has been successfully applied to stable isotope fractionation in growing sea ice [*Souchez et al.*, 1988; *Eicken*, 1998], showing an inverse relationship between the freezing rate and the $\delta^{18}O$ (or δD) signal.

The question might then be raised as to why the $\delta^{18}O$ isotopic profiles with depth (Figures 2.8a and 2.8b) do not show a clear analogous influence by the freezing rate, nor does they show a clear inverse correlation with salinity (Figure 2.9). The reply might lay in the fact that, since frazil crystals themselves are almost completely desalinated, the salinity signal results only from the intergranular brine inclusions while the isotopic signal reflects both contributions. Therefore, even if isotopic fractionation does occur in the brine inclusions due to the advancement of a freezing front, the resulting signal would be submerged by the overwhelming and unmodified contribution from the crystals. As for the isotopic signal of the crystals themselves, it is plausible that the temperature and pressure conditions necessary for the formation of frazil ice in the successive ascending water masses are regularly satisfied at certain specific depths in the water column, thus producing frazil crystals with more or less the same isotopic enrichment, which would account for the rather weak variability in the isotopic signal of the NIS cores. *Eicken et al.* [1994], while noting the decreasing salinity with depth in the B13 core, exclude the advancement of a freezing front as an explanation of the salinity profile on the basis of thermodynamic constraints (conductive heat fluxes in the central Ronne Ice Shelf of the order of 0.1 W/m^2) and of the "anomalously" low salt distribution coefficient ($k_{eff} < 0.001$) that would be needed to explain the observed salinity. Evaluating the impact of possible post-genetic desalination processes, the same authors judged this to be too low by at least two orders of magnitude. This led them to propose that only an already low initial salinity of the newly accreted layers can explain the very low salinity measured in marine ice. They suggest that consolidation under the deviatoric buoyancy stress associated with the tens of meters of crystals accumulating beneath, would lead to densification and expulsion of brine through fragmentation and settling of individual platelet crystals. However, in the near-surface formation setting for marine ice being proposed in this work, thermodynamic growth through the progressively slowing descent of a freezing front cannot be neglected.

Although initial salt entrapment and stable isotope fractionation of the NIS marine ice have been determined by thermodynamic growth, subsequent reworking has clearly taken place as attested to by the salinity profiles of Figures 2.8a and 2.8b. It is the location of the cores and their geomorphologic context which provide at least two possible explanations for the presence of large scale conductivity/salinity deviations from the baseline values: the first is related to the dynamically active core site environment, which is described above to be a zone where different ice streams converge with different velocities thus creating a situation where the ice is subjected to lateral compression. Such a stress configuration would fold the ice body and disturb the initial stratification as sketched in Figure 2.10 and as witnessed to by the small scale folding features in the core (Figure 2.6a). One objection that could be raised to this idea is why would large scale compression only selectively affect the part of the core, in the case of NIS1 for example, that lies above 28 meters depth and spare the lower part, as could be inferred from Figure 2.8a. The response could be that large scale folding has also occurred in the lower parts of the core but it is not as visible because ice strata there are characterized by low contrast between their salinity values.

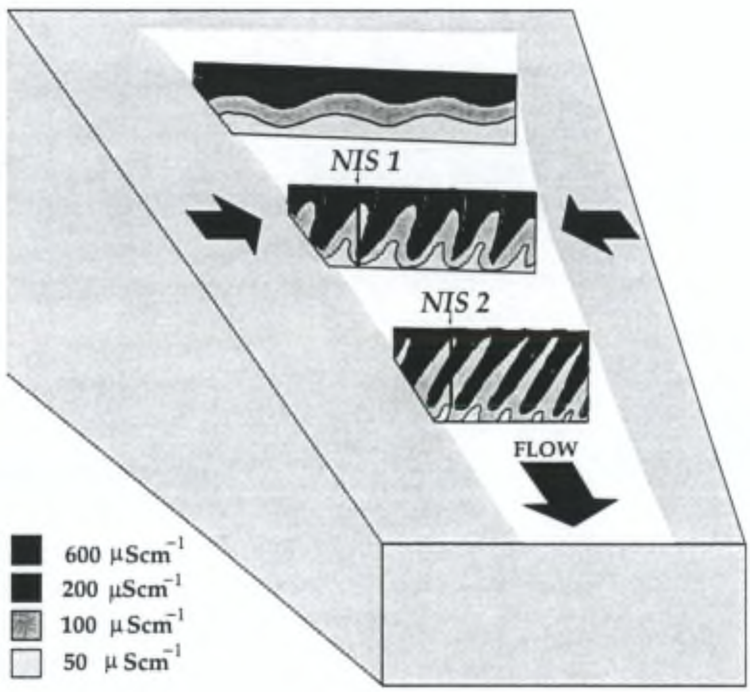

Figure 2.10: A schematic sketch of possible modification of the initial ice stratification due to lateral compression.

A second possible explanation is related to the core's location near the surface of the ice shelf where its brine content could be affected by seasonal temperature changes. The resulting temperature gradients could create the necessary conditions, especially in the top few meters, to induce a form of the phenomena known in the sea ice literature as brine pocket migration [*Hoekstra et al.*, 1965; *Seidensticker*, 1966]. There are several factors that could result in a pocket of brine having a net vertical displacement. These include the asymmetry of the seasonal temperature signal, the vertical component of the ice velocity thus further asymmetrically changing the thermal gradients to which a brine pocket is subjected with time, and the fact that, unlike shorter-lived sea ice, marine ice in a setting as the one described here is subjected to these varying thermal regimes over an extended period of time. The problem with this idea however is the slowness of the process [*Weeks and Ackley*, 1982; *Eicken et al.*, 1994], associated with the fact that the seasonal temperature signal does not significantly affect the temperature profile below a certain depth (in continental ice, field observations show that seasonal variations are undetectable below a depth of 20 meters [*Paterson*, 1994]).

A basal crevasse, with its vertical spatial extension, would also account for the appearance of marine ice layers on the shelf surface despite proximity to the grounding line. This would also imply a relatively young age for the NIS cores ice (in the order of 50 to 100 years) compared to the hundreds of years estimated for the Filchner-Ronne cores by *Eicken et al.* [1994]. This would give the grains of the NIS cores less time to recrystallize, thus resulting in their relatively smaller sizes. On the other hand, the abundance of crystals exhibiting the string-lined facies and their vertical orientation could be due to grain recrystallization under the influence of horizontal compressive forces applied by the walls of the crevasse. The presence of such forces could in part be inferred from the appearance of folding in the core and its direction, in addition to the non-horizontal direction of the layers of debris which suggests at least a horizontal component for the acting force.

2.5 Conclusion

The evidence examined in this chapter does not leave much doubt about the plausibility of the main hypothesis of the current work. The accretion of marine ice in a zone where melting is the dominant process, the abundance of rifts and basal crevasses in the coring zone, the form that these features have on the surface of the ice shelf, the presence of marine ice at the surface of the shelf and the discrepancy it shows relative to other marine ice cores all promote the idea of bottom crevasses and rifts providing environment suitable for marine ice formation.

One objection that could be raised is the possibility that the marine ice cored from the Nansen Ice Shelf originated from a layer of marine ice that had formed at the ice shelf/ocean interface as a result of thermohaline convection in the sub ice shelf cavity. The block then detached from the main marine ice body and was subsequently trapped in a basal crevasse or rift where it is found. Two arguments could be used to refute this objection. The first is that, at least in the case of NIS1, the core location is upstream from the possible location of marine ice formation as part of thermohaline convection. Such circulation involve a current of Ice Shelf Water flowing towards the front (building marine ice on its way), which means that any detached marine ice will flow away from the core location upstream.

The second argument is simply the fact that there are two ice cores from two different locations of which the properties support the hypothesis and it is difficult to imagine the scenario proposed by the objection occurring in both instances.

Another variation of the same objection is that marine ice did form in a crevasse or rift near the grounding line and then it detached and subsequently entered another crevasse downstream where it was found. The idea is that at its formation, the crystals would have horizontal orientation as in the case of B13 and B15 but when displaced into the other crevasse the orientation of the whole block of ice was tilted thus producing the observed vertical tendency in NIS1 and NIS2. Again, the probability that such a sequence of events occurs at two different locations is remote.

The task of the next chapter, now that the hypothesis is established through a laboratory study, is to demonstrate that a mathematical model, built on sound physical bases, generates results that support the feasibility of the process proposed here.

Chapter 3

Rift model: Theoretical bases

The only modeling work that could be found in the literature dealing with ice formation in a rift or bottom crevasse is that of *Weertman* [1980]. In it, the author presents an approximate analytical calculation of direct sea water freezing on the walls of a newly opened crack at the bottom of an ice shelf. *Weertman* [1980] concludes that, in the absence of circulation in the crevasse, ice formation would fill up cracks opening in shelves less than 400 meters thick. In the others, freezing would not be enough to prevent the crack form continuing to creep open.

In the numerical model proposed here, a rift or basal crevasse is already wide open with a turbulent plume active inside. Ice formation is mainly through the creation of frazil ice crystals in addition to direct freezing on the portion of the wall of the cavity where the water in the plume begins to be supercooled.

The concept and structure of the rift model presented in this work find their origins in three different sources.

As for the general idea, this model could be considered another application of what has become to be known as the ice pump mechanism: the process by which ice in contact with sea water is melted at depth and deposited higher in the water column.

A detailed mechanism, by which this transfer of ice through the water column takes place, is needed. The simulation of melting and freezing processes at the ice/ocean interface is therefore provided by a plume model, which is at the heart of the current rift model structure.

In the confined space of a rift situation, such a plume will actually be modifying the properties of the water it is entraining, to which it is in turn most sensitive. Therefore, a description of the manner by which the ambient water in the rift evolves with time is necessary, and this is inspired by filling-box models.

3.1 The ice pump concept

In addition to salinity, the freezing point of sea water, T_f, is also a function of pressure. This dependence can be seen from the following equation which is typically used in ice/ocean interface models. This relation is expressed in terms of depth below sea level, pressure being a direct linear function of depth:

$$T_f = aS + b + cz, \tag{3.1}$$

where S is the salinity of the body of water given in practical salinity units (psu) and z is the depth in meters (increasingly negative downwards) at which the water is found. *Millero* [1978] gives a review of the work done by several investigators studying the relationship between sea water's freezing point and its salinity and depth. The above equation is actually a linearized approximation of the original relation that the author recommends using. Thus, the dependence on salinity is expressed by *Millero* [1978] as:

$$T_f(S) = q_1 S + q_2 S^{3/2} + q_3 S^2,$$

where $q_1 = 0.0575$, $q_2 = -1.7105\text{E-3}$ and $q_3 = 2.1550\text{E-4}$. Since the non-linear salinity terms in this relation are multiplied by relatively weak coefficients, most workers therefore drop them and content themselves with the linear term for ease of calculation. The relation above is based on data from experiments on water samples of salinity ranging between 4 and 40. *Millero* [1978] points out that consequently some error is incurred if the relation is used for fresh water.

As for pressure dependence, experiments done by *Fujino et al.* [1974] on water of salinities in the range between 27 and 35 show that all salinities have the same freezing point pressure dependence and that this dependence is linear. In arriving at these conclusions, the authors used pressures of up 100 bars, which is approximately equivalent to a column of water 1000 meters thick.

Fofonoff and Millard [1983] indicate that the recommendation of *Millero* [1978] and the conclusions of *Fujino et al.* [1974] are adopted by the Joint Panel on Oceanographic Tables and Standards. In the linear approximation of equation (3.1), the numerical values of the empirical coefficients typically used (e.g. *Jenkins and Bombosch* [1995]) are a = -0.0573°C/psu (the depression of the freezing point with increasing salinity), b = 0.0832°C (a constant coefficient) and c = 0.0761E-2 °C/m (the depression of the freezing point with depth).

Although the numerical value of c is less than that of a, in the situations studied in this work, depth could vary by up to two orders of magnitude while the change in salinity is restricted to fractions of a psu. Consequently, changes of depth are much more important in determining the freezing point than variations in salinity.

It is the depression of the freezing point with increased pressure which is at the source of the ice pump concept. Hence, as *Williams et al.* [1998] emphasize, at sea-level atmospheric pressure 90% of ocean waters freeze at temperatures between -1.87 and -1.92°C, but at a depth of 1500m the corresponding range is -3.01 and -3.06°C, which gives water at the surface freezing point the potential to melt ice at depth.

As a result of the melting of fresh water ice in the ocean, both the temperature and salinity of the resulting mixture are reduced relative to the ambient with opposite effects on density. However, in the range of temperatures encountered in polar oceans, the effect of lower salinity in reducing density overwhelms that of its increase due to lower temperature. This can clearly be seen in the temperature-salinity diagram of Figure 3.1, where the isopycnal lines (lines of constant density) are very steep around the freezing point. *Greisman* [1979] addresses the question of the density of melt water relative to that of ambient water. Using the appropriate mixing proportions for heat and salt, the author derives the slope of the straight line in the temperature/salinity space resulting from the melting and mixing processes. In doing so, heat flux into the ice is ignored. The mixing slope is then compared to the local slope of the isopycnal line which is derived from an equation of state for sea water. *Greisman* [1979] consequently divides the temperature/salinity space into two main parts according to whether the melt floats or sinks as illustrated in Figure 3.1. He states that although temperature differences are necessary for melting, the dependence of the resulting melt water density on temperature is weak below 20°C for water of typical oceanic salinities. The author describes the temperature in this case as a passive tracer, no doubt because its detection in fieldwork, in association with other parameters, is an indication of melting taking place deep in the ice shelf cavity far from direct observation.

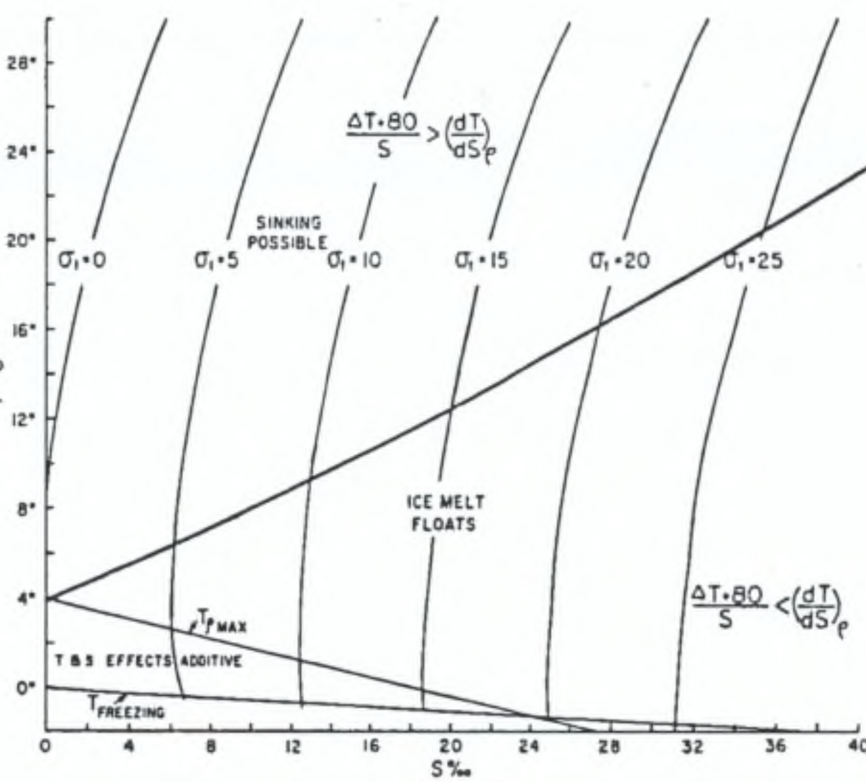

Figure 3.1: Isopycnal lines in the Temperature-salinity space which is divided into zones according to whether the melt sinks or flows. The quantity $(\Delta T + 80) / S$ is the mixing slope derived by *Greisman* [1979], from which this figure is reproduced.

The term "ice pump mechanism" was coined by *Lewis and Perkin* [1986] to describe the mechanism, driven by the change of freezing point with depth, by which ice is melted at depth in the ocean and deposited at a shallower location. It is interesting to note that the first of these two authors in a previous work related to sea ice, *Lewis and Lake* [1971], was even contesting the occurrence of supercooling in Antarctic waters other than as a transient condition that has no role in ice formation processes. To illustrate the ice pump idea, *Lewis and Perkin* [1986] also proposed a conceptual experiment which supposes a tank of sea water with one vertical wall made of ice. Papers by several investigators, such as *Huppert and Turner* [1980] and *Josberger and Martin* [1981], describe in detail methods to construct experimental configurations of vertical ice walls in saline water. When the ice is vertically introduced into the water tank, melting would start at the bottom because of higher pressure. The addition of fresh melt results in a mixture with the capacity to ascend the water column because of its buoyancy relative to the surrounding, more dense, ambient water. *Foldvik and Kvinge* [1974] proposed the idea that such a rising mass of water will become supercooled relative to the surrounding water since the in-situ freezing point decreases with reduced pressure. The authors suggested that the release of this supercooling could be attained through the production of frazil crystals in the water column. *Doake* [1976] used this idea to explain melting and freezing processes beneath ice shelves and then *Robin* [1979] explicitly proposed that melting takes place beneath the deeper parts of an ice shelf while ice deposition prevails below shallower parts as part of thermohaline circulation.

3.2 Model for ice-ocean interaction

Up to date, several types of models have been devised to simulate sub-ice shelf circulation. One thing they all have in common is the treatment of thermodynamic processes taking place at the ice-ocean interface. Exchanges of mass and heat at this boundary have a profound impact on the nature of the circulation and the properties of the water being circulated. As outlined by *Williams et al.* [1998], such models could be divided into two categories according to the main type of forcing at the source of the flow: tidal models and thermohaline models. The latter include plume models, two-dimensional models and three-dimensional models. Tidal [e.g. *Sheduikat and Olbers*, 1990], two- [e.g. *Hellmer and Olbers*, 1989] and three-dimensional thermohaline models [e.g. *Determann and Gerdes*, 1994], which concentrate on simulating large scale circulation in the sub-ice cavity, are difficult to adapt to the confined space of an open rift or bottom crevasse. One variety of plume models created by *Jenkins and Bombosch* [1995] lends itself more readily to the rift problem, as presented in the second chapter, since it is the only one that explicitly contains a treatment of frazil ice formation in an ascending plume. This is in contrast to other plume models [e.g. *Jenkins*, 1991] where supercooling is released exclusively through direct freezing on the bottom of the ice shelf (or the side of the rift in the current problem). Therefore, the *Jenkins and Bombosch* [1995] model is adopted and adapted to the rift problem.

3.2.1 The Jenkins-Bombosch plume model

In this section, equations of the plume and frazil model are listed. *Jenkins and Bombosch* [1995] developed this model from the one presented by *Jenkins* [1991] by including in it a treatment of frazil ice formation in the plume and its subsequent possible deposition. When applied to thermohaline convection beneath the Ronne Ice Shelf [*Jenkins*, 1991] and the Filchner-Ronne Ice Shelf [*Bombosch and Jenkins*, 1995] both models showed good agreement with field measurements. The 1991 Jenkins simple one-dimensional model is in turn similar in concept to *MacAyeal*'s [1985] streamtube simulation and its equations are adapted from those conventionally used in the description of turbulent gravity currents. Figure 3.2 presents the plume model configuration associated with the equations below as it is constructed by *Jenkins and Bombosch* [1995].

The model envisages a two-component (frazil plus water) turbulent gravity current ascending the interactive (melting and freezing) underside of an ice shelf. This plume overlies a stationary body of ambient water from which entrainment takes place.

In deriving model equations, *Jenkins and Bombosch* [1995] make several assumptions. The flow of the plume is supposed to be plane and all properties are taken to be constant over its thickness (except when considering the details of diffusion processes at the ice/water interface). Average values of these properties are calculated when dealing with plume dynamics since the granular structure of the plume is approximated by that of a homogeneous fluid. Sea water is treated as incompressible and the Boussinesq approximation is applied to it (which means that density differences are ignored in inertial terms but considered where they give rise to buoyancy). Steady state is assumed.

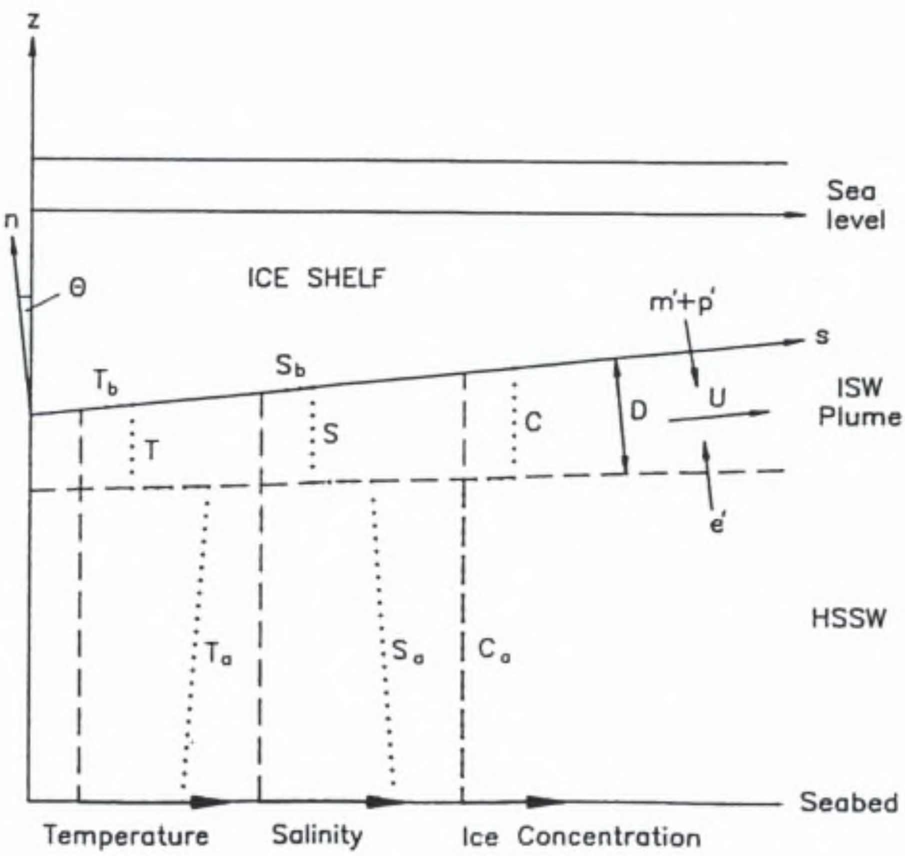

Figure 3.2: The configuration of plume model as presented by *Jenkins and Bombosch* [1995].

Density equations: The mean density of the plume, ρ_m, is obtained by summing the densities of its two components, thus:

$$\rho_m = \rho + C(\rho_i - \rho),$$

where ρ is the density of the water fraction of the plume while ρ_i is the density (considered to be constant) of the ice fraction C. One simplification *Jenkins and Bombosch* [1995] made is to put $\rho = \rho_0$ (where ρ_0 = 1030kg/m^3 is a reference sea water density) whenever the mass of the fluid, rather than its weight, is being considered. This is an application of the Boussinesq approximation and in this case the mixture density is denoted by $\rho_m^\bullet$. All densities are in kg per cubic meter.

The density of the plume water is given by the relation:

$$\rho = \rho_0\left[1 + \beta_S(S - S_0) - \beta_T(T - T_0)\right], \tag{3.2}$$

where S_0 = 34.5 and T_0 = -2.0°C are reference salinity and temperature, respectively. The significance of the coefficients β_S = 7.86E-4psu^{-1} and β_T = 3.87E-5°C^{-1} is discussed in section 3.2.2 below.

Plume properties equations: the evolution of five plume properties, specifically its thickness (D, meters), velocity ($\mathbf{U}$, meters per second), frazil ice concentration in the plume by volume (C, dimensionless), temperature (T, degrees Celsius) and salinity (S, psu) is calculated from the following five conservation ordinary differential equations.

Mass conservation equations:

$$\frac{d}{ds}(DU) = e' + m' + p', \tag{3.3}$$

$$\frac{d}{ds}(DUC) = \frac{\rho_0}{\rho_i}(p' - f'), \tag{3.4}$$

where e' is the entrainment rate, m' is the melt rate at the ice-ocean interface, p' is the precipitation rate of frazil crystals and f' is the total melt rate of frazil ice in the plume (all are in units of meters of water at the reference density ρ_0 per second and are positive when mass is gained by the plume).

Momentum conservation equation:

$$\frac{d}{ds}\left(DU^2\right)=\frac{\left(\rho_m-\rho_a^D\right)}{\rho_0}Dg\sin\theta-KU^2, \tag{3.5}$$

where g = 9.81m/s^2 is the acceleration of gravity, θ is the slope of the ice shelf base with respect to the horizontal and K = 2.5E-3 is the drag coefficient. ρ_a^D is the average the ambient water density over the thickness of the plume:

$$\rho_a^D=\frac{1}{D}\int_{-D}^{0}\rho_a dn.$$

Heat and salt balance equations: If T_a, T_b and T_c are, respectively, the temperature of the ambient water at the bottom of the plume, the temperature of the water in contact with base of the ice shelf and the temperature of the water in contact with the ice crystals. And if the depth average of the latter across the plume is T_c^D, then:

$$\begin{aligned}&\frac{d}{ds}[(1-C)DUT]=\\&e'T_a+m'T_b+\int_{-D}^{0}w'T_c dn-(1-C)\gamma_T^b\left(T-T_b\right)-(1-C)D\gamma_T^c\left(T-T_c^D\right)A_c\end{aligned}, \tag{3.6}$$

$$\begin{aligned}&\frac{d}{ds}[(1-C)DUS]=\\&e'S_a+m'S_b+\int_{-D}^{0}w'S_c dn-(1-C)\gamma_S^b\left(S-S_b\right)-(1-C)D\gamma_S^c\left(S-S_c^D\right)A_c\end{aligned}, \tag{3.7}$$

where γ_T^b and γ_T^c, for which the expressions are given below in section 3.2.2, are the heat transfer coefficients (meters per second) at the ice shelf base and at the edge of frazil crystals, respectively. The volume of water created by melting of frazil ice per unit volume of mixture per unit time is donated by w', while A_c, for which the expressions is also given in the following section, is the total surface area of the crystals per unit volume of the mixture. The parameters in the equation for salt balance are defined in an analogous manner.

Ambient fluid entrainment relation: One of the quantities that appear in the above differential equations is the entrainment rate. This is calculated using the relation:

$$e' = E_0 U \sin\theta , \tag{3.8}$$

where E_0 is the entrainment constant, which is discussed in more detail below.

Equation for the deposition of ice crystals from turbulent suspension: Another quantity that arises in the above differential equations is p'. To evaluate this parameter, *Jenkins and Bombosch* [1995] adopt the treatment of *McCave and Swift* [1976]. The relation they propose, which represents the rate at which ice crystals settle out from the plume into the ice shelf base in a process of "inverted sedimentation" is expressed as:

$$\rho_0 p' = -\rho_i C W_d \cos\theta \left(1 - \frac{U^2}{U_c^2}\right) He\left(1 - \frac{U^2}{U_c^2}\right), \tag{3.9}$$

where U_c is a critical plume velocity above which no precipitation occurs and W_d is the velocity at which crystals settle into the thin, non-turbulent, viscous layer adjacent to the base of the ice shelf. *He* is a function that takes the value 1 if its argument is positive or zero and is zero if its argument is negative. It is introduced in order to prevent the erosion of previously deposited crystals.

Equations for melting and freezing at the ice-ocean interface:

$$(1-C)\gamma_T^b\left(T-T_b\right)=\frac{L}{c_0}m'-\frac{\rho_i c_i K_i}{\rho_0 c_0}\left(\frac{dT_i}{dn}\right)_b, \tag{3.10}$$

$$(1-C)\gamma_S^b\left(S-S_b\right)=m'S_b, \tag{3.11}$$

where the parameters for ice are given by K_i = 1.14E-6m^2/s which is the thermal diffusivity, T_i is the temperature, c_i is the specific heat capacity (2009.0 joule per kilogram per degree Celsius) and L = 3.35E5J/kg is the latent heat of fusion. c_0 = 3974.0J/kg°C is the specific heat capacity of water. In the equation for salt S_b represents the salinity at the base of the ice shelf. The heat and salt transfer coefficients are given by (adopted from *Kader and Yaglom* [1972]):

$$\gamma_T^b=\frac{K^{1/2}U}{2.12\ln\left(K^{1/2}UD/\nu\right)+12.5\Pr^{2/3}-9}, \tag{3.12}$$

$$\gamma_S^b=\frac{K^{1/2}U}{2.12\ln\left(K^{1/2}UD/\nu\right)+12.5Sc^{2/3}-9}, \tag{3.13}$$

where Pr = 13.8 is the dimensionless Prandtl number (which is proportional to the ratio of molecular viscosity and thermal diffusivity) and Sc = 2432 is the equivalent Schmidt parameter for salt transfer.

Interface temperature and salinity equation: In the above two algebraic equations for melting and freezing at the ice/ocean interface, (3.10) and (3.11), there are three unknowns: the melt rate in addition to interface temperature and salinity. The third necessary equation is provided by equation (3.1) and thus it takes the form:

$$T_b=aS_b+b+cz_b,$$

where z_b is the depth below sea level (negative downwards) of the point at the interface at which temperature and salinity are being calculated.

Equations for melting and freezing of suspended ice crystals: Heat and mass exchanges at the suspended crystal/plume water interface are analogous to the ones related to the ice shelf/ocean interface:

$$(1-C)\gamma_T^c\left(T-T_c^D\right)D\frac{2C}{r}=\frac{L}{c_0}f', \tag{3.14}$$

$$(1-C)\gamma_S^c\left(S-S_c^D\right)D\frac{2C}{r}=\int_{-D}^{0}S_c w' dn, \tag{3.15}$$

$$T_c^D = aS_c^D + b + c\left(z_b - \frac{D\cos\theta}{2}\right), \tag{3.16}$$

where r is the specified radius of frazil disks. Solving these equations yields the remaining unknown quantities in the differential plume equations, namely, T_c^D, S_c^D and f'. To render this feasible, *Jenkins and Bombosch* [1995] propose using the following approximation in equation (3.15):

$$\int_{-D}^{0}S_c w' dn = S_c^D f'.$$

3.2.2 Discussion of the plume model equations and their adaptation to the rift model

Comments are now presented on the equations of the plume model listed above. In addition, some derivations or hints for arriving at them are included. The objective is to give a clearer idea of the different considerations and approximations that are made in constructing these equations thus providing a better insight into the functioning of the model and its limitations. Also discussed in this context are the different modifications that are made to the above plume model in order to adapt it to the rift model.

In the process, it is noticeable that frequent recourse to approximation are made in deriving the plume model equations. This is an inherent part of any investigative effort of phenomena involving turbulence. Because of their non-linear nature, equations of fluid flow are not possible to solve, except for the simplest examples. Therefore, as *Cipra* [1995] explains, workers in the field have to look for shortcuts: models of fluid flow that combine theoretical insights and physical intuition to produce simplifying assumptions.

Density: Equation (3.2) results from a direct application of the Taylor series expansion. This is possible since the temperature and salinity space, on which the density depends, could be considered as forming a continuum. This makes it possible to express the properties at a certain point in that space as a function of properties at a neighboring point. If $\phi(x)$ is a function which has a certain value at point x_0 then its value at x_1 is given by the Taylor series expansion as:

$$\phi(x_1) = \phi(x_0) + (x_1 - x_0)\left.\frac{d\phi}{dx}\right|_{x_0} + \frac{(x_1 - x_0)^2}{2!}\left.\frac{d^2\phi}{dx^2}\right|_{x_0} + \cdots.$$

In the current problem, the fluctuations of density are small enough to permit dropping the second order and higher terms in the expansion. From this expansion formula, the values of the coefficients in equation (3.2) can be deduced:

$$\beta_S = \frac{1}{\rho_0}\left.\left(\frac{\partial\rho}{\partial S}\right)_T\right|_{S_0},$$

which is the haline contraction coefficient of sea water, and

$$\beta_T = \frac{1}{\rho_0}\left.\left(\frac{\partial\rho}{\partial T}\right)_S\right|_{T_0},$$

which is the thermal expansion coefficient of sea water.

It is now also clear that S_0 and T_0 are, respectively, the salinity and temperature at which the reference sea water density ρ_0 is calculated. The numerical values of all these parameters are given in the previous section. β_S is at least an order of magnitude larger than β_T. This could be taken as another indication of how the change in salinity is the dominant factor in determining the density near the freezing point according to equation (3.2).

Mass: Equation (3.3) expresses the conservation of the total mass of the plume mixture (water and ice crystals). The starting point in deriving this relation is to express the conservation of the mass of the mixture as:

$$\frac{\partial}{\partial t}\left(\rho_m^\bullet\right)+\nabla\cdot\left(\rho_m^\bullet \mathbf{U}\right)=0.$$

This is the differential form of the continuity equation for an incompressible fluid. Using the assumption of steady state (which makes the first term on the right hand side of the equation drop) and plane flow, then:

$$\frac{\partial}{\partial s}\left(\rho_m^\bullet U\right)+\frac{\partial}{\partial n}\left(\rho_m^\bullet W\right)=0, \tag{3.17}$$

where U is the s-component of the plume velocity and W is the corresponding n-component. The velocity profile with thickness of a plume flow is roughly Gaussian [e.g. *Ellison and Turner*, 1959]. However, as mentioned above, *Jenkins and Bombosch* [1995] make the assumption that all properties are constant over the plume thickness, including velocity. With that in mind, integrating the above equation over the plume thickness gives:

$$\int_{-D}^{0}\frac{\partial}{\partial s}\left(\rho_m^\bullet U\right)dn+\int_{-D}^{0}\frac{\partial}{\partial n}\left(\rho_m^\bullet W\right)dn=0.$$

Evaluating the first term on the left using the Leibnitz's rule for differentiating an integral gives:

$$\int_{-D}^{0}\frac{\partial}{\partial s}(\rho_m^{\bullet}U)dn=\frac{\partial}{\partial s}\int_{-D}^{0}(\rho_m^{\bullet}U)dn-(\rho_m^{\bullet}U)\frac{\partial 0}{\partial s}-(\rho_m^{\bullet}U)\frac{\partial D}{\partial s}=\frac{\partial}{\partial s}(\rho_m^{\bullet}UD)-(\rho_m^{\bullet}U)\frac{\partial D}{\partial s},$$

while the second term on the left gives:

$$\int_{-D}^{0}\frac{\partial}{\partial n}(\rho_m^{\bullet}W)dn=\int_{-D}^{0}d(\rho_m^{\bullet}W)=\rho_m^{\bullet}(W_0-W_{-D}).$$

The vertical velocity at the upper edge of the plume, W_0, is the combination of both the melting/freezing and frazil precipitation rates. The configuration of the problem is such that both of these rates have an opposite sign to the displacement of the upper edge, hence:

$$\rho_m^{\bullet}W_0=-\rho_0 m'-\rho_0 p'.$$

The factor ρ_0 appears on the right hand side to ensure that mass fluxes on both sides of the equation are equal, since the melt and precipitation rates are expressed in terms of thickness at the reference fluid density.

On the other hand, W_{-D}, the net vertical velocity of the lower edge is the combination of the rate at which the plume is spreading out (in the negative n-direction) and the entrainment velocity (in the positive n-direction). The plume spreading rate, with the assumption of steady state, can be written as:

$$\frac{D}{Dt}(D)=\frac{\partial D}{\partial t}+(\mathbf{U}\bullet\nabla)D=U\left(\frac{\partial D}{\partial s}\right).$$

Therefore,

$$\rho_m^{\bullet}W_{-D}=-\rho_m^{\bullet}U\left(\frac{\partial D}{\partial s}\right)+\rho_0 e'.$$

Putting all the expressions together results gives:

$$\frac{\partial}{\partial s}\left(\rho_m^{\bullet}UD\right)-\rho_0 m'-\rho_0 p'-\rho_0 e'=0\,.$$

Substituting for $\rho_m^{\bullet}$ and using the following approximation proposed by *Jenkins and Bombosch* [1995]:

$$C\frac{\left(\rho_i-\rho_0\right)}{\rho_0}=0, \tag{3.18}$$

gives equation (3.3) after some rearrangement. Equation (3.4), which expresses the conservation of the ice fraction in the plume, could be derived in a similar manner using in the process the same above approximation. A relation expressing the conservation of the water fraction of the plume could be directly obtained by subtracting equation (3.4) from equation (3.3).

Momentum: The origin of equation (3.5), the statement of the conservation of linear momentum, is written by *Jenkins and Bombosch* [1995] as:

$$\rho_m^{\bullet}\frac{\partial\mathbf{U}}{\partial t}+\rho_m^{\bullet}\mathbf{U}\bullet\nabla\mathbf{U}=-\nabla P-\rho_m g\mathbf{k}+\nabla\bullet\mathbf{T}\,, \tag{3.19}$$

where P is pressure, $\mathbf{k}$ is a unit vertical vector, g is the acceleration due to gravity and $\mathbf{T}$ is the Reynolds stress tensor. This relation is an application of Navier-Stokes equation for an incompressible fluid (without the terms due to the Coriolis acceleration nor molecular viscosity), which is often used as the starting point for solving fluid flow problems.

This equation is a direct application of Newton's second law of motion with the left-hand side representing the total rate of change of momentum ($\rho_m^{\bullet}\mathbf{U}$) with time, which is equivalent to the resultant of forces on the body. It is obtained by applying the operator known as the total derivative (which is also used in the mass conservation equations above):

$$\frac{D}{Dt}=\frac{\partial}{\partial t}+(\mathbf{U}\bullet\nabla).$$

This is how the total rate of change with time is described in the Eulerian representation of nature. The fact of dealing with a continuum rather than particles requires such representation. The right-hand side of the equation (3.19) is the sum of the forces acting on the fluid. A similar momentum equation can be written for the ambient water taking into consideration that it is stationary. This has the form:

$$0=-\nabla P_a-\rho_a g\mathbf{k}.$$

Subtracting this equation form equation (3.19), a momentum balance relation along the s-coordinate could be obtained using the approximations of steady state, plane flow, small aspect ratio, employing equation (3.17) to show that:

$$\frac{\partial U^2}{\partial s}+\frac{\partial WU}{\partial n}=U\frac{\partial U}{\partial s}+W\frac{\partial U}{\partial n},$$

and replacing $\rho_m^\bullet$ by ρ_0 using the approximation (3.18) in association with another approximation:

$$\rho_m^\bullet=\rho_0+C(\rho_i-\rho_0).$$

The dimensional analysis of gravity flows carried out by *Mahrt* [1982] justifies that, in the equation resulting from the above manipulation, the pressure gradient term, $\frac{\partial}{\partial s}\left(P-P_a\right)$, could be ignored provided that the thickness of the plume is small compared to the height of its rise. With this in mind, depth integration could then proceed in a manner similar to that of the mass conservation equation above to obtain equation (3.5).

The Reynolds stress tensor accounts for the impact of entrainment on the momentum. As illustrated by *Eskinazi* [1975], the velocity of a parcel, which is entrained from a body of ambient water at rest, has to be increased to that of the plume resulting in momentum loss for the flow. To explicitly introduce the components of **T** into the relation would result in more dependent variables than equations and mathematical closure of the problem would not be possible. It is customary to employ approximations to circumvent such a situation. The one adopted here is to approximate the turbulent stress at the boundaries of the plume by a quadratic drag law following, for example, *Killworth* [1977].

Temperature and salinity: Equation (3.6) is the consequence of the conservation of heat relation expressed as:

$$\rho_0(1-C)c_0\frac{\partial T}{\partial t}+\rho_0(1-C)c_0\mathbf{U}\bullet\nabla T=\nabla\left[\rho_0(1-C)c_0\left(K_T+k_T\right)\nabla T\right]-Q_T, \quad (3.20)$$

where only the water fraction of the plume mixture is considered since diffusion into the frazil crystals is negligible. Q_T is the heat sink or source due to frazil ice melting or formation (watts per cubic meter). K_T = 1.4E-7m^2/s is the molecular thermal diffusivity of sea water while k_T is its turbulent thermal diffusivities (square meters per second).

In writing down the equation in terms of its components, only the vertical one is considered since *Jenkins and Bombosch* [1995] made the approximation that the streamwise distribution of scalar contaminants is negligible compared with cross-flow diffusion. A relation equivalent to equation (3.17) which this time expresses the conservation of the water fraction of the mixture:

$$\frac{\partial}{\partial s}\left[\rho_0(1-C)U\right]+\frac{\partial}{\partial n}\left[\rho_0(1-C)W\right]=\rho_0 w',$$

is employed to show that:

$$\rho_0(1-C)U\frac{\partial T}{\partial s}+\rho_0(1-C)W\frac{\partial T}{\partial n}=\rho_0(1-C)\frac{\partial UT}{\partial s}+\rho_0(1-C)\frac{\partial WT}{\partial n}-\rho_0 w'.$$

Therefore, equation (3.20), with the assumption of steady state, is reduced to:

$$\frac{\partial}{\partial s}[(1-C)UT]+\frac{\partial}{\partial n}[(1-C)WT]=\frac{\partial}{\partial n}\left[(1-C)\left(K_T+k_T\right)\frac{\partial T}{\partial n}\right]-\frac{Q_T}{\rho_0 c_0}+w'T.$$

Depth integration then follows as above. *Jenkins and Bombosch* [1995] give a detailed enough description for the rest of the derivation, which applies in an analogous manner to the salt balance relation. In the process, heat diffusion at the bottom of the plume is ignored compared to the entrainment term while at the ice-ocean interface the diffusion is represented by a heat transfer coefficient (to be discussed below) and the temperature difference between the interface and the plume. The authors also give the following expression for Q_T:

$$Q_T=\rho_0(1-C)c_0\gamma_T^c\left(T-T_c\right)A_c+\rho_0 c_0 w'\left(T-T_c\right),$$

where the first term on the right represents heat diffusion toward or away from the crystals during phase changes. The second term is the heat used to raise the temperature of the water volume resulting from melting to the plume temperature or that of the water to freeze from the supercooled temperature of the plume to the temperature at the crystal-water interface (i.e. the freezing point). Depth integration of Q_T produces the third term on the right of equation (3.6), which *Jenkins and Bombosch* [1995] approximate as:

$$\int_{-D}^{0} w'T_c dn = f'\ T_c^D,$$

where f' is the total melt rate of frazil ice, in meters per second, per unit area of plume.

Interface processes: Equation (3.10) for melting and freezing at the ice-ocean interface is the expression of the energy balance at the interface by which the heat consumed or released during phase change is equivalent to the difference between heat fluxes normal to the interface. *Jenkins and Bombosch* [1995] express this condition as:

$$\rho_i c_i K_i \left(\frac{\partial T_i}{\partial n} \right)_b - \rho_0 (1 - C) c_0 K_T \left(\frac{\partial T}{\partial n} \right)_b = \rho_0 L m'. \tag{3.21}$$

Thus, the first term on the left represents molecular heat flux through the ice shelf while the following term is the molecular heat flux through water.

The equivalent equation for the balance of salt, keeping in mind the assumption that there is no salt gradient in the ice and all salt is taken to be expelled upon freezing, is:

$$- \rho_0 (1 - C) K_S \left(\frac{\partial S}{\partial n} \right)_b = \rho_0 m' \left(S_b - S_i \right). \tag{3.22}$$

In the heat balance equation, values for the temperature gradients, in the water and in the ice, need to be estimated.

Finding the temperature gradient in the water is complicated by the non-uniform structure of the boundary layer between the plume and the ice, of which the thickness is designated by Δ_T. In this layer, the fluid sublayer adjacent to the surface of the ice is characterized by laminar flow where molecular diffusion and a linear temperature gradient prevail. The outer parts of the layer, on the other hand, is dominated by turbulent flow and the temperature profile is nonlinear. The procedure employed to account for such a complicated structure is explained by *Holland and Jenkins* [1999]. The authors propose using another dimensionless parameter, hence, the Nusselt number Nu is introduced. This number actually gives an indication of the ratio of the total heat transfer to conductive heat transfer, which makes its value always greater than one. Hence, in order to account for the increased heat flux due to turbulence in the outer part of the boundary layer, *Jenkins and Bombosch* [1995] multiply the second term on the left of equation (3.21) by the Nusselt number. In that term, the temperature gradient is represented by $\left(T_b - T\right)/\Delta_T$ and after some manipulation equation (3.10) is obtained. In this equation, the following substitution is made:

$$\gamma_T^b = \frac{NuK_T}{\Delta_T}, \tag{3.23}$$

thus introducing the heat transfer coefficient γ_T^b , which has units of meters per second as can be deduced from the above relation. The empirical expression for this coefficient, and that of its salinity counterpart γ_S^b, are given respectively by equations (3.12) and (3.13) above.

This leaves the temperature gradient in the ice as the remaining quantity to be determined in equation (3.21). As *Williams et al.* [1998] state, there is no simple way to estimate the temperature gradient immediately above the ice shelf base. When, for example, *Scheduikat and Olbers* [1990] addressed this question in the context of their tidal model beneath the Ross Ice Shelf they adopted a linear temperature profile. This implies that the temperature in the ice shelf decreases linearly with depth from an average surface temperature to the in-situ freezing point at the ice-ocean interface. Previous work at location J9 in the Ross Ice Shelf described by *Clough and Hansen* [1979] indicates this to be almost the case. However, the discussion in *Paterson* [1994] demonstrates that this is not always true as it is revealed by subsequent measurements in other ice shelves. Indeed, even for the same shelf, the temperature profile could vary from one location to another depending on different factors, including the melting/freezing regime that prevails beneath a certain part of the shelf.

Another point, which is not addressed by *Jenkins and Bombosch* [1995], is the effect of ice flow on the temperature profile at the ice shelf-ocean interface. As stated by *Nost and Foldvik* [1994], heat conduction normal to the flow lines in the ice means that some of the heat conducted into the ice at one position is advected to another position downstream.

Nevertheless, heat conduction into the ice shelf could be negligible compared to the heat exchanged during melting and freezing as a result of the pressure-dependence of the freezing point. For example, estimations by *Jacobs et al.* [1979]

show that heat loss into the ice could not account for more than 3.5cm of freezing per year at J9. Furthermore, some investigators ignore heat conduction into the shelf altogether in their models [e.g. *Lane-Serff*, 1995; *Grosfeld et al.*, 1998]. For their plume model, *Jenkins and Bombosch* [1995], state that since the heat flux is such a comparatively small quantity, it can either be specified or ignored. They opt for the latter solution.

In the version of the plume model used in the current rift model, however, the treatment later proposed by *Holland and Jenkins* [1999] is adopted. These authors solve the heat transport equation in an ice shelf by allowing for vertical advection within a shelf assumed to be in steady state and to have a constant vertical velocity equal to the basal melting or freezing rate. From the solution, *Holland and Jenkins* [1999] derive an expression for the temperature gradient at the ice shelf base as:

$$\left(\frac{\partial T_i}{\partial n}\right)_b = \Pi \frac{(T_i - T_b)}{H_i},$$

where T_i is the temperature at the surface of the shelf and H_i is its thickness. The authors designate the dimensionless parameter Π as the temperature gradient amplification factor. The analysis of *Holland and Jenkins* [1999] shows that in the case of freezing, the temperature gradient near the base is reduced and the value of Π is near zero. In the case of melting, on the other hand, the gradient is enhanced and Π can be very well approximated by $m'H_i / K_i$. Therefore, with the temperature gradient in both cases evaluated, the first term in equation (3.21) is set to zero in the case of freezing while in the case of melting it becomes:

$$\rho_i c_i K_i \left(\frac{\partial T_i}{\partial n}\right)_b = \rho_i c_i K_i (\frac{m'H_i}{K_i}) \frac{(T_i - T_b)}{H_i} = \rho_i c_i m'(T_i - T_b).$$

This relation is derived with the situation of melting at the base of an ice shelf in mind where the far field temperature is always the temperature at the shelf surface which could reasonably be approximated by a fixed average value. However, since a rift or basal crevasse cuts the shelf vertically, it is exposed to a range of far field temperatures at different depths. To account for this, the significance of T_i in the above relation is modified in the rift model. Therefore, inspired by the use of linear ice shelf temperature profiles by investigators such as *Hellmer and Olbers* [1989] and *Scheduikat and Olbers* [1990], the far field temperature profile of the ice shelf is represented by a linear function decreasing from some specified surface temperature to zero at the interface. Each time the gradient at the base is calculated, the shelf temperature corresponding to the specific depth is used.

Frazil crystals: *Jenkins and Bombosch* [1995] thoroughly discuss the manner in which they obtain the equations for the melting and freezing of suspended frazil crystals, assumed to have a cylindrical flat disk shape. They start by writing heat and salt balance equations for single crystals similar to the ones for the melting and freezing at the ice-ocean interface (equations (3.21) and (3.22)). However, they suppose that there is no heat diffusion into the frazil ice and, for reasons discussed below, multiply the left hand side of the equations by a factor representing the surface area of the edge of each disk. During the derivation, the value of the total area of the disc edges per unit volume A_c, which also appears in equations (3.6) and (3.7), is found to be:

$$A_c = \frac{2C}{r}, \text{ where } C = \frac{N\pi r^2 2\varepsilon r}{\Delta V}.$$

The aspect ratio of frazil discs (thickness/diameter) is given by ε, while N is the number of frazil crystals in the reference volume ΔV of the mixture.

The authors make many important assumptions and approximations. One is that all the crystals have the same size and that they continue to do so during the simulation. This implies that freezing is accounted for by increasing crystal number rather than enhancing the sizes of already existing crystals.

Observations [e.g. *Hobbs*, 1974; *Daly*, 1984] that frazil growth velocity along the crystal a-axis is tens of times faster than along the c-axis suggest another assumption. Namely, that heat and salt exchange take place at the edges, rather than the two flat surfaces, of frazil crystals. The analysis by *Daly* [1984] of heat transfer rates for disks supports this assumption.

This analysis is carried out for frazil disks in stagnant water, which is applicable to a good approximation to the crystals of the dimensions of interest to the current study. *Jenkins and Bombosch* [1995] estimate the turbulent dissipation length scale in the plume to be around 1mm, which is much larger than the typical disc thickness of 0.01mm, rendering disk edges oblivious to turbulent fluctuation. *Daly* [1984] cites an unpublished work by *Wadia* [1975] and uses his definition for the characteristic major dimension, $\bar{r}$, of a crystal that has a disk shape:

$$\bar{r} = \left[r\left(r_e + \frac{r}{2} \right) \right]^{1/2},$$

where r_e is one half the thickness of the disk, which *Daly* [1984] considered as the appropriate length scale for heat and salt transfer at its edge. This last author does not explicitly mention how *Wadia* [1975] formulated this definition, however, it is straightforward to show that $\bar{r}$ is actually the radius of a sphere that has the same surface area as that of a disk. The choice of half the disk thickness as the characteristic length of transport at the edges results also from *Wadia's* analysis, who found that, with such a choice, the results agree well with those for the overall transport from a disk. The disk dimensions used in the current study are taken such that $r_e = 0.01r$. Therefore, applying the approach of *Daly* [1984] which consists of writing Nusselt numbers for the edge and the face in terms of r reveals, despite the minor error in the presentation of his results [*Daly*, 1984, page 29], that the heat transfer coefficient at the edge of the disk is indeed 100 times larger than that at the face of the frazil crystal. This explains why the factor A_c appears in equations (3.6), (3.7), (3.14) and (3.15). Since the edges of frazil disks are supposed not to feel turbulence then transfer is taken to be solely by molecular diffusion and the Nusselt number is equal to unity according to its definition given above. Then using equation (3.23) , with the Nusselt number put to one and substituting appropriately for the boundary layer thickness, the term for γ_T^c is found immediately to be:

$$\gamma_T^c = \frac{K_T}{\varepsilon r}.$$

Analogous arguments apply to γ_S^c.

One of the main modifications to the plume model in its application to the rift problem concerns the rate of precipitation of frazil crystals. The explicit treatment of the formation and melting of frazil crystals is one of the innovative features of the *Jenkins and Bombosch* [1995] model and the authors derive in detail the expressions for U_c and W_d. However, as an important simplification, p' is set to zero in the rift model. This implies that frazil crystals formed in the plume are not deposited on the walls of the rift even if the plume velocity fall below U_c. Rather, the crystals remain in the plume until it reaches the top of the water column where they are deposited. This approximation could be justified by examining equation (3.9) which contains the term $\cos\theta$. This angle represents the inclination of the ice-ocean interface surface to the horizontal as can be seen in Figure 3.2. In the rift configuration this angle is 90 degrees or close to it, therefore its cosine is zero or very small.

Entrainment: Equation (3.8) represents the process of ambient fluid entrainment by the plume. It is an application of what has come to be known as the "entrainment assumption". *Turner* [1986] formulates the original form of this hypothesis as follows: "the mean inflow velocity across the edge of a turbulent flow is assumed to be proportional to a characteristic velocity such as the mean velocity over the cross section at the level of the inflow". The proportionality factor between the entrainment and flow velocities is known as the entrainment constant. The author describes how the entrainment assumption and its extensions remain enormously successful in a wide range of applications. The hypothesis is related to the satisfaction of certain similarity assumptions, namely, that the same kind of turbulent structure and balance of forces prevail at each height of the flow. This kind of similarity assumption is not entirely satisfied in the case of a plume in a stably stratified ambient fluid, since plume water spreads laterally once it reaches the point of neutral buoyancy. However, the analysis by *Ellison and Turner* [1959] of this problem shows that the entrainment assumption still satisfactorily holds by modifying the value of the entrainment constant, E_0, to make it a function of the Richardson number, Ri, of the layer where entrainment is taking place. This dimensionless empirical parameter is written in the notation of the current work as:

$$Ri = \frac{g(\Delta\rho)D\cos\theta}{U^2}, \text{where } \Delta\rho = \frac{(\rho_m - \rho_a^D)}{\rho_0}.$$

It represents the ratio of buoyancy to inertial forces. Thus, the role of a stable density gradient in subduing mixing is taken into consideration. On the other hand, it can be seen from the equation above that this role diminishes the nearer the edge of the plume is to the vertical, which is the prevailing condition in a rift. In such a case, the component of gravity perpendicular to the boundary of the flow is too small to be able to significantly alter entrainment. When a plume is more horizontal, the "lifting" of heavier fluid from the ambient water below during entrainment is done against a more pronounced gravity component acting in the opposite direction.

The specific form of the entrainment assumption for the plume model, equation (3.8), is adopted from *Bo Pederson* [1980] and has the advantage of simplicity. It establishes a direct proportional relationship between the entrainment velocity of ambient fluid on the one hand and both the slope and the mean velocity of the plume on the other. However, it is unclear either from *Jenkins* [1991] or *Jenkins and Bombosch* [1995] whether it would also be valid for the slopes encountered in a rift or basal crevasse situation, which are steep (vertical or almost) compared to the gentle slopes ($<10^{-2}$) of the underside of an ice shelf. Furthermore, only for such gentle slopes is it possible to demonstrate that the entrainment constant is a function of the Richardson number. *Bo Pederson* [1980] addresses these questions and clearly states that the relation is valid, as a first approximation, for the whole range of slopes. Further confirmation comes from the fact that *Jenkins* [1993] applied his 1991 model (on which the *Jenkins and Bombosch* [1995] work is based) to the problem of the vertical wall of an iceberg (akin to the vertical wall of a rift) without modification using the same entrainment relation given by equation (3.8).

Since the formulation of *Jenkins and Bombosch* [1995] contains one horizontal dimension, the Coriolis force could not be incorporated explicitly. The authors nevertheless did take account of this force indirectly when in equation (3.8) they argued that the Coriolis force will tend to deflect the flow across the basal slope thus reducing the $\sin\theta$ term. To compensate for this, they decided to adopt half the value of the dimensionless constant parameter E_0 given by *Bo Pederson* [1980].

In adapting the plume model for the rift problem, however, the original E_0 value of 0.072 given by *Bo Pederson* [1980] has been retained. This can be justified by the fact that the flow in the rift situation covers a few hundred meters at most, compared to the hundreds of kilometers in the ice shelf situation, therefore, there is a much smaller chance to considerably reduce the $\sin\theta$ term. The extent to which the Coriolis force is significant in a certain situation can be examined by employing the dimensionless parameter known as the Rossby number, $\Re o$, which gives an idea of the ratio between the inertial and Coriolis forces. Supposing that V is the magnitude, in meters per second, of the characteristic velocity of fluid flow, x is a characteristic distance, in meters, over which this flow is taking place, Ω is the magnitude of the angular velocity, in radian per second, due to the rotation of the Earth (which is a vector that applies everywhere on the surface of the globe maintaining its magnitude and direction) and ψ is the Earth's latitude angle where the flow is occurring, then following *Elder and Williams* [1996],

$$\Re o = \frac{V}{x 2\Omega \sin\psi} .$$

The larger this ratio is, the more realistic it becomes to ignore the effect of Earth's rotation on the movement of the fluid. Substituting with values representative of a rift situation taken from the simulations of the last chapter:

$$\Re o = \frac{0.02}{200 \times 2 \times \left(7.28 \times 10^{-5}\right) \times \sin 70} = 0.74\,,$$

while using values from *Jenkins and Bombosch* [1995] typical of an ice shelf situation gives:

$$\Re o = \frac{0.1}{\left(5 \times 10^{5}\right) \times 2 \times \left(7.28 \times 10^{-5}\right) \times \sin 70} = 1.5 \times 10^{-4}\,.$$

The important difference between the two situations is obviously the result of the big discrepancy in their respective length scales. *Jenkins and Bombosch* [1995] clearly state that ignoring the Coriolis force on the momentum balance is a considerable simplification in the context of the problem they consider but that their main aim is to investigate the interactions between the ice and the ocean, rather than to study the details of ocean dynamics. This is even more so in the rift problem.

3.2.3 Initial plume conditions

For the first plume to start a simulation, the initial values of its flux, velocity, thickness, temperature and salinity should either be assigned or calculated.

Initial plume total flux: In all the simulations and experiments of this work, the initial flux of the plume is assigned a value of 1E-3m^2/s through a cross section that has the thickness of the plume and unity width. This is a rather arbitrary but reasonable choice because it is very small compared to the size of the plume at later stages of its growth. Experiments of the next chapter show that the final flux of the plume when it reaches the top of the water column and starts spreading its water could be at least two orders of magnitude larger than the initial assigned value. Indeed, *Lane-Serff* [1995] describes how he found that variations in the initial flux of water have very little effect on the flow, unless this initial flux is very large.

Initial plume velocity and thickness: The flux is actually the product of the plume's velocity and thickness per unit distance in the direction perpendicular to the plane that contains the s- and n-axes of Figure 3.2. Therefore, once the initial flux is known one can proceed to find the initial values of the latter two parameters.

Equation (3.5) for the conservation of momentum, in which the term $(\rho_m - \rho_a^D)/\rho_0$ is denoted by $\Delta\rho$, can be written as:

$$\frac{d}{ds}(DU^2) = DU\frac{dU}{ds} + U\frac{d(DU)}{ds} = \Delta\rho Dg\sin\theta - KU^2.$$

At the very early stages of the plume it is possible to make the following two assumptions. First, the velocity of the plume does not change much so that dU/ds in the equation above could be set to zero. Second, melting is not yet very active hence the melting rate can be neglected compared to the entrainment rate. With this last assumption, equation (3.3) for the conservation of mass can be used to evaluate the term $d(DU)/ds$ in the above equation, hence:

$$Ue' = \Delta\rho Dg\sin\theta - KU^2.$$

Substituting for the entrainment rate with equation (3.8) gives:

$$U^2 E_0 \sin\theta = \Delta\rho Dg\sin\theta - KU^2.$$

However, during the initial stages of the plume only the flux, DU, is given. Therefore, both sides of the above equation are multiplied by U to obtain:

$$U^3 E_0 \sin\theta = \Delta\rho(DU)g\sin\theta - KU^3,$$

which, rearranged, gives the equation for the initial velocity as:

$$U = \left(\frac{\Delta\rho (DU) g \sin\theta}{E_0 \sin\theta + K} \right)^{1/3}.$$

With both the initial flux and the initial velocity known, the initial plume thickness can be directly found.

Initial plume temperature and salinity: In the investigations of *Jenkins* [1991], *Jenkins and Bombosch* [1995] and *Lane-Serff* [1995], since the models are applied to an ice shelf, the initial flux is taken to be a small flow of fresh melt water emerging at the grounding line from beneath the ice shelf under study. Therefore, the initial plume salinity S_{in} is set to zero and the temperature T_{in} is the in situ freezing point for fresh water. In the current study, however, where rifts and bottom crevasses are not necessarily located near the grounding line, this does not apply. Instead, a formulation provided by *Gade* [1979] and included into the Jenkins-Bombosch plume model is activated to provide the initial temperature and salinity of the nascent plume.

In his work, *Gade* [1979] ponders the question: if ice melts in sea water, then what is the salinity of the resulting mixture? The steady state model that he proposes in response considers an infinitely wide slap of ice floating on a sea of a temperature (which is above freezing) and salinity that are constant far from the ice/water boundary. A laminar layer is assumed to form directly below the interface in which salt and heat are transferred by molecular diffusion. This layer forming between the ice face and the ambient water is the one taken to be analogous to the initial plume in the rift model. The author derives a relation for the salinity of the laminar layer in terms of the ambient temperature and salinity and ice temperature and in doing so he ignores density change due to melting. Using the notation and the coordinate system of the current rift work (where depth becomes more negative downwards) the equation obtained by *Gade* [1979] is:

$$\frac{S_{in}}{S_a} = \frac{(c_i / c_0)(T_i - T_f(S_{in})) - (L / c_0)}{T_f(S_{in}) - T_a + (c_i / c_0)(T_i - T_f(S_{in})) - (L / c_0)}.$$

This is the form of the relation that the author estimates suitable of the case of an infinitesimal boundary layer, which should best approach the situation of the very small starting plume in the rift model. Using equation (3.1) to substitute for the $T_f(S_{in})$ terms and after some algebraic rearrangement a quadratic equation in S_{in} is reached of which only one of the two solutions is valid. Once the initial salinity is known, equation (3.1) can be explicitly employed again to evaluate the initial temperature since the mixture is at the freezing point.

If at the beginning of a run the ambient water is calculated to be already below its freezing point at the bottom of the rift or crevasse then no melting occurs and the simulation is terminated immediately.

3.3 The filling-box concept

A fundamental difference between the rift situation and the configuration of the plume model is in the relation to ambient water. The *Jenkins and Bombosch* [1995] model quite justifiably treats the ambient water as an infinite reservoir whose properties are unaffected by the presence of the plume. In the confined space of a rift, however, ambient water is constantly being turbulently entrained by the plume where it is mixed and then spread as a layer at the top of the water column or at some point below if it becomes neutrally buoyant there. This newly deposited layer forms part of the ambient water which in turn will be incorporated in the plume and so on. Therefore, the modifications of the ambient water properties as a function of time has to be accounted for in the rift model. Clues for this task are provided by the work done in studies of turbulent buoyant convection from a source in a confined region, a set up which *Turner* [1973] designated as the "filling-box" model. The pioneering theoretical and experimental work in this field was done by *Baines and Turner* [1969]. Investigation was later expanded by other workers such as *Germeles* [1975], *Manins* [1979] and *Worster and Huppert* [1983]. The problem they addressed concerns a plume starting from a small source of buoyancy at the bottom of a box filled with heavier ambient fluid. On its way up, the plume entrains this denser fluid. Since the density with depth profile of the ambient water is constant then the plume will always remain buoyant until the top where it spreads a layer of less dense fluid. This layer will be separated from what is beneath it by a front of density discontinuity. As a result, the structure of the ambient fluid is now modified. Below the density continuity, the original ambient fluid remains, while above it, the newly deposited relatively lighter layer. Now that this layer is part of the ambient fluid, the subsequent plume will be entraining the same ambient fluid as the first one only until the density continuity. Above, it will start entraining the relatively less dense liquid deposited by the first plume. Therefore, it arrives at the top of the tank even lighter than the previous plume and spreads another layer on top of the first one with a new density discontinuity front separating the two. The density stratification which results from such a process will obviously be stable. *Baines and Turner* [1969] used the same entrainment hypothesis discussed above in section 3.2.2.

The aspect of most relevance to the rift problem from the filling-box work is the question of the rate of advancement of the new density profile in the ambient water. From the principle of conservation of volume *Baines and Turner* [1969] propose that the upward flux of plume fluid at any height in the box should be equal to the downward flux of ambient water at the same height. That is, using the notation of the current work:

$$U_z D_z = u_{a,z}\left(l_z - D_z\right), \tag{3.24}$$

where U_z is the magnitude of the plume's velocity, D_z its thickness, $u_{a,x}$ is the magnitude of the downward velocity of the ambient water and l_z is the width of the box (rift), all taken at the same depth from the surface z.

It should be noted at this point that one of the assumptions of the *Jenkins and Bombosch* [1995] model is that the ambient water is stationary. To a good approximation, this is not violated by assigning the ambient water a non-zero velocity in the above relation. This can be seen by rewriting this equation as:

$$\frac{U_z}{u_{a,z}} = \frac{l_z - D_z}{D_z}.$$

This shows that since the width of the rift is generally taken much larger than that of the plume, then

$$U_z >> u_{a,z}\ , \tag{3.25}$$

and $u_{a,z}$ can be safely ignored in the momentum equation of the plume. Such an approximation is used by *Baines and Turner* [1969] as well as later workers treating the same problem such as *Germeles* [1975].

The latter author explicitly tackles the incorporation of time as an independent variable in his numerical method for solving the problem. The account *Germeles* [1975] gives of his method is similar in its general approach to the one used in the current rift problem. Thus, the fluid deposited by the plume may be conceived of as occurring in a sequence of time intervals. Each interval creates a new layer of well mixed liquid of a given thickness, salinity (and temperature in the rift situation). After a layer is deposited, it is convected vertically through the liquid of the tank (rift) due to plume entrainment. During the convection, the density of a given layer remains unchanged, while its thickness continuously decreases as a result of the entrainment. At any given time, the position of the different layers determines how much water with a certain set of properties will be entrained by the plume. Therefore, the quantity and properties of the water discharged by the plume are in turn a function of time.

In should be stated here that the lateral spread of the plume when it looses its buoyancy is considered to be instantaneous and that its details of are not considered in the rift model.

As it is explained in the previous section, the plume model equations of *Jenkins and Bombosch* [1995] are derived as steady state: they give the rates of melting and freezing in space at the ice-ocean interface and the resulting characteristics of plume water along its length. By inserting these equations in a structure such as the one described in the preceding paragraph, the rates are used to calculate an evolution in time and plume properties are modified from one time interval to the next.

There are, nevertheless, two important differences between filling-boxes and the rift situation. First, instead of a constant density profile the original ambient water could be already stably stratified. This could lead to a plume loosing its buoyancy somewhere before reaching the top of the water column if it reaches a depth where the density of the ambient water is equal to its own. Second, in the rift situation the plume could be laden with frazil crystals. The presence of ice will then be a source of additional buoyancy for the frazil-water mixture. Once the plume reaches the top of the water column the crystals are upwardly deposited as a result of their lower density. Consequently, It might turn out that the density of the residual water is actually higher than that of the water it underlies. Thus the resulting density structure is unstable. These two possibilities have to be addressed in the rift model and are further discussed below.

3.4 A description of the rift model

In the preceding sections the equations which form the basis of the proposed model are presented and discussed. The current section is dedicated to a more qualitative description of the sequence of events taking place in the course of a standard simulation. This is done with the help of Figure 3.3.

Input information: a program run begins by providing the data set that defines the situation to be simulated. In addition to the initial ambient water temperature and salinity, this also includes the spatial proportions of the rift or basal crevasse. One of the necessary dimensions is the depth at which the top of the cavity is initially located. This does not have to necessarily be sea level as in the case of a basal crevasse that does not reach the upper surface of the ice shelf for example. Therefore, also provided is the actual vertical distance from the top of the cavity to its bottom. In between the two points, the profile of the side of the rift or crevasse is specified since the model can handle initial walls which are inclined as well as vertical ones. However, the wall should not be too far from being perpendicular to the horizontal. Otherwise, some of the approximations made in the previous sections could be violated, concerning crystal deposition during plume ascension for example.

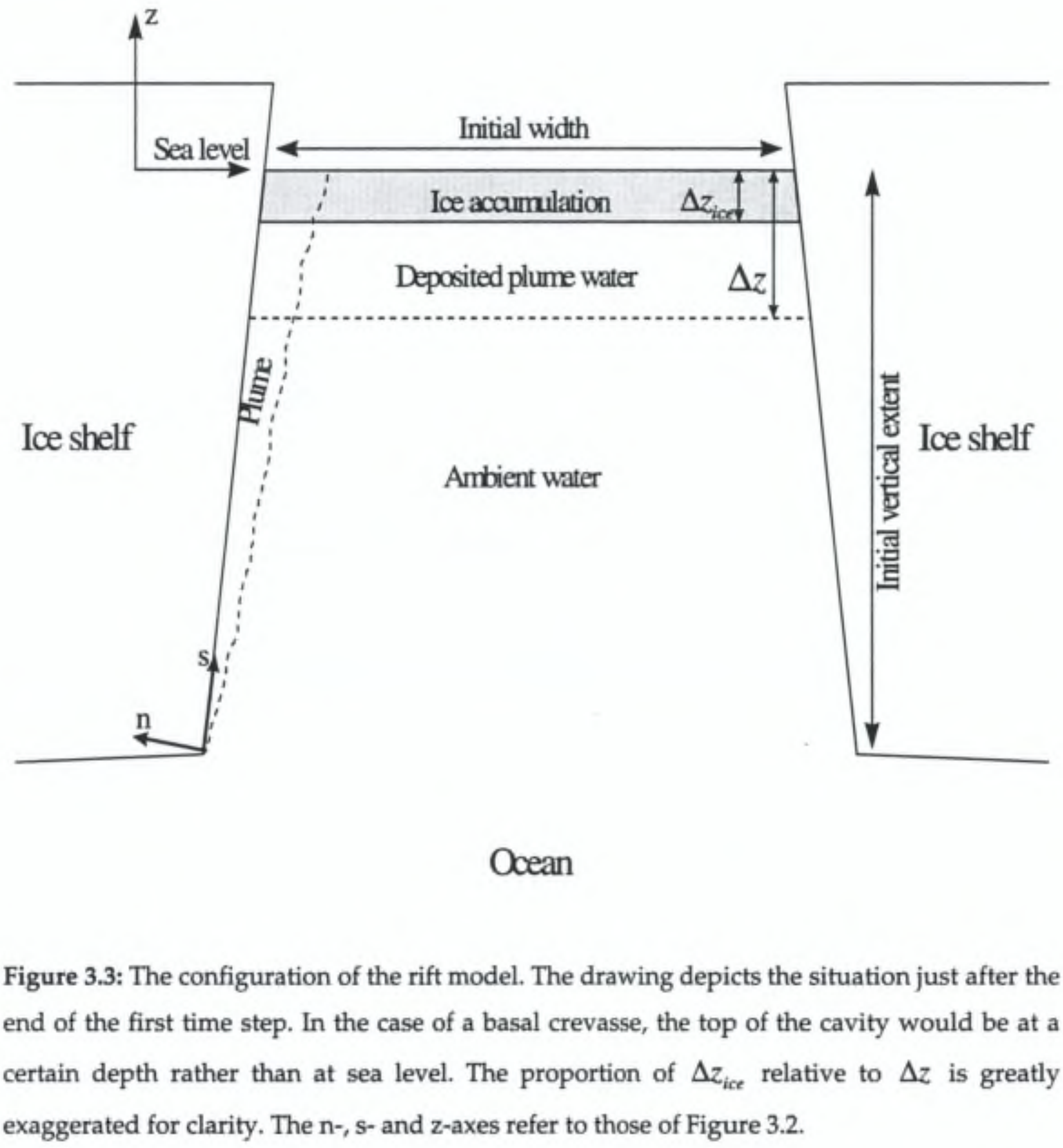

Figure 3.3: The configuration of the rift model. The drawing depicts the situation just after the end of the first time step. In the case of a basal crevasse, the top of the cavity would be at a certain depth rather than at sea level. The proportion of Δz_{ice} relative to Δz is greatly exaggerated for clarity. The n-, s- and z-axes refer to those of Figure 3.2.

Furthermore, initial input also includes the width of the rift or crevasse at its top-most point. The initial width provided as part of the input is at once divided by two and the resulting value, l, is the one used throughout the simulation. This is equivalent to supposing that there are actually two plumes active in the cavity, one at each wall. In the preceding mathematical description of the model there is no physical justification for supposing that a plume forms on one side of the cavity and not the other. Obviously, complete symmetry between the two sides is assumed.

The width of the rift or crevasse at the top cannot be zero (which would give a triangular cavity with a pointed apex) since it has to be much larger than the thickness of the plume, otherwise, inequality (3.25) above is violated.

Finally, the far field temperature profile of the ice shelf is specified. In all the experiments below, a linear function is adopted with temperature increasing from -20°C at the surface of the shelf to 0°C at the ice/ocean interface, as an approximation of the in situ freezing point.

Ice and water deposition: With the above information provided, the simulation commences and a plume is active during the specified time step, Δt. At the end of this period, the plume is allowed to spread its water at the top of the cavity if it manages to ascend to that point. The temperature and salinity of the new layer are those of the plume at the point where it terminates. As for the thickness of the deposited layer, Δz, it is calculated from the equation:

$$\Delta z = \frac{DU}{l - D_h} \Delta t, \tag{3.26}$$

where U is the plume's velocity, D its thickness and D_h the horizontal projection of the thickness, all at the point where the plume terminates. Ice crystals carried by this newly deposited layer are then made to separate from the fluid and aggregate at the top. The thickness of the layer of accumulated ice Δz_{ice}, which is supposed to be homogenous along the cavity's width, is found from:

$$\Delta z_{ice} = \Delta z C, \tag{3.27}$$

where C is frazil ice concentration in the plume by volume at its termination point. Notice that the deposited thickness is that of "pure" ice with interstitial water being considered.

If the ambient fluid is density stratified then there is a possibility that the plume looses its buoyancy before reaching the top of the cavity. In such a case, the water layer is inserted beneath the depth at which the plume stopped while ice crystals are still deposited at the top of the water column. Their thickness is calculated from equation (3.27) also but the final result is adjusted through multiplying it by the ratio of the cavity's width at the top to its width at the depth where the plume stopped. This point is further discussed in the section of the next chapter dealing with ambient water stratification.

Density check: The fact that the plume reaches the top of the cavity does not necessarily mean that its water is less dense than that of the fluid filling the cavity. At that point, the plume is a mixture of water and ice crystals, and it could be that the suspended frazil crystals are the only source of buoyancy for the mixture. *Foldvik and Kvinge* [1974] already give account of such a situation and they designate it as conditional instability, borrowing the term usually used to describe an atmospheric phenomenon. Therefore, once ice crystals are deposited, the density of the new layer of water introduced by the plume should be tested relative to the density of the ambient water beneath it. The model performs such a test each time the plume deposits a new layer using an equation similar to equation (3.2), where the density comparison is done between the two layers in question rather than relative to a reference body of water. If a density stability is discovered, then the new layer and the one below it are mixed. Afterwards, the density of the water resulting from the mixing process is verified relative to the one below it and so on until the whole ambient water column is checked and stabilized. Each time the mixing of two layers is performed, the resulting temperature and salinity are calculated in terms of the relative volumes of the two original layers.

Vertical downward displacement of ambient layers: Ambient fluid could initially be composed of several layers of increasing density from the top, each having its own temperature, salinity and/or thickness. Or the water in the cavity could initially be non-stratified but the plume later adds new layers on top which stay unmixed because of their inferior density relative to what is beneath. When the ambient fluid is already composed of layers then measures should be taken to push each layer down by a suitable distance each time the plume insets a new layer at the top of the cavity. This is done by the means of equation (3.24) from which the velocity of the top and bottom limits of a layer are each found in terms of the plume's velocity and thickness at each depth in addition to the cavity's width there. Once the downward speed of each limit is known, multiplying it by the time step Δt gives the distance by which each limit should be moved. Actually, water layers do not change their position and thickness only in response to the deposition of new layers. It is also a result of the fact that the plume is constantly entraining water from each layer. Calculating the displacement in the manner just described takes account of this since it expresses the conservation of volume at a specific depth.

Modification of cavity dimensions: The vertical extent of the cavity is constantly diminishing as a result of crystal accumulation on top. Therefore, once the thickness of deposited ice is calculated for a certain lapse of time, the vertical dimension is accordingly updated. Furthermore, the width of the rift or crevasse at each depth is always being modified as a result of melting and freezing processes taking place at the wall. The profile of the cavity is consequently modified using the melt rate m', which when multiplied with the time step Δt, gives the distance by which the wall should retreat relative to the vertical (in the case of melting) or advance (in the case of direct freezing) at a given depth. During the course of a run, the profile of the cavity is calculated and updated at equal depth intervals of every 10 meters for the experiments of this study. When the width of the cavity is needed at a point somewhere in between, then an interpolation is employed to obtain the sough after value. This interpolation actually produces a certain model artifact which manifests itself whenever the profile of the cavity is used in a certain calculation through a long-enough time span. Plotting the calculated result as a function of time exhibits a saw-tooth aspect. An example of this can be seen in Figure 4.12a of the next chapter. This occurs because, if the profile is to be calculated at a depth which is located for example in the top-most 10-meter interval, then interpolation is carried out with reference to the values at the upper and lower limits of that specific interval. When a subsequent calculation is required at a lower depth which is located in the next 10-meter interval, then the interpolation uses a new pair of limit values, thus producing a slight discontinuity or jump relative to the values obtained in the first interval.

Output: After the sequence of events described above, a subsequent plume starts a new time step in a cavity that had its dimensions and the temperature and salinity of the water filling it modified by the action of the preceding plume. Therefore, all these updated parameters serve as the input set for the new plume. This continues for the specified run time. At completion, the program outputs the required parameter values. If the simulated period of time is long (tens or hundreds of years) then instead of instructing the program to give the results for each time step (which is mostly set to 5 days) this is instead done for longer time intervals (mostly one month). When this approach is used then some of the values obtained are actually calculated averages of the variable in question for the one-month period. This is notably the case for the plume's velocity, thickness and ice crystal concentration. Ambient temperature and salinity values are those existing in the cavity at the end of each month. Monthly ice accumulation refers to the thickness of ice crystals that is produced and deposited at the top of the water column during each specific month, not to be confused with the total ice accumulation which is the sum of the monthly accumulations.

Code and computer: The rift model is written using version 4.2c of the computer software Matlab. This high-level programming language proved to be very suitable for the task at hand by virtue of its high flexibility in handling matrices and the built-in calculation tools provided. Most input data to the rift model and the representation of the cavity and its properties during simulations take the form of matrices of different dimensions. Throughout the program, parameter interpolation is performed using one of the linear interpolation routines available.

The numerical routines employed to integrate the differential equations of the *Jenkins and Bombosch* [1995] plume model are Runge-Kutta fourth and fifth order methods. These procedures are characterized by the fact that no information is needed to start the integration other than the initial conditions provided. Furthermore, they require only the first-order derivative but produce results

with the same order of truncation error as methods involving higher-order derivatives [*Potter*, 1978]. This relative simplicity combined with high accuracy make the Runge-Kutta methods a popular choice for such applications.
For program runs simulating long periods (decades), run time usually lasts between 7 and 15 hours for each experiment, depending on ambient properties and rift/or crevasse vertical extension. Simulations were carried out on the machines of the Computing Centre of the University of Brussels. These include the *Silicon Graphics Challenge-L* server and the *Compaq AlphaServer GS140* system.

3.5 Limitations and prospective evolution of the rift model

Several limitations are already exposed during the above description and discussion of the rift/basal crevasse model. However, perhaps the most important shortcoming of the model is the fact that it does not include a treatment for the closing or further opening of the rift or crevasse due to shelf flow during the time period being simulated. There are a number of reasons for this omission. The least consequential is that in almost none of the rift/basal crevasse field observations used in the next chapter to force the model are the necessary information about closure or opening rates provided. Most importantly, however, is not being able to predict how the accumulation of crystals in the cavity would affect or react to the closure or further opening of the cavity in which it had formed. This is related to the question of the nature of the interaction among frazil crystals in saline water. If crystals remain as a loose aggregate then a widening or narrowing rift will just redistribute them vertically. In contrast, if frazil shows cohesiveness and crystals join together to form a structure with solid properties, then perhaps accumulating ice could be capable of resisting or even stopping a rift from further narrowing, even before the ice crystal/water mixture is fully consolidated. The available evidence on the cohesive tendencies of frazil crystals in saline water is contradictory. Experimenting on water with 35.5 salinity, *Martin and Kauffman* [1981] report observing crystals easily joining together to form clusters. *Hanley and Tsang* [1984] on the other hand, strongly dismiss this possibility and describe how their experiments show that frazil forming in saline water shows a lack of adhesiveness and cohesiveness. They explain this by the rejection of salt when a crystal forms which lowers the freezing point at its edge and limits further growth. Drawing a conclusion is complicated by the fact that the experiments of *Hanley and Tsang* [1984] are conducted at a salinity of 44 which is much higher than the 34 to 35 salinity range of interest for this study.

The model also suffers from what *Williams et al.* [1998] describe as the summer bias of the field observations used in testing it; a problem shared with all other ice shelf/ocean interaction models.

A very interesting extension of the current model would be to include a treatment for the properties of the ice forming as a result of the process investigated here. Work described in the first chapter shows the importance of parameters such as the salinity and heavy-isotope composition in recognizing marine ice. Furthermore, a rift model that is also capable of predicting such properties could be even more thoroughly verified by comparing its output with observed ice salinity and isotopic composition. Such an undertaking, however, entails addressing the complex question of the consolidation process.

Little is known about the actual process by which a mixture of a more or less loose aggregate of frazil crystals immersed in a body of host water is transformed into a mass of marine ice. The field observations and analyses results of the recovered marine ice samples presented in the first chapter suggest that the main mechanism of this transformation is the advancement of a freezing front into the frazil/water mixture. Upon the freezing of interstitial water, most of the salt content is expelled into the water beneath, while the resulting ice is enriched in the heavy stable isotopes of oxygen and hydrogen. A prospective model would attempt the construction of a mathematical model of the consolidation of a frazil/water slush in a rift/basal crevasse, integrating the principal implicated physical processes. These include the extent of convection due to density instability. The water layer at the freezing interface should become denser than the underlying water because of the addition of the rejected salt. However, increased salinity also works to lower the freezing point which could result in frazil ice melting. This in turn could have two opposing effects on the density: added fresh melt water would decrease it while reduced temperature would increase it. All these opposing effects on the density are further modulated by the rate at which interstitial water is squeezed out from between the crystals by the compaction effect of accumulating new crystals below. The enhanced pressure resulting from this compaction could also have an effect on the melting point of layers located higher in the water column. Porosity in turn would certainly be affected by any changes in the size of frazil crystals due to freezing/melting and how close together they could be arranged. This discussion makes it obvious that one of the important tasks of such a model would be to accurately determine the rates at which all these interdependent processes occur: the advancement of the freezing front, convection, rate of accumulation of new crystals and the rate of their freezing/melting. The relatively sheltered environment of an open rift or basal crevasse makes it easier to assume that mass and energy exchanges between frazil crystals and the surrounding water occur in a non-turbulent manner. Another particularity of the rift situation, compared to that of the sub-ice shelf cavity, is its proximity to the surface.

There are certainly differences in the situation of marine ice forming at a depth of hundreds of meters beneath an ice shelf and that forming relatively nearer to the surface in an open rift or a bottom crevasse. However, both manifest not yet fully understood low salinities. A consolidation model could help shed some light on the question, including for the sub-ice shelf marine ice. Constructing such a model is certainly beyond the scope of the current work, but it is quite a natural future continuation of it.

Chapter 4

Rift model: Sensitivity study

The model presented in the previous pages is now tested in a series of control experiments. Model behavior and dependence on several parameters are investigated by applying it to a suitable observed situation. The examined parameters include the stratification of ambient water, ambient temperature and salinity, the entrainment constant, cavity dimensions and crystal size. From this first group of experiments, one combination of parameters is chosen to be used during a second main set in the next chapter which is composed of model application to different natural situations described in the literature.

The work of *Orheim et al.* [1990] and that of *Osterhus and Orheim* [1992] provide an observed data set which is relatively, so far, the most detailed available in the literature for initial testing of the model.

The observations of these authors are discussed in detail at the beginning of the next chapter. For the time being, based on the information they provide, a rift having an initial vertical extent of 300 meters and initial width of 340 meters is simulated in the following experiments. Unless otherwise specified, this rift is filled with ambient water at an initial temperature of -1.89°C and initial salinity of 34.38.

The model output ambient temperature, salinity and ice accumulation are compared to the observations of *Orheim et al.* [1990] and *Osterhus and Orheim* [1992] which are summarized in the last row of Table 4.1.The model produces parameter values using four decimal places, while observations are most often provided with two such places. Therefore, during comparisons, model output is rounded to two decimals. Consequently, model output temperature is considered to agree with observation if it falls between -1.9750 and -1.9649°C and output salinity between 34.3350 and 34.3449. However, when comparing two sets of model results, the comparison is made using four decimal places.

In many cases, the model is run to simulate 50 years (each composed of 12 months, each month containing 30 days) which are continued later for up to 250 years according to need. Use of shorter periods is explicitly indicated. Generally, a time step of 5 days is specified.

4.1 Ambient water salinity stratification

In these experiments, the model is tested according to the degree of stratification of the ambient water column at time zero. The value of the entrainment constant E_0 is fixed for the time being at 0.072 as discussed in section 3.2.2, and this choice is further tested and justified below. As is the choice of frazil crystal diameter set at 2.2mm for the sake of this test. Other than deciding the question of what degree of stratification to use in the following simulations, this series of experiments also serves to present different features of the plume and the effects its action has on the water of the cavity.

The starting assumption is that water properties observed at the sea bed by *Orheim et al.* [1990] (Figure 5.1) represent the original state of water before the beginning of rift plumes. Therefore, the salinity of the initial water column at 400 meters is assumed to be 34.38. Salinity gradients with depth for HSSW of 1.75E-4 and 1.5E-4 given respectively by *Jenkins* [1991] and *Bombosch and Jenkins* [1995] are used as guides to constructing stratified water columns. Hence, if the water were continuously stratified then its salinity at the lower end of the rift at 300 meters depth would be 34.37 further decreasing to 34.32 at the top. The model handles such gradients by treating the properties of the water column as a step function with the depth divided into finite length sections each having its temperature and salinity. Hence, the larger the number of steps the closer one gets to more accurately simulating what is supposed to be a smooth gradient. In three of the current experiments, a water column with salinity 34.37 at 300 meters depth was divided into six, four and two equal-length sections, each representing an equal step in salinity. In the fourth experiment, the whole water column was set at a salinity of 34.38. This is equivalent to assuming that the rift has opened and filled rather quickly with the pressure of gushing water providing the energy to fill the rift up with "heavy" water, and that plumes started before any significant stratification could take place. In all the simulations, temperature is kept constant throughout at -1.89°C, which is the temperature at the sea bed as can be seen in Figure 5.1.

4.1.1 Results and discussion

At the end of 50-year runs, all four experiments result in a one-layer water column. Table 4.1 gives a summary of output temperatures, salinities and total ice accumulations. It can be seen that with increasing number of layers, salinity decreases, temperature increases and total ice production is rather stable. In order to explain these observations, the progression of plumes in such a stratified environment is first examined.

In his investigation of the flow of melt water beneath ice shelves, *Lane-Serff* [1995] further explores the basic features of the *Jenkins* [1991] model. The author describes how the flow of the plume can be divided into two regions. The first, where melting is important and the addition of melt water (as discussed above in section 3.1) serves to reduce the density of the flow thus enhancing its buoyancy, and the second, where freezing takes place and buoyancy is gradually diminished.

In the current experiments, the plume starts at the lower end of the rift (at 300 meters depth in this case) by entraining ambient water which is above the in situ melting point. The lower region of the rift is therefore a strong melting zone.

Melting works to progressively push the temperature and salinity of the plume towards the in situ equilibrium conditions.

no. of layers	*temperature (°C)*	*salinity*	*total ice (m)*
6	-1.9698	34.3047	31.3495
4	-1.9703	34.3134	31.4909
2	-1.9707	34.3200	31.5193
1	*-1.9719*	*34.3415*	*31.5453*
values from observations at Jutulgryta	-1.9750 to -1.9649	34.3350 to 34.3449	approx. 25

Table 4.1: Final output data for different degrees of water column stratification. All are 50-year runs. The one-layer case is not a direct continuation of the other three. For comparison, observed parameter ranges from the Jutulgryta rift are included in the last row.

A salinity step in an isothermal water column also represents a density discontinuity. This discontinuity becomes a barrier to the ascending flow if the density of the plume is greater than that of the water laying above the step. Consequently, the plume looses its buoyancy thus terminating at the barrier and spreading its water to fill the part of the water column that lies below the step. This newly deposited body of ambient water has lower density by virtue of its lower salinity. The next plume will therefore be entraining water which is less dense while at the same time also incorporating melt water. When this plume in turn arrives at the same salinity step it will have lower density than its predecessor. However, if this density is still higher than that of the water above the step, the plume will again terminate there and spread its water to form the new body of ambient water in the part of the rift situated below the step. The process is repeated until the density of the ascending plume is finally lower than that of the water in the layer above the salinity discontinuity. At that point, the plume is able to breakthrough the density barrier continuing to ascend in the region occupied by the next water layer until it reaches the next salinity step. The same previous sequence of events is therefore reproduced.

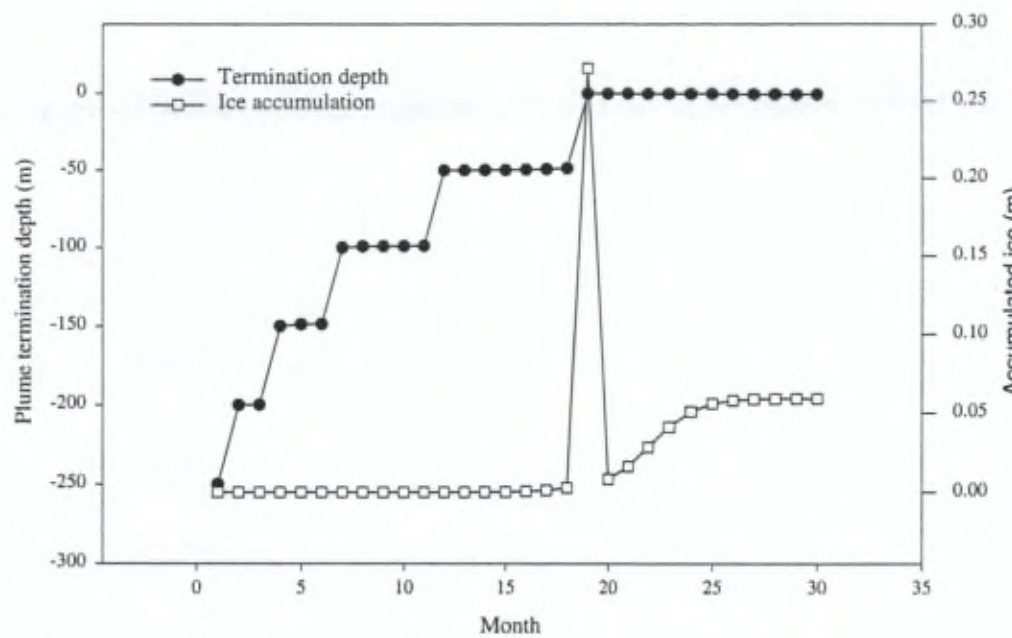

Figure 4.1: Depths at which plumes are stopped by density steps in the water column composed of six layers for the first 30 months of the experiment (time step is on month). Thickness of ice accumulating at the top of the water column (for each time step) for the same case shows the big jump associated with the break through of the last salinity step .

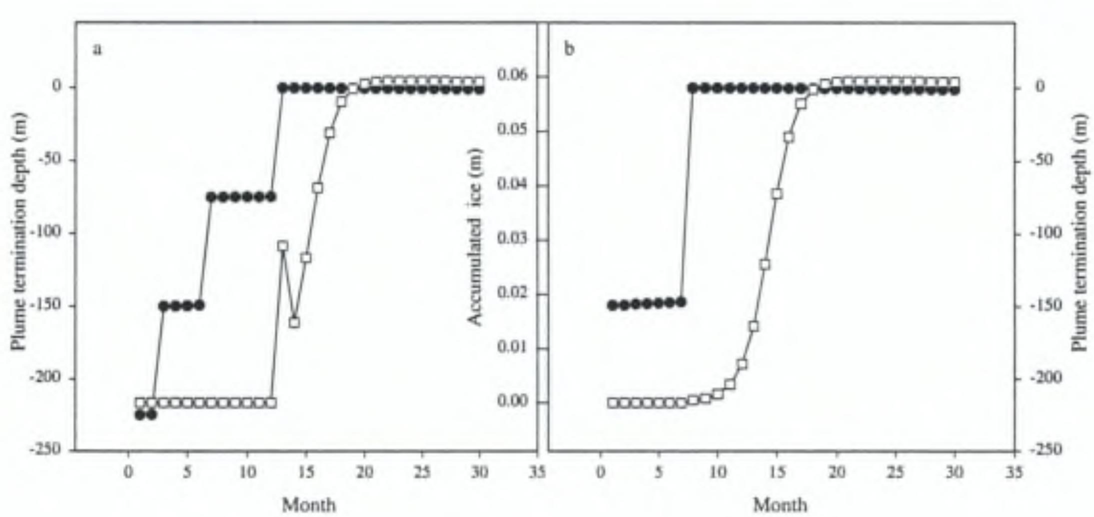

Figure 4.2: Depths at which plumes are stopped by density steps (black circles) in water columns composed of (a) four layers and (b) two layers and corresponding thickness of ice accumulation (open squares). Ice thickness scale in the middle applies for both plots.

The fact that salinity steps in the experiments are equal, and that the density of the plume when it breaks through one density barrier has dropped to the density of the above-lying layer or lower means that when the plume arrives at the next step higher in the water column the density difference to surmount is the same if not lower. However, as can be seen from Figures 4.1 and 4.2b, the higher the salinity step in the water column, the longer the plume needs to go through it. This can be explained by two related factors. The first is that melting rates slow down higher in the water column. This is because the in situ freezing point increases with decreasing depth (pressure) as discussed in section 3.1 above. Furthermore, as *Lane-Serff* [1995] describes, the thickness of the plume increases during its ascension thus increasing the amounts of heat and salt exchanges (through entrainment and melting) necessary to maintain the state of the flow. This, combined with an increasing in situ freezing point with less depth, means that the sensible heat provided by entrainment progressively diminishes and eventually stops thus driving the plume into the second region where it becomes supercooled [*Jenkins*, 1991]. Consequently, when salinity steps are lower in the water column, plumes active beneath them will be in a zone where melting rates are higher, thus taking less time to reduce the density of the plume enough as to be able to overcome the density barrier. The other factor to explain why breakthrough time increases for density steps at shallower depths is the continuous modification of ambient water properties as a result of water deposition by successive plumes. This results in the temperature and salinity of the ambient water evolving in such a way as to slow the melting rate. This process is examined in more detail in the discussion of the entrainment constant below. A sure indication of the occurrence of melting is a decrease in temperature associated with a decrease in salinity since heat is consumed to melt ice, thus adding fresh water to the mixture. Figure 4.3 shows the general tendency of the temperature and salinity of water in the current to decrease with time before the breakthrough point. It also shows how the gradient of this decrease becomes lower with time indicating a slowing of the effects of melting.

The above description of the two regions that comprise a plume path are also the key to explain why the total produced ice quantity is rather stable regardless of the number of layers in the water column. This is mainly because ice production takes place in the second region where the plume becomes supercooled. For the reasons that are presented above, this zone occupies the top portion of the water column. Therefore, for the most part, plumes are still in their melting phase before they breakthrough the last density barrier, especially in the cases of the two- and four-layer water columns. It is clear from Figures 4.1 and 4.2 that the bulk of ice production takes place after this last barrier is cleared and the ambient water is homogenized and is henceforth composed of one layer in all experiments.

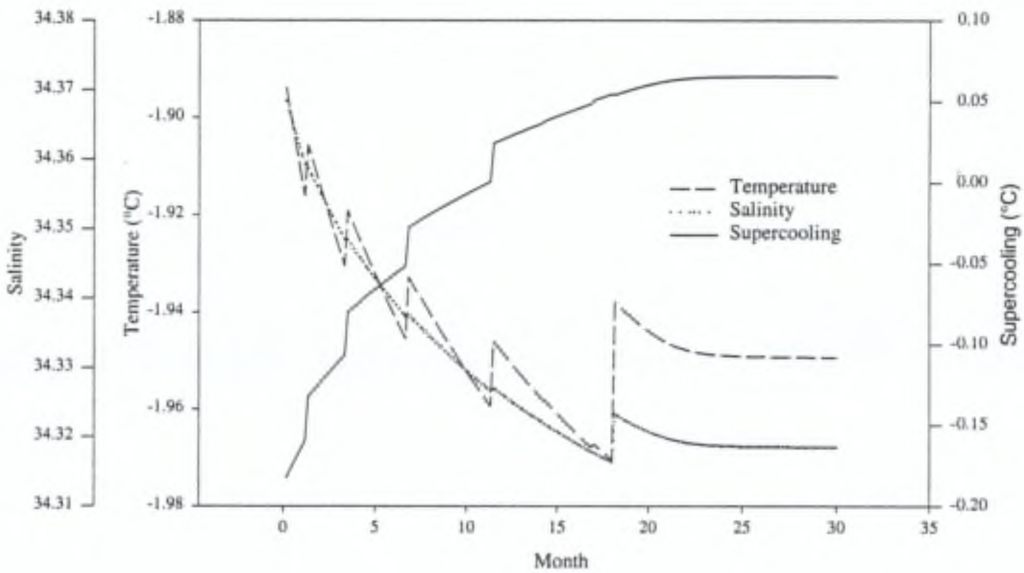

Figure 4.3: A detailed look (time step of 5 days) at the evolution of the temperature and salinity of plume water at depths where it ends (which is also the water deposited in the cavity beneath these depths) for the first 30 months of the six-layer experiment. Supercooling (expressed in positive values when plume temperature is lower than the in situ freezing point) is also calculated each time at the depths where the plume terminates. It can be seen how after going through each density barrier the temperature leaps. This is because at that point the plume starts entraining the yet unmodified warmer water above the step since temperature is not stratified. However, the higher jump at the last step cannot be explained by that alone and is also the result of high ice production, which also produces a noticeable salinity increase at the same point.

In summary, the main difference between the three experiments, namely the degree of stratification, had already been removed before any substantial ice generation has begun, thus minimizing the differences in the final amount of ice accumulating.

However, as can be seen from Table 4.1, despite the small differences in the total amount of ice, there is a consistent tendency of less total ice with increased number of layers. This can be explained, at least for the preliminary stages of the experiments, by the time necessary in each case to overcome all the salinity steps. Figures 4.1 and 4.2 show that the larger the number of layers composing the water column, the larger the number of months needed to go through them, hence the later plumes are able to access the higher parts of the cavity where they get the chance to become supercooled, and thus the shorter the span of time they have to produce ice.

Longer time is the expression of not only the need to go through a larger number of density steps. It is also the consequence of what can be considered, at least partially, a model artifact. This could be demonstrated by contrasting, for example, the four-layer and the two-layer experiments. In both situations, the salinity at the mid point in the water column (at 150 meters depth) is the same and equals 34.3450. This is expected since the same salinity gradient is used to obtain these values. However, in the four-layer case, there is still another layer to insert between the mid point and the surface using the same gradient. This results with a salinity step at depth 75 meters that is associated with a salinity value of 34.3325 while in the two-layer case all of the cavity half above the mid point is maintained at a salinity of 34.3450. The result is that in the four-layer case, plumes not only have to go through a larger number of density barriers, but also the overall salinity difference they have to overcome is larger (34.3700 at the bottom minus 34.3325 at depth 75 meters) compared to the two-layer case (34.3700 at the bottom minus 34.3350 at depth 150 meters).

In addition to explaining the different homogenization times needed, the model artifact described above is also at the origin of the decrease of output salinity with increased stratification shown in Table 4.1. From the outset, cavities with a higher number of layers have longer sections of their water columns at lower salinities, especially towards the top. This initial difference reproduces itself in the final outcome.

The final outcome temperature is in turn related to the salinity. The study of *Lane-Serff* [1995] is illuminating in this regard. Through this author's approach it is possible to see how the fluid in the plume is in a constant process of trying to approach local (depth dependent) equilibrium values of temperature and salinity. Through the dependence of the freezing point on salinity, water with lower salinity has a higher freezing point as equation (3.1) indicates. In the higher stratification situations, where salinity is lower, the water in the current will generally be tending towards higher temperatures, which manifests itself in the final results as increasing temperature with increased stratification.

It is interesting to notice from Figure 4.1 how ice production jumps significantly after crossing the last salinity step in the case of the six-layer water column. Figure 4.2 shows a similar jump for the case of the four-layer stratification, but with a much lower magnitude, while no jump takes place for the two-layer case. This can be partially explained by the larger size of the breakthrough plume at the top in the case of higher stratification, with 17.5572 meters for the six-layer case just before breakthrough and 15.3964 meters for the four-layer case, so even if the plume contains the same fraction of frazil crystals, a larger plume will deposit more ice in absolute terms. However, the main reason must be the fact that breakthrough takes place after different lapses of time. In the six-layer situation, it takes longer to overcome the last salinity step as discussed above. This entails more plumes being active in an environment in which melting is generally the dominant process, which can be inferred from Figure 4.3. Therefore, the plume which achieves the breakthrough tends to have a higher degree of supercooling thus producing larger amounts of ice once it has access to the upper parts of the cavity where this supercooling can be more effectively released. Thus, in the six-layer case, at a depth of 43.0555 meters, where the last density step is, the plume which is about to go through it has a salinity of 34.3162 which according to equation (3.1) has an in situ freezing point of -1.9159°C. This is higher than the plume's actual temperature of -1.9710°C resulting in a supercooling of 0.0551°C. Figure 4.3 clearly shows how supercooling in the plume continues to build up to the point of breakthrough then stabilizes afterwards. An analogous calculation in the case of the four-layer experiment (in which the last step is at 74.3097 meters depth and the temperature and salinity of the plume at that point are, respectively, -1.9613°C and 34.3287) gives a supercooling of 0.0209°C. In the two-layer case, the only salinity step is at 146.239 meters depth before being finally passed by a plume that has a salinity of 34.3414 and a temperature of -1.9594°C which reveals that it is not supercooled at all and is actually 0.03645°C above the in situ freezing point.

It is interesting to point out, however, that after the breakthrough point in the six-layer experiment, the total amount of ice produced since the first month, 0.2769 meters, is close to the 0.2733 meters produced in the four-layer case during the same period. As if the plume in the former case catches up by finally accessing the upper part of the cavity and releasing its built up supercooling. Despite the lead at this point in ice production for the six-layer case, the lower initial stratification experiments produce a higher final total amount of ice as noted above. This is related to the above-mentioned trends in ambient water properties which favor more ice production in these cases. A glimpse of the effect of the ambient temperature and salinity on ice production can be seen in Figure 4.1 where in the six-layer experiment the marked jump in produced ice is followed by sharp drop in the subsequent month. What has changed is that the subsequent plume was entraining ambient water which is the product of the breakthrough plume. The temperature and salinity of the latter were strongly modified by its high production of ice which adds both heat and salt to the water. Figure 4.4 shows how changes in the temperature and salinity follow closely the fraction of frazil in the current. Consequently, the ambient fluid entrained by the following plume is warmer, which means water in the plume will be relatively less supercooled. Thus, for the first plume after the breakthrough, at 49.7855 meters depth, the closest to the breakthrough depth with output data available, salinity is 34.3229 and temperature is -1.9386°C. This results in a supercooling of 0.0172°C compared with 0.0515°C for the breakthrough plume at a comparable depth.

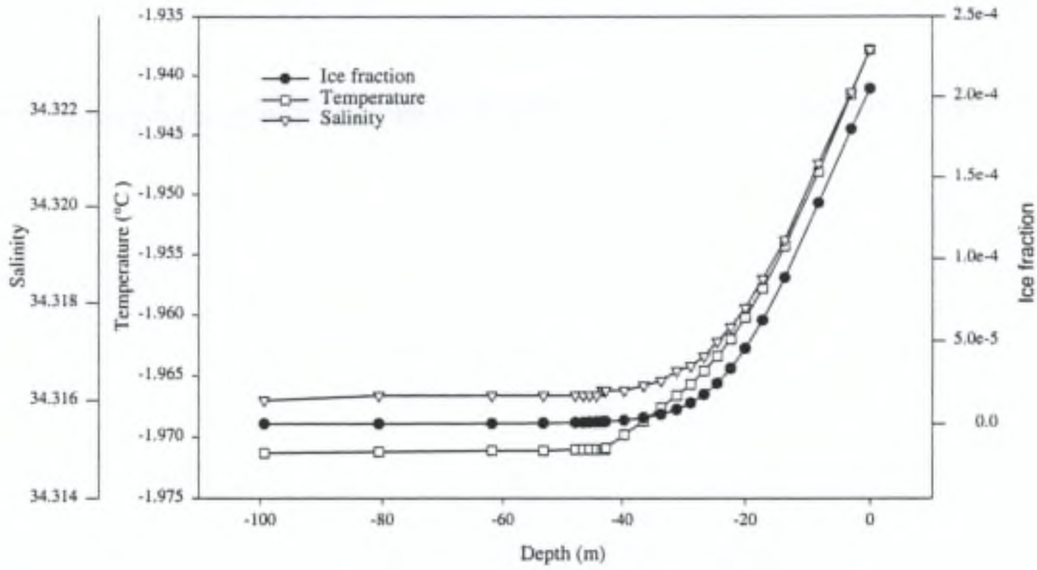

Figure 4.4: A closer look at the plume that finally breaks through the last salinity step (at 42.9174 meters depth) during the last 100 meters of its path in the six-layer case. Notice the great increase in the ice fraction after breakthrough and how plume temperature and salinity follow.

This is a good point to discuss the question of ice crystals drifting upwards to accumulate on the ice-water interface when plumes stop somewhere below the top of the water column upon losing their buoyancy which, for example, occurs in the current experiments at the salinity steps. At such points, the plume stops and spreads its water filling the cavity below while the crystals float to the top in the ambient water above the plume-termination point. The properties of the ambient water are obviously different from those of the plume and the crystals will react differently when subjected to them. *Bombosch* [1998] addresses just this question through his one-dimensional model concentrating on the development of a mass of ice crystals rising through a water column under the influence of gravity. The conclusions of the author show that this interaction has important consequences for the ice crystals themselves, which may melt or increase in concentration and, consequently, on the properties of the surrounding ambient water. The current rift model does not take this into account and plume-generated frazil crystals are deposited as they are on the top of the cavity.

However, the discussion above shows that in this series of experiments, negligible ice production takes place before the breakthrough (and only in the six-layer situation). Most of ice is produced when the water column has already been homogenized and plumes continue all the way to the top and thus deposit their crystal loads directly.

4.1.2 Conclusion

During the above discussion different aspects of plume behavior are examined. The main immediate conclusion concerns the degree of stratification of ambient water to use in the other experiments. The water column with the highest number of density steps, six in this series of experiments, is the one that would best approach naturally occurring stratification. From Table 4.1, however, it can be seen that the output salinity value is far from the one observed in the rift of Jutulgryta. From the same table, the experiment with no stratification emerges as the one that produces the closest fitting results. Consequently, this setting is used in all the experiments below. This is equivalent to supposing either that rift or crevasse opening had happened rather suddenly or that plume circulation in the cavity started before the ambient water had enough time to stratify, or both. Now that plume behavior in a step-stratified environment is exposed, using non-stratified ambient water columns for the rest of the experiments has the added advantage of simplifying the task of analyzing their outcomes. Another important consequence of working with non-stratified ambient water is that the plume never looses its buoyancy. This happens because in such a situation it is constantly entraining water with the same higher density; thus, while its own density increases, it never exceeds that of the ambient. The plume only stops when it reaches the ice/water interface at the top of the cavity.

In addition to understanding plume interactions in an environment where the stratification is a step function, the above discussion also highlights the need to take a closer look at the relation between ambient temperature and ice production. This question is addressed in the following section.

4.2 Effects of ambient water temperature and salinity on ice production

In the *Jenkins* [1991] investigation of plumes beneath ice shelves a simulation is undertaken to examine the effect of a 0.6°C increase in ambient water temperature on the current's interaction with the bottom of the ice shelf. The result is that the plume never enters the freezing zone and continues melting ice almost all the way to the surface. In the current study, however, situations arise where the ambient temperature and salinity are actually reduced, or the water even becoming supercooled, due to the action of the plume itself which is "recycling" fluid in the cavity. Such a situation appears in the series of experiments presented in the previous section and in other simulations below. It is therefore the aim of this section to investigate how ambient temperature and salinity modify ice production in the rift/crevasse problem.

In this context, it is useful to adopt the concept of ambient freezing point, z_{amb}, which is introduced by *Lane-Serff* [1995]. This is defined as the vertical depth where the ambient sea water would freeze based on the pressure freezing relation (equation (3.1)) and the temperature and salinity of the ambient water. Thus, using equation (3.1) it is possible to obtain:

$$z_{amb} = \frac{T_{amb} - aS_{amb} - b}{c}, \tag{4.1}$$

where T_{amb} and S_{amb} are, respectively, the ambient temperature and salinity of the water in the rift or crevasse.

That a body of sea water could still exist in liquid form while having a temperature below the local freezing point can be already seen from Figure 5.1 where the water in the Jutulgryta rift is supercooled between 50 and 120 meters depth. *Hobbs* [1974] excludes the possibility that large quantities of water could be cooled far below freezing without initiating ice formation. This is not contradicted by *Daly* [1984] who actually emphasizes the low levels of supercooling found in nature. *Martin* [1982] cites observations from river research of frazil ice beginning to form at around 0.1°C degrees of supercooling. On the other hand, *Weeks and Ackley* [1982] estimate that supercooling levels of a few hundredths to tenths of a degree Celsius could be found in sea water. But perhaps the most pertinent evidence comes from the work of *Penrose et al.* [1994]. These authors realized conductivity-temperature-depth (CTD) measurements in Prydz Bay off the Amery Ice Shelf, East Antarctica. Their results reveal the presence of supercooled water over an extensive depth portion of the water column, from about 20 meters below the surface down to about 220 meters depth. Supercooling was about 0.10°C reaching 0.12°C at some points. *Penrose et al.* [1994] also describe the "sustained character" of the supercooling of this body of water. In the experiments of this section initial supercooling levels never exceed 0.2132°C, while for the simulations below its maximum value is 0.1760°C, which occurs in the case of the rift in the Ronne Ice Shelf at the top of its water column. In these experiments and simulations, since ambient fluid is taken to be of uniform temperature and salinity, supercooling starts occurring at the ambient freezing depth and increases steadily until reaching its maximum value at the top of the cavity.

In the experiments here, the Jutulgryta rift is simulated with the initial ambient water salinity set at 34.3800 as inferred from the observed data, while the initial ambient temperature is varied between -1.9000 and -2.1000°C by 0.0250°C increments. Below -2.1151°C the ambient water would be already supercooled at the lower end of the rift, thus no melting would occur and a buoyant plume would not form. All runs are for the duration of one time step simulating five days.

4.2.1 Results and discussion

Figure 4.5a shows how the quantity of accumulating ice rapidly increases with decreasing temperature after dropping below a certain temperature. The temperature corresponding to the point where ice production begins to pick up, -1.9500°C, is then fixed and salinity allowed to change between 33.0000 and 35.0000 by increments of 0.2000 as shown in figure 4.5b. This is the range which encompasses most of the salinity values cited in the literature on Antarctic ice shelf research. In this case, ice accumulation for a run composed of a single time step also increases below a certain salinity in a similar manner to that of variable temperature but on a smaller scale.

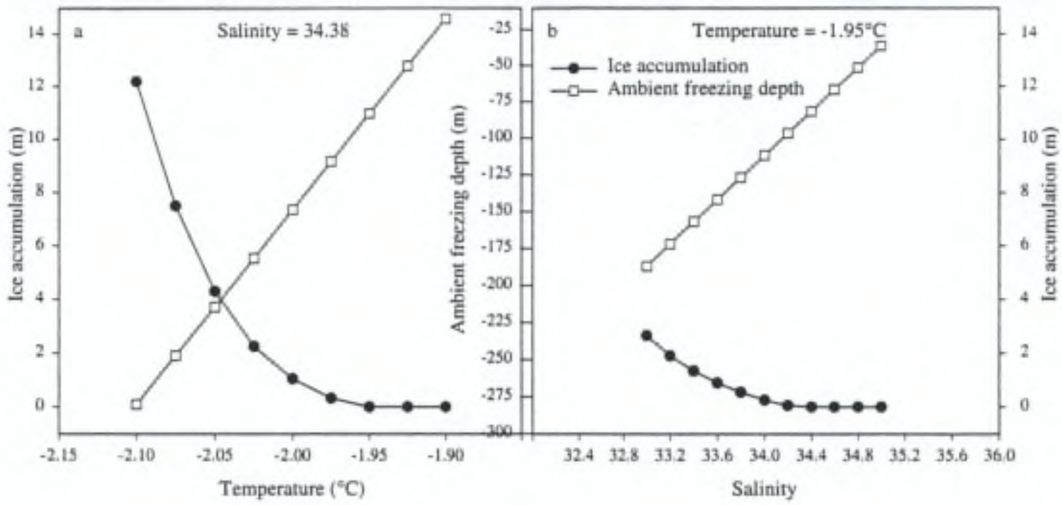

Figure 4.5: (a) Ice production and ambient freezing depth as a function of ambient temperature at a fixed ambient salinity. (b) Ice production and ambient freezing depth as a function of ambient salinity at a fixed ambient temperature. Ambient freezing depth scale in the middle as well as the legend apply to both plots.

In order to understand these observations, a first step is to examine the effect that the changes in ambient temperature or salinity have on the ambient freezing point. This is also plotted in Figures 4.5a and 4.5b. The resulting relation is linear as expected from equation (4.1) and it can be seen that, in both cases, deeper ambient freezing depths are associated with higher ice outputs. Furthermore, these plots also reveal why temperature change would have a more dramatic effect on ice production. This is due to the fact that in the respective ranges of temperature and salinity considered for this experiment, temperature change is resulting in a much higher variation in ambient freezing depth extending between 17 and more than 280 meters depth. Change due to salinity variation on the other hand is confined to the 150 meters below 36 meters depth.

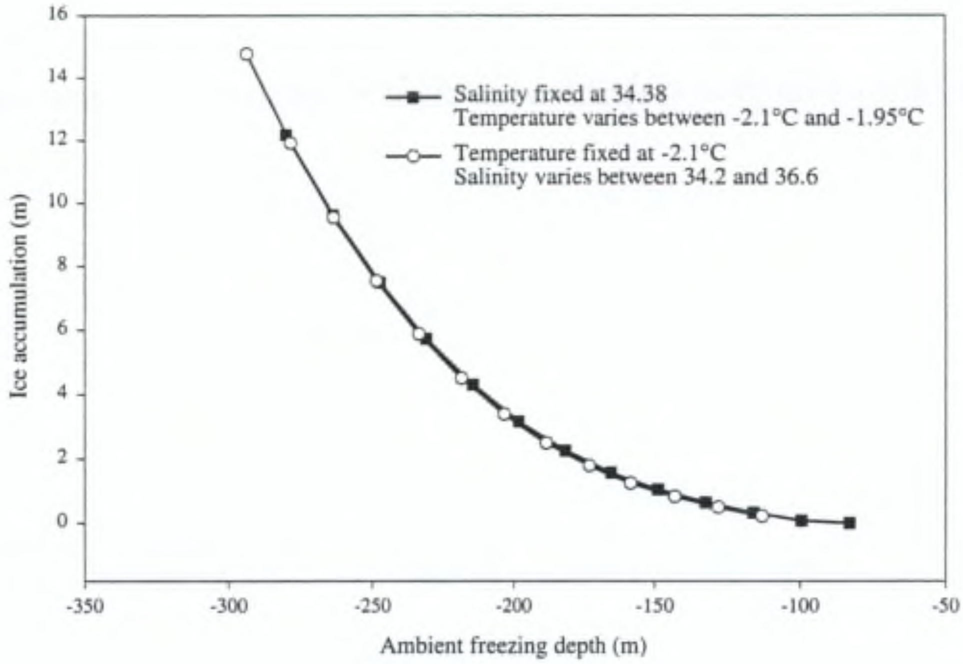

Figure 4.6: A comparison of ice output as a function of ambient freezing depth for the first time step among points, each of which representing a different combination of temperature and salinity. Notice however how ice accumulations are the same for points having the same ambient freezing depth.

In Figures 4.5a and 4.5b there is already a hint that, in both cases, equal ambient freezing depths correspond to equal quantities of generated ice, but the narrower range of ice accumulation in Figure 4.5b makes the comparison difficult. Therefore, to test this idea, the ice production of Figure 4.5a, where salinity is fixed and temperature varies by increments of 0.0125°C, is first plotted against the ambient freezing depth. Then, this is compared to an opposite situation where the ambient temperature is fixed at -2.1000°C, which corresponds to the highest ice production in Figure 4.5a, and salinity allowed to vary between 34.2000 and 36.6000 by increments of 0.2000, thus creating a wider range of ice accumulation. The results are plotted in Figure 4.6 and it can be clearly seen that ambient freezing depths produce the same quantities of ice in both situations. In other words, two different points, each corresponding to a different combination of temperature and salinity are nevertheless associated with the same ice output if they have the same ambient freezing depth.

The preceding remarks makes it possible to hypothesize that changes in ice production induced by variations in temperature or salinity actually have the same underlying mechanism: it is through modifying the ambient freezing point that a change in either parameter influences the quantity of ice deposited.

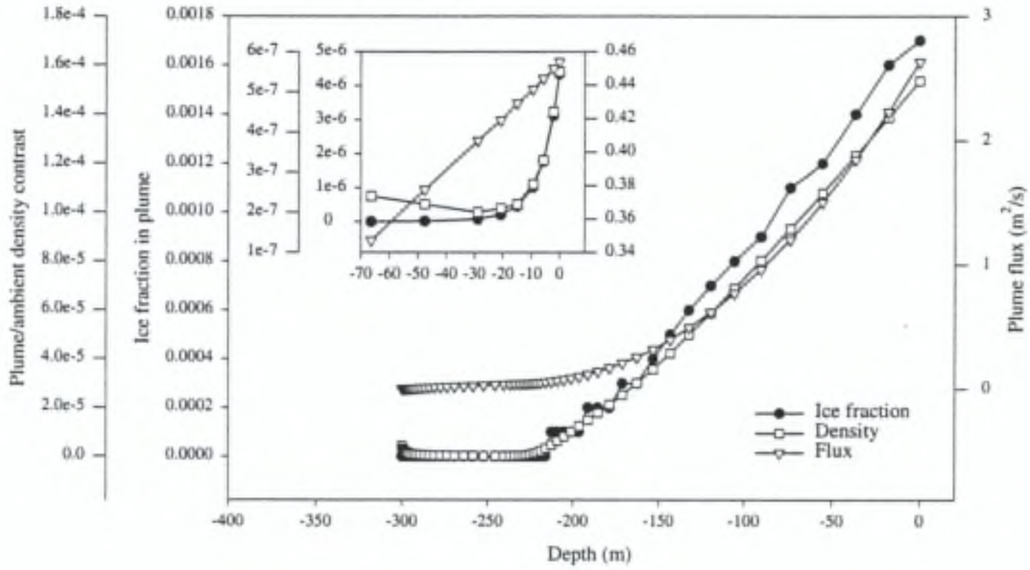

Figure 4.7: The main figure represents the evolution of plume properties in the -2.1°C experiment, while the inset depicts the situation for the -1.95°C experiment, but only for the last 70 meters below the surface since frazil production only picks up at around 30 meters depth, as opposed to 215 meters for the -2.1°C case. The legend and axis titles of the main figure apply to their inset counterparts. Notice how the final plume flux in the -2.1°C experiment is more than 5.7 times that in the -1.95°C case.

Now, the process by which a change in the ambient freezing depth affects ice production is investigated. To achieve this, a more detailed look is taken at the plumes in the case of initial ambient temperatures of -1.9500°C and -2.1000°C, both at a fixed salinity of 34.38. These temperatures are the ones at the beginning and end of the enhanced ice production range in Figure 4.5a, thus maximizing the contrast between the two experiments in order to better discern their differences. The former produces only 0.0057 meters of ice and has an ambient freezing depth of 83.0828 meters, while for the latter these values are, respectively, 12.1856 meters and 280.19185 meters. The examination of Figure 4.7 suggests the following sequence of events: the lower the ambient freezing point in the water column, the earlier the plume enters the zone of freezing, the earlier it starts forming frazil ice in suspension, the higher the concentration of these crystals becomes, the higher the resulting buoyancy of the plume (equation (3.5)), the faster it ascends the face of the rift, the more supercooled ambient water it entrains (equation (3.8)), the larger the plume and its flux (the product of plume velocity and thickness) become and the higher the quantity of ice it deposits once it reaches the top of the water column. A positive feedback cycle between ice concentration in the plume and its velocity is already noted by *Jenkins and Bombosch* [1995], but the details of the process is different. In their ice shelf situation, the authors explain that if ice concentration is growing in the plume the higher the plume velocity and the lower the possibility to deposit crystals which in turn maintains the velocity. Once deposition begins, the opposite process takes place and rapid deceleration occurs. In the rift situation, however, there is no ice deposition before reaching the top of the cavity. Therefore, crystals continue to provide additional buoyancy and velocity to the plume which increases the rate of supercooled water being entrained thus providing the conditions to form even more crystals.

It is interesting to take the temperature (-1.9694°C) and salinity (34.4333) resulting from the plume in the -2.1°C experiment and use them as the initial values for another run of the model.

These values are both higher in comparison with their respective initial values of the experiment, confirming the observation of the previous section that in a situation of important frazil formation the accompanying release of latent heat and salt raises the temperature and salinity. The discussion earlier in this section (Figures 4.5a and 4.5b) demonstrates that higher values for each of these parameters are associated with lower ice production. Therefore, one would expect much reduced ice formation when the input values are -1.9694°C and 34.4333 instead of -2.1000°C and 34.3800. Indeed, this is the case with an output accumulated ice thickness of 0.1411 meters compared to 12.1856 meters in the original -2.1°C experiment.

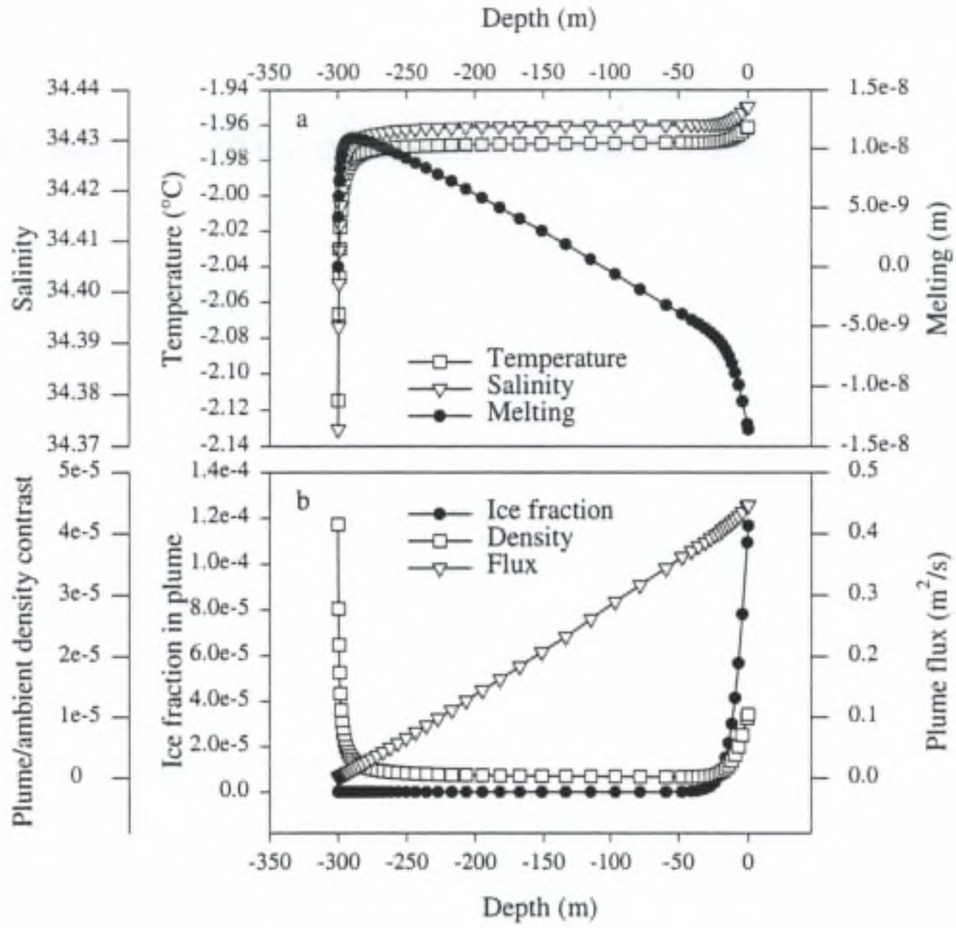

Figure 4.8: Output data for initial temperature and salinity values of -1.9694°C and 34.4333, respectively. (a) Melting values are the thickness of ice added or removed from the rift's wall during the time span considered. Negative values for the melting profile indicate freezing and vice versa (b) This plot depicts the equivalent profiles to those in Figure 6, to which it is also to be compared.

By way of comparison with the -2.1°C case, the sequence of events for the latter experiment is presented in detail in Figures 4.8a and 4.8b. The temperature and salinity profiles of the plume are first provided in Figure 4.8a which helps explain the marked differences in the density and flux profiles between the two experiments. It can be seen how the plume starts at a temperature and salinity that are lower than the ambient values, which is a clear indication of the occurrence of ice melting from the rift's wall. However, since the flux at this point is still small (Figure 4.8b), entrainment of the warmer, saltier and denser ambient water manages very quickly to raise the value of both of these parameters, in addition to lowering the density contrast (Figure 4.8b), until a point is reached where the heat, salinity and density lost through melting are compensated by entrainment thus stabilizing both profiles. Most of the plume's path is in this stabilized phase during which the temperature and salinity still continue to slightly increase and the density contrast to slightly decrease mainly because melting is steadily declining as shown in Figure 4.8a. Melting of the rift's wall stops completely somewhere between the depths of 96.2855 115.0355 meters, a range which includes the ambient freezing point depth of 104.5620 meters. Afterwards, freezing at the wall of the rift begins, but it is not until frazil formation picks up at 47.5259 meters depth that a clear increase in the density contrast begins to be manifest. Ice fraction growth induces an increase in plume flux but neither has the same proportions of the -2.1°C case (Figure 4.7). Due to the position of the ambient freezing point, these changes are taking place too close to the termination point of the plume to make a comparable effect. In fact, before the onset of frazil formation, the profiles of both the -2.1000°C/34.3800 and the -1.9694°C/34.4333 experiments are qualitatively the same. The discrepancy begins once the presence of ice crystals, at different points of the development of the plume in each case, initiates the above-mentioned series of events that gives different outcomes.

4.2.2 Conclusion

The experiments in this section serve to show that it is possible to establish a certain pattern for the plume's interaction with the wall of a rift when examining the quantity of generated ice. This is shown to be determined by the temperature and salinity of the ambient water, and how these two parameters affect the position of the ambient freezing point. The decisive role of this last parameter in modifying the magnitude of ice produced in the first time step is revealed. The linear change in the ambient freezing point is shown to be magnified through the multiple interactions and feedback cycles taking place.

The investigation so far concentrates on the initial stages of the interaction. However, the conclusions about the effect of the variation in temperature or salinity on the quantity of ice formed apply generally. The study of the effect of the entrainment constant below is the occasion to examine the long term evolution of the subject. In the meanwhile, the following section presents the attempt to devise a method to determine whether a certain combination of temperature, salinity and rift configuration lends itself to high ice formation.

4.3 Recognition of high-ice output cavities by an empirical relationship

Looking at Figures 4.5 and 4.6 one can notice how quickly the amount of generated ice changes after reaching a certain ambient freezing depth. This makes it tempting to think of classifying rift and bottom crevasse systems as belonging to one of either two possible regimes: one of initial high-ice output and another of initial low-ice output. The following step would be to try to investigate whether it is possible to find a relatively simple criterion by which the distinction between the two could be made. With fieldwork especially in mind, the question in other words is that if a cavity under study is found to have certain dimensions and vertical location and the water filling it is measured to have certain temperature and salinity, is it feasible using this, relatively accessible, information alone to decide whether this rift system is a high-ice output or a low-ice output one according to the model presented here?

Before attempting to answer, a possible objection should first be addressed. The usefulness of such an undertaking could be questioned on the basis of the discussion in the above section. There, it is shown that even if the plume generates large quantities of ice during the first time step, then this occurrence itself ensures that the following plume acts in a cavity full of water at a higher temperature and salinity, thus sharply reducing ice accumulation. Hence, the difference between the two regimes could only be present during the first time steps and would not have a significant impact on the long term. Such a reservation could be valid until one considers the possibility that water in the rift could undergo renewal through its contact with the main sub-ice shelf cavity. This would result in the removal of ambient water already modified by rift action and replacing it by water with the initial temperature and salinity favorable to enhanced ice generation. If this takes place on regular basis, then the effect on the thickness of ice accumulating at the top of the cavity becomes significant. This idea is tested below in the Ronne Ice Shelf simulation of the next chapter.

4.3.1 Procedure

The search for an empirical relationship proceeds as follows. To render it as general as possible, what is required is a relationship that takes account of the initial vertical extent and width of the rift, the depth at which the rift's bottom edge is located in addition to the initial temperature and salinity of the ambient fluid filling it.

The first step is to chose the criterion or border point that separates high-ice output regimes from low-output ones. To a certain extent, this choice is arbitrary and depends on the specifications of the investigator. In the context of this study, a rift system is designated to be a high-ice output one if the ratio of the thickness of ice produced during the first time step to the initial vertical extent of the cavity is equal to or larger than 1.6667E-5 (throughout, one time step is taken to represent five days). This is equivalent to 5mm of ice accumulation for a 300-meter-deep rift, or 2.5mm for a 150-meter one, and so on.

Keeping this ratio constant for different rift configurations already takes account of the variability of rift widths at the top of the cavity. This is because, for example, a rift that generates a certain thickness of ice would have to produce two times the amount of ice if it were to deposit the same thickness when it has double the width. Therefore, the ambient water in the wider rift would have to have different properties in order to be able to produce double the amount of ice in the same time span. Furthermore, by its definition as a ratio of which the denominator is the rift's vertical extent, this latter parameter is also already considered in the designation of a minimum amount of ice.

Afterwards, different rift configurations are constructed with initial vertical extents varying between 50 and 600 meters, initial widths at the top between 50 and 500 meters and aspect ratios (defined as the ratio of rift's depth to its width at the top) between 1/7 and 7. The salinity is then set to values in the range extending from 33 to 35 and each time the ambient temperature at which the plume begins depositing the minimum thickness of ice designated is found.

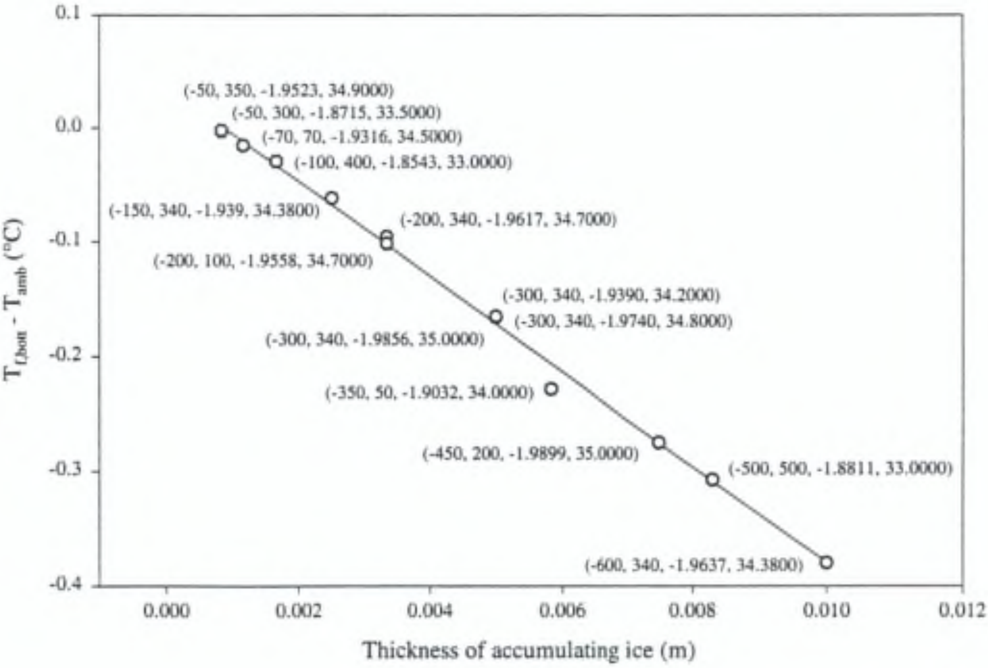

Figure 4.9: The fourteen points representing the experiments and the regression line used to construct the empirical relationship. In the parenthesis besides each point, the numbers represent, in order: the rift's depth, its width, ambient temperature and ambient salinity at which plume begins to deposit the minimum amount of ice. Correlation coefficient of the regression line, $r^2 = 0.9961$.

The resulting data set is then explored in order to find a suitable parameter to plot against the minimum ice thickness. This parameter should take into account the ambient temperature and salinity in addition to the rift's lower edge depth. This last parameter is important to make the relation applicable to bottom crevasses. Using the ambient freezing depth alone is not sufficient since it does not include the depth of the rift's lowest point. An appropriate parameter is found to be the difference between the freezing temperature at the bottom of the rift and the ambient temperature, $T_{f,bott} - T_{amb}$. Thus, the ambient temperature appears explicitly while the freezing point is related to the ambient salinity, S_{amb}, and rift's lower edge depth, z_{rift}, through the relation:

$$T_{f,bott} = aS_{amb} + b + cz_{rift}. \tag{4.2}$$

Figure 4.9 is a plot of $T_{f,bott} - T_{amb}$ against the minimum ice thickness, z_{ice}, and it can be seen that the relationship is very well represented by straight line. Therefore, it is possible to write the equation of this straight line as:

$$T_{f,bott} - T_{amb} = Az_{ice} + B, \tag{4.3}$$

where A = -41.5802°C/m and B = 0.0366°C are the slope and the $T_{f,bott} - T_{amb}$ intercept, respectively.

It is possible to show that the quantity $T_{f,bott} - T_{amb}$ is related to the ambient freezing depth as follows:

$$T_{f,bott} - T_{amb} = c(z_{rift} - z_{amb}).$$

In this equation, the right-hand side becomes larger (less negative) the deeper the ambient freezing point descends, which is associated with higher ice generation as discussed in the above section. Considering the left-hand side, this means that the closer the ambient temperature becomes to the in situ freezing point at the bottom, the higher the ice accumulation becomes. Once the ambient temperature drops below the freezing point at the bottom, however, no initial melting takes place and a plume does not form. Keeping this in mind and considering that the right-hand side in equation (4.3) represents the lower limit above which the rift system is in a high-ice output regime, one can write:

$$0 > T_{f,bott} - T_{amb} \geq Az_{ice} + B.$$

After some rearrangement and using equation (4.2) this becomes:

$$-Az_{ice} - B > aS_{amb} - T_{amb} + cz_{rift} - Az_{ice} + b - B \geq 0\,. \tag{4.4}$$

Therefore, given the ambient temperature and salinity of the water filling a rift of certain dimensions, the inequality can be used to determine whether it is in a high-ice output regime (the middle member of the inequality is equal to or larger than zero), a low one (the middle member is less than zero) or that the water at the bottom is already supercooled hence no plume would start (the middle member is larger than the left member). Testing the inequality reveals that it is accurate to within a few parts in a thousand in the given ranges of salinity, rift depths and rift widths at the top of the cavity, which would be expected in view of value of the correlation coefficient of the regression line in Figure 4.9.

It is also important to point out that the relationship is general enough to apply in an equally satisfactory manner to bottom crevasses whose cavity does not extend all the way to sea level. In this case, care should be taken to interpret z_{rift} as the depth at which the lower edge of the crevasse is found and not the vertical extension of the crevasse, which could be much smaller. These two parameters are the same thing initially in the case of a rift.

4.3.2 Conclusion

An empirical relationship is found that can be used in simulations or fieldwork to predict whether a certain rift or basal crevasse is prone to high ice accumulation.

A high-ice output regime is argued to be important on the long term if it is accompanied with regular ambient water renewal.

The long term evolution of conditions in rifts and crevasses begins to be addressed in the following section.

4.4 Entrainment constant influence and long term evolution of rift processes

The works of *Jenkins* [1991], *Lane-Serff* [1995] and *Jenkins and Bombosch* [1995] all underline the importance of the entrainment process in plume processes. This importance is even more enhanced in the rift/bottom crevasse setting since the plume after the first time step begins entraining fluid that is produced and of which the properties are determined by the action of its predecessors. A feedback cycle is thus created and the importance of this interdependence between the plume's development and its subsequent evolution is already evident in the above discussion and it continues to be so in the attempts to understand the results of experiments below.

The entrainment constant and the choice of its value are discussed above in section 3.2.2. Arguments are presented there to justify retaining the original value of 0.0720 used by *Bo Pederson* [1980] rather than that proposed by *Jenkins* [1991] which has half the original value. In this section, this choice is tested and verified. In the process, different aspects of the long term behavior of the model are exposed.

Four values of the entrainment constant are investigated here. These are the one used by *Bo Pederson* [1980], 0.0720, double that value, 0.1440, the value proposed by *Jenkins* [1991], 0.0360, and half that value, 0.0180. All experiments are run to simulate a 50-year period, unless otherwise specified, with each time step representing 5 days. The Jutulgryta data set is used again, with a water column set initially at -1.8900°C and 34.3800 salinity, the rift taken to be 300 meters wide and 340 meters deep and crystal diameter equal to 2.2mm. This setup is a low-ice output one according to inequality (4.4). However, as is discussed above, even if it were not, the high ice generation of the first few time steps could move it to a low-output regime. The long term evolution of a high-output setting is discussed in the Ronne Ice Shelf rift simulation of the next chapter.

4.4.1 Results

The final output results of the four experiments for the temperature, salinity and total ice accumulation are presented in Table 4.2.

These results show that there is a clear difference and trend in the total amount of ice deposited. However, the differences in the final temperature and salinity are smaller than what one might expect for a range of entrainment constants covering almost one order of magnitude. Furthermore, while there is a trend for increasing temperature with increasing entrainment constant, this trend is interrupted in the case of salinity.

entrainment constant	*ambient temperature (°C)*	*ambient salinity*	*total ice accumulation (m)*
0.0180	-1.9849	34.3407	25.4939
0.0360	-1.9785	34.3414	28.7494
0.0720	-1.9719	34.3415	31.5453
0.1440	-1.9668	34.3404	35.4192
values from observations at Jutulgryta	-1.9750 to -1.9649	34.3350 to 34.3449	approx. 25

Table 4.2: Results for 50-year runs for different values of the entrainment constant. For comparison, observation ranges from the Jutulgryta rift are included in the last row.

In order to have a clearer picture of what is taking place, the behavior of these three parameters is plotted over the whole period of 50 years in Figure 4.10.

One of the main characteristics that emerges from this data set is the tendency for the evolution of all parameters to converge on the long term. This convergence is more pronounced in the case of salinity which explains the even closer final results and the overlapping which accounts for the absence of a trend.

The other important feature displayed by Figures 4.10a, 4.10b and 4.10c is the common distinctive pattern of rapid change for all parameters in the first months of each experiment before entering a phase that comprises most of the simulated time and which is characterized by much slower change.

The task of this section therefore has three main parts: first try to explain the evolution pattern of the parameters under study, which all cases exhibit, on the short and then the long term. Finally, attempt to account for the changes induced by the variation in the entrainment constant among the four experiments and their evolution relative to each other over both time scales.

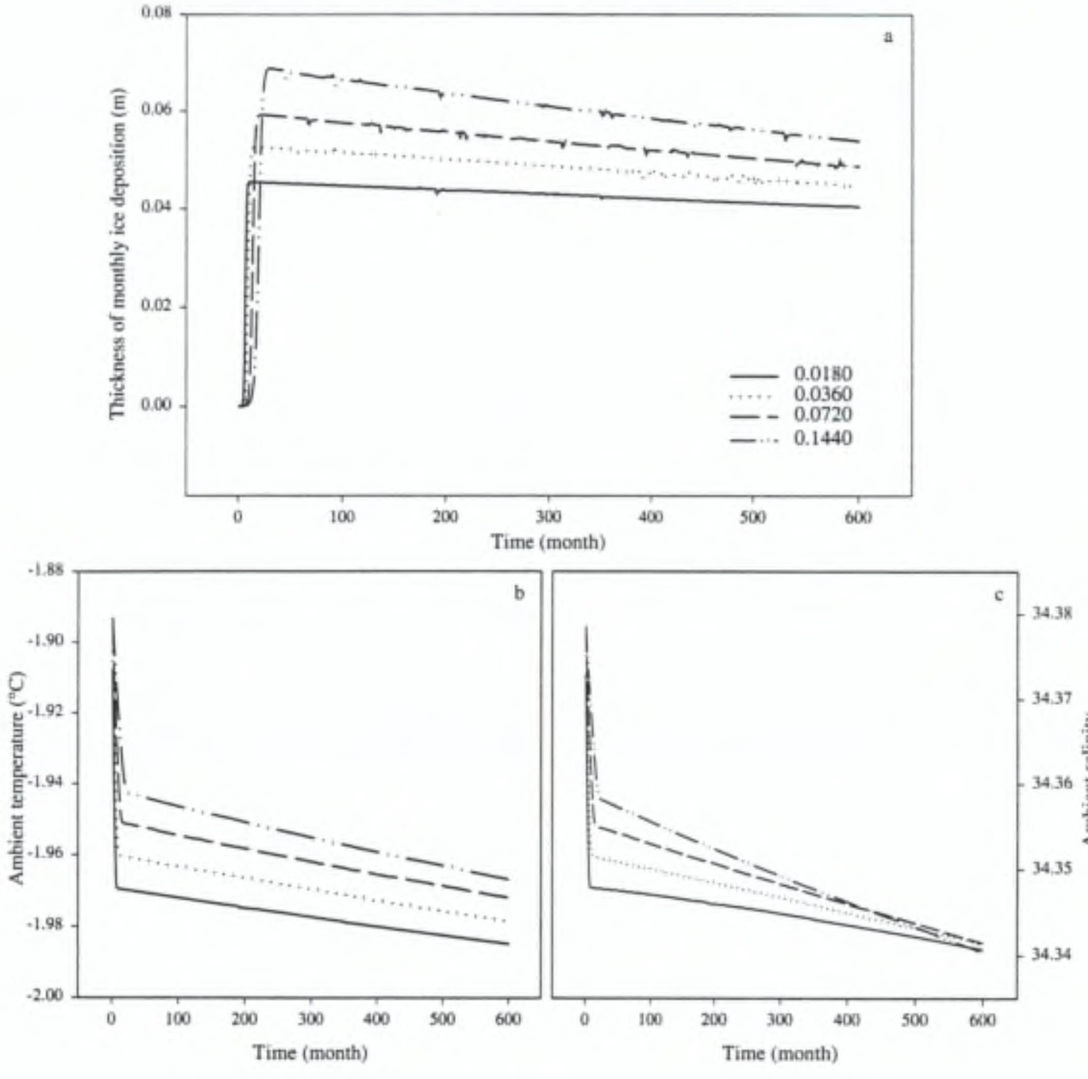

Figure 4.10: The 50-year evolution of (a) quantity of ice deposited by the plume during one month (not the accumulative amount of ice), (b) ambient temperature and (c) ambient salinity for four different values of the entrainment constant. Their values are found in the legend of the first figure, which applies also for the other two plots.

4.4.2 The first months

For all values of the entrainment constant, both temperature and salinity show steep decline in the first few month, while the ice generation per month evolves in an opposite manner as shown in Figure 4.10. After a certain time, all changes slow down greatly and the parameters enter a much longer period of much slower change. The point at which this transition takes place is henceforth designated as the turning point. For each of the entrainment constants used, the turning point for all the parameters occurs at around the same time. While temperature and salinity continue to fall beyond the turning point, monthly ice accumulation reverses its initial increasing trend after its turning point and commences a slow decline. To understand these features, the situation should be analyzed in terms of the competing effects of melting and freezing processes induced by the plume during its interaction with the face of the rift and the ambient water.

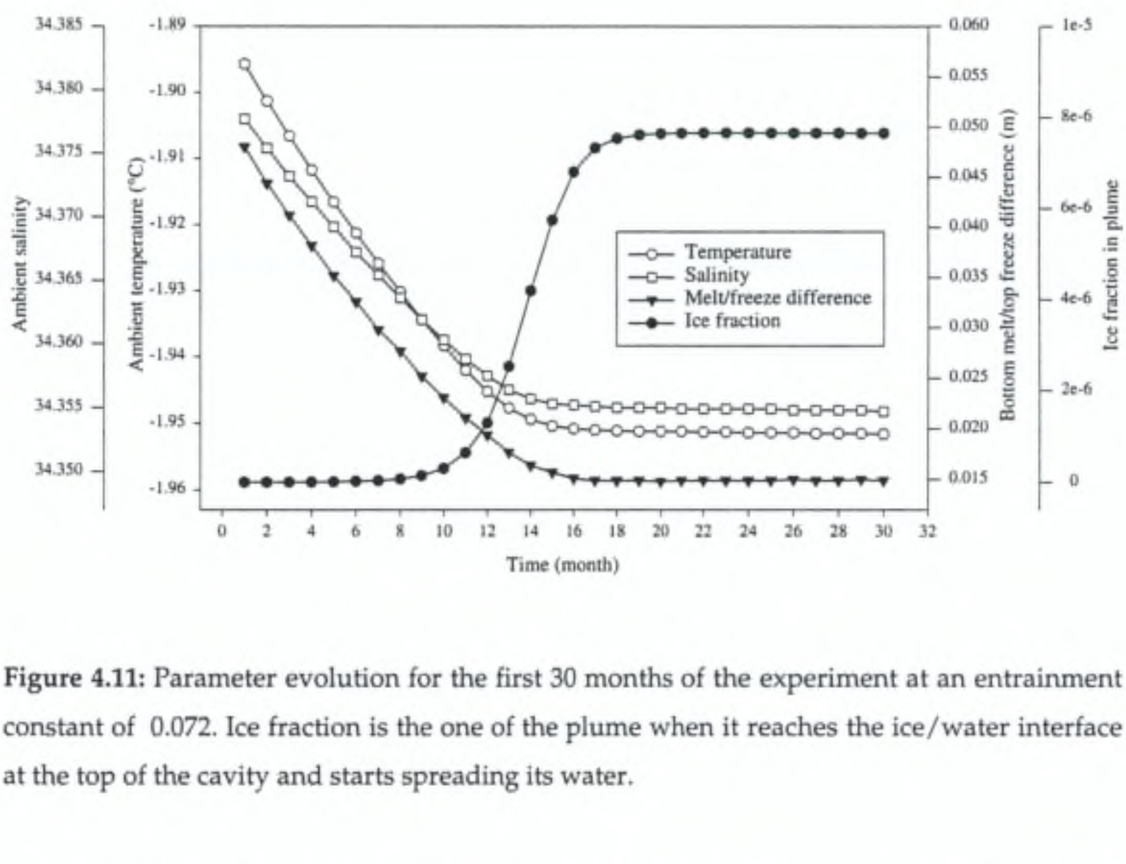

Figure 4.11: Parameter evolution for the first 30 months of the experiment at an entrainment constant of 0.072. Ice fraction is the one of the plume when it reaches the ice/water interface at the top of the cavity and starts spreading its water.

Figure 4.11 represents a closer look at the first thirty months of the 0.072 experiment. The evolution in ambient temperature and salinity is presented along with the two main factors that are needed to understand this evolution. The first is the concentration (by volume) of frazil ice in the plume at the moment when it is stopped by the ice ceiling at the top of the cavity and starts spreading its water to fill it. As a measure of ice production, the monthly ice accumulation could have been used as in Figure 4.10. However, now that the situation is being considered on the long term, a new factor begins to exert its influence.

In addition to frazil generation, the supercooling in the plume is also released, to a lesser extent, through direct freezing on the rift's wall. With time, the width of the rift changes as a result and even if a plume is carrying the same fraction of ice as a previous one, the deposition of ice might result in a different accumulation thickness as can be predicted from equations (3.26) and (3.27) of the previous chapter. Therefore, studying the evolution of ice production through the ice concentration in the plume is relatively more accurate.

However, direct freezing at the wall is taken into account in the other new parameter introduced which represents the difference between its extent and that of melting taking place at the lower part of the same wall. This parameter is devised because there is no exact one number that could be used to give an exact description of the magnitude of melting and/or freezing occurring directly at the side of the cavity. Melting is most intense at a point a little higher than the lowest part of the wall and decreases towards the point of transition after which freezing starts to build up until reaching its maximum at the highest point of the plume's path. One could therefore consider that the amount of ablated ice at the bottom-most point gives a good idea of the general measure of melting of the lower part of the wall while analogously the amount of added ice at the highest-most point does the same for freezing at the upper section. Both melting and freezing are calculated in the model as the thickness of ice disappearing in the case of the former and the thickness of ice added to the wall in the case of the latter. The new parameter is the difference between the two, with the thickness of the ice freezing at the upper-most point in the cavity subtracted from the thickness of the ice melted at the lower-most point for the given period of time. Therefore, monitoring the evolution of ice concentration in the plume and the change in the melting/freezing difference ensures that all the melting and freezing processes in the cavity are taken into account.

In Figure 4.11, the initial simultaneous drop in temperature and salinity is an indication of the predominance of melting. This is confirmed by the positive values always assumed by melting/freezing difference (indicating more melting at the wall than freezing) and the ice fraction in the plume which is very near to zero. Melting, however, is creating the conditions for enhanced ice generation through its effect in lowering both the temperature and salinity. Lower values of these two parameters also lead to the reduction in the extent of wall melting relative to freezing seen in Figure 4.11. The same figure shows that crystal formation begins to noticeably appear around month 8, then rapidly picks up in the following eight months. The mechanism behind this fast increase in ice generation is discussed in the preceding two sections. In the same 8-month period of ice-fraction rapid increase, the decline in both temperature and salinity quickly decreases due to the enhanced emission of heat and salt from the produced ice thus helping to counter the effects of melting. However, high ice generation quickly falls victim of its own success. The resulting slow down of temperature and salinity decline also means limiting the change towards even more favorable ambient conditions for ice formation. Therefore, ice formation itself begins to slow down until reaching the turning point around month 18 and the interplay cycle between ambient conditions and crystal output is closed. It is interesting to notice in Figure 4.11 how at the beginning of this cycle ice concentration undertakes its rise around month 8 but that the response of ambient temperature and salinity starts appearing only later around month 12. Towards the end of the cycle, on the other hand, both temperature and salinity are already at their turning points around month 16 while ice fraction in the plume needs two months to react and reach the same point.

4.4.3 Beyond the turning point into the long term

Figure 4.10 shows that the rate of change of all parameters after the turning point compared to before is noticeably reduced. Both temperature and salinity continue to decline slowly while monthly ice accumulation stops growing and begins also to fall. To be certain that these trends do actually continue on a longer time scale, the 0.0180 and 0.0720 cases are simulated in each case for a period of 250 years. The results are shown in Figure 4.12 with the ice fraction in the plume presented instead of the monthly ice accumulation. These plots indeed demonstrate the continuing general declining trend of all the parameters considered. The root of this behavior resides in the predominance of melting over direct freezing on the cavity wall while the influence of frazil formation is also receding with time. This is the situation in both the 0.0180 and 0.0720 cases as can be seen from Figure 4.12a. The prevalence of melting leads to emphasizing the impact of its associated effects, namely the simultaneous cooling and freshening of ambient water as testified by Figures 4.12b and 4.12c.

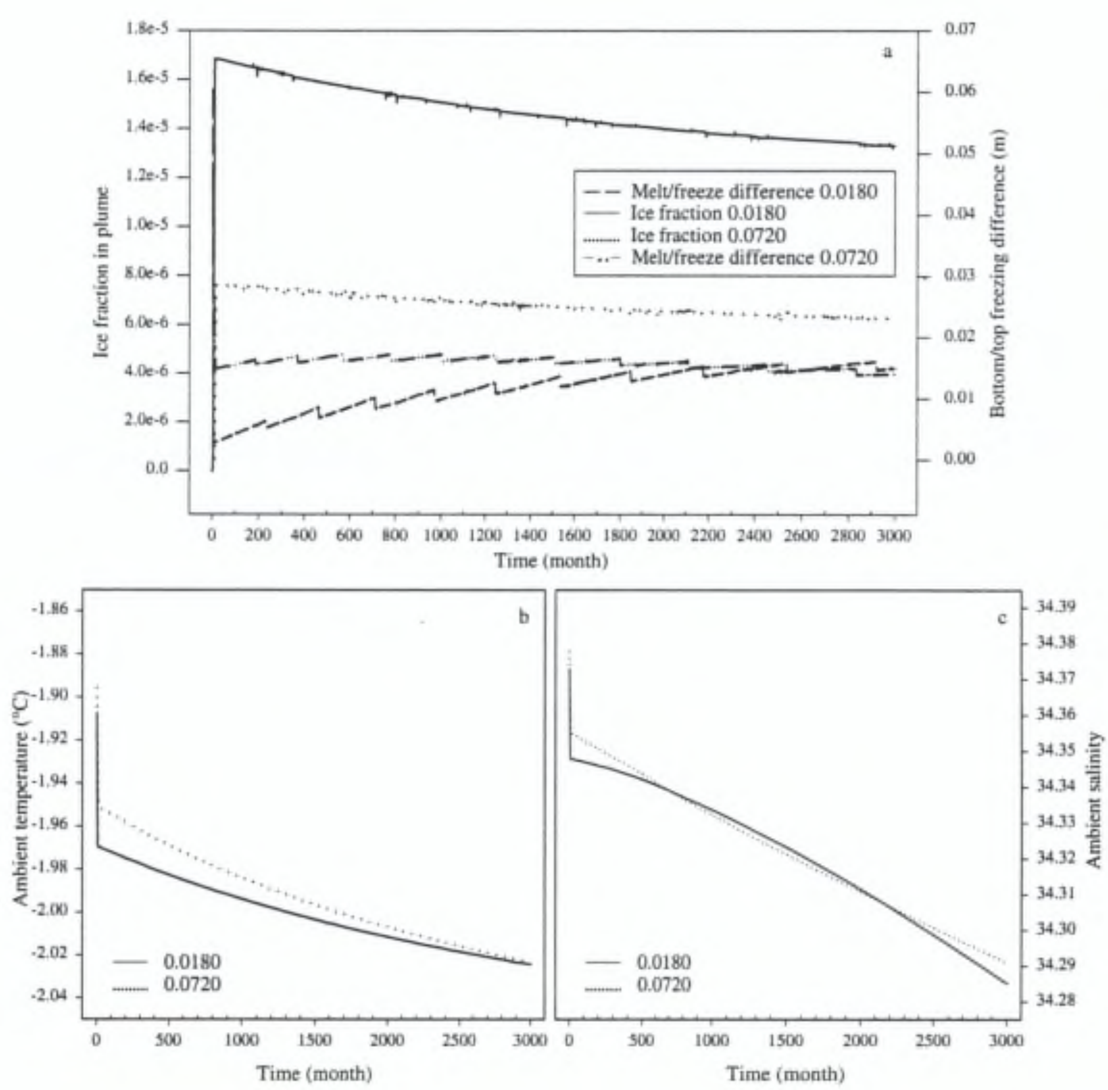

Figure 4.12: The 250-year evolution of (a) the fraction of ice in the plume at the point where it terminates in addition to wall melting relative to direct freezing (b) ambient temperature and (c) ambient salinity for two out of the four different values of the entrainment constant considered in Figure 4.10.

However, from the conclusions of the two preceding sections one would expect ice concentration in the plume to increase with decreasing temperature and salinity. This is clearly not the case as can be seen from Figure 4.12a. The reason has to do with another factor that begins to become important on longer time scales, in this case, the progressive reduction of the vertical extent of the cavity as a result of crystal deposition on top. Consequently, the length of the freezing zone of the plume's path is shortened and the plume has less opportunity to become even more supercooled before terminating, thus having less favorable conditions for crystal generation in suspension. Such behavior is already exposed in the above experiments on ambient water stratification. Shorter path also means less opportunity to entrain ambient water which would make the plume's flux, and subsequently its deposition, smaller at the top.

To test this explanation, the program is therefore modified in such a way as to prevent the generated ice crystals from accumulating on the top of the water column. Hence, throughout the simulation, the initial vertical extent of the cavity does not change. All other parameters do continue to be updated exactly as before, including frazil concentration in the plume, the temperature and salinity of ambient water and the profile of the cavity. The experiment is performed using an entrainment constant of 0.0720 since this is the value used in the preceding sections when studying the relationship between ice production and ambient conditions. The results are plotted in Figure 4.13 and they do indeed show that ice concentration in the plume not only stops declining but actually displays a modest rise with time. Temperature and salinity also evolve differently from the standard experiment with the former remaining very stable around the turning point value while the latter falls slightly.

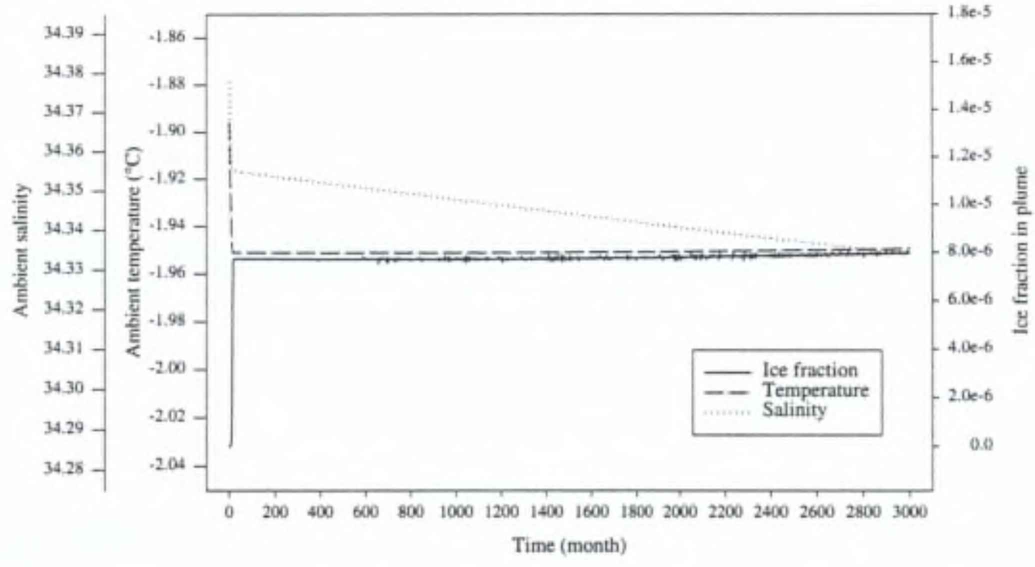

Figure 4.13: The 250-year evolution of plume ice concentration, ambient temperature and salinity for the case of an entrainment constant of 0.0720 but with frazil crystals not permitted to accumulate at the top of the cavity. The scales are the same as the ones used in Figures 4.12a, b and c to facilitate comparison.

The drop in salinity is certainly due to prevalent melting which in turn is a consequence of the maintenance of a higher temperature relative to the standard experiment (Figure 4.12b). The ambient freezing depth therefore hardly moves and stays relatively high in the cavity throughout the run. At the turning point (month 18), it is calculated from equation (4.1) to be at a depth of 86.2717 meters to reach its deepest point around 87.0664 meters depth at month 1700 (which coincides with the slight increase in plume crystal concentration at that point) and goes back up to a depth of 85.7580 meters at the end of the experiment. This agrees well with the final profile of the cavity which shows that, starting from the bottom, the last point at which there is melting at the cavity's wall is at depth 90 meters and the first one at which freezing begins is at depth 80 meters. By comparison, the melting/freezing transition in the final output of the standard experiment occurs lower in the water column between 150 and 140 meters depth. However, salinity in the experiment with no ice accumulation at the top does not descend as low as the standard run (Figures 12c and 13) because of the maintenance of crystal concentration levels in the plume and the continued availability of the higher portion of the cavity for direct freezing on the wall, both contributing to counter the effects of melting.

The question arises however of why the temperature remains rather stable (with a small increase towards the end) and does not exhibit the same general decreasing tendency as the salinity, especially that both are affected by the same processes of phase change in the system. A prerequisite to the answer is to emphasize the fact that changing ambient properties are in turn responsible for modifying some of the underlying conditions of the process. Thus, the progressive drop in salinity results in the continuous rise in the in situ freezing point in the cavity. Figures 4.14a and 4.14b depict this outcome for the standard 0.0720 experiment and the one with no ice accumulation, respectively. It can be seen that in the standard experiment the increase in the in situ freezing point is more prominent since the decrease in salinity is steeper. This discrepancy is the result, in the standard experiment, of the enhanced relative dominance of melting over freezing for the reasons given above. However, the contrast in the scope of melting and freezing processes is behind the even more divergent evolution of the other parameter plotted in Figures 4.14a and 4.14b. The difference between the ambient temperature and the in situ freezing temperature (at the bottom of the cavity) in the standard experiment exhibits distinct decline with time while, in the no-top-accumulation run, it barely moves. Therefore, keeping in mind that phase changes moves ambient water closer to its freezing point, one can discern the following. In the standard experiment, more enhanced melting relative to freezing pushes salinity down which increases the in situ freezing point but its effect on cooling plume water is proportionately more pronounced so the end result is a net decline in ambient temperature (Figure 4.12b). In the no-top-accumulation situation, on the other hand, the in situ freezing point is also rising with time, but less enhanced melting relative to freezing means that the extent to which plume water is cooled is nearly equal to the rise in the in situ freezing point. The two effects more or less cancel each other which gives the stable temperature profile of Figure 4.13. It is as if the ambient temperature is being "carried along" on top of an increasing "base" freezing temperature.

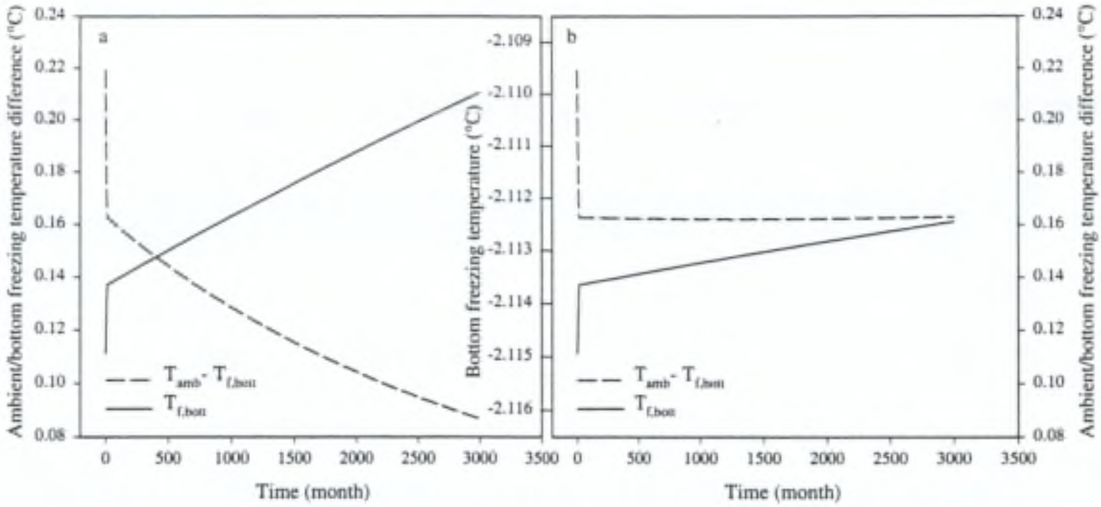

Figure 4.14: The 250-year evolution of the in situ freezing point at the bottom of the rift (at 300 meters below sea level) and the difference between it and the ambient temperature in the cavity (freezing point subtracted from ambient temperature) for (a) the standard experiment with the entrainment constant set to 0.0720 and (b) the modified experiment where ice crystals do not accumulate at the top of the water column. The scale in the middle applies for both plots.

4.4.4 Effects of entrainment constant variation

Although the parameters under study show the same general pattern of behavior for all the tested entrainment constant values, there are important quantitative differences that need to be explained.

Figure 4.10 shows that the higher the entrainment constant the lower the ambient temperature, salinity and deposited ice thickness at the turning point and the earlier this point is reached. On a large time scale however, Table 4.2 and Figures 4.12b and 4.12c show that convergence occurs for ambient temperature and salinity while important differences persist in the final total thickness of ice accumulated on the top of the cavity. The determining factor in producing these differences is obviously the amount of ambient water that the plume integrates. This amount is directly proportional to the entrainment constant according to equation (3.8) of the last chapter. Therefore, in the beginning, for higher values of the entrainment constant, the plume entrains larger quantities of the ambient fluid. Consequently, plume water is relatively less affected by the addition of the cold and fresh melt water. Thus, the drop in the resulting temperature and salinity takes longer and never reaches as low as when the entrainment constant is smaller. In the latter case, the fact that temperature and salinity drop so low requires that the plume produces more frazil (Figure 4.12a) before it is able to balance the effects of melting and slow down the parameter rate of change. However, the actual amount of crystals accreted also depends on the flux of the plume (the product of its thickness and velocity in two dimensions). Higher plume volume means that at termination the flux of the plume is much higher for the high-entrainment constant cases. Therefore, even if the concentration of ice crystals in such cases is less than those for low-entrainment constant plumes (Figure 4.12a), the accumulated ice quantity is larger because the plume is larger. For example, the thickness of the terminating plume in the 0.0180 case at its turning point at month 11 is 4.4819 meters and the ice concentration is 16.8600E-6. The corresponding turning point values for the 0.0720 case at month 18 is 19.1827 meters and 7.5370E-6, respectively. The plume velocity discrepancy between the two cases is not as decisive with the 0.0180 case velocity at 0.0354m/s versus 0.0235m/s for the 0.0720 case. Situations with higher entrainment constants generally have lower plume velocities because the fact that they are mixing larger quantities of the ambient fluid means that the density difference between the plume and the ambient is reduced. This renders the buoyancy of the plume lower, thus reducing its velocity.

For both entrainment constant values tested in Figure 4.12, the prominent feature after the turning point is the dominance of melting at the wall, associated with the decline in frazil crystal generation discussed above. Hence, both cases show a decrease in temperature and salinity but at different rates. In the 0.0720 case, Figure 4.12 shows that the frazil concentration is lower in the plume and that the relative extent of melting relative to freezing is higher than the other case, because of the higher ambient temperature and salinity at the turning point. Melting does decrease afterwards with dropping temperature and salinity but so does freezing because of crystal accumulation at the top, and the two trends manage to approximately balance each other. The result is that these two parameters, but especially ambient salinity, decline faster than in the 0.0180 experiment. This makes the salinity of the high entrainment case catch up with that of the low entrainment case around month 700 (Figure 4.12c). The two remain close for a while during which salinity of the 0.0180 case begins to drop faster again. The reason can be seen in Figure 4.12a where the melting/freezing difference for this case is increasing with time. This is mainly due to the reduction in direct freezing as more and more frazil accumulates in the top part of the cavity. Table 2 shows that after 50 years, the proportion of the initial vertical extent of the cavity (300 meters) covered by ice in the 0.0810 case is 0.0850 while it is 0.1052 in the 0.0720 case. However, at the end of the 250 these proportions are closer at 0.3396 and 0.3801, respectively. The plume 0.0180 case succeeds in reducing the gap on the longer run due to its higher crystal concentration and the fact that the plume thickness advantage of the 0.0720 case is also reduced with shrinking cavity vertical extent.

4.4.5 Conclusion

Work in this section shows that the change in the ambient entrainment constant has a significant effect on the total amount of ice accreted at the top of the cavity. Temperature and salinity, the other two parameters examined, however, show a tendency to converge for different entrainment constants. This is mainly due to the discrepancy of evolution during the first few months which results in each system entering the long remaining phase after the turning point with different ice production capacities of the plume and different ambient conditions. Another factor is the influence of the change in the vertical extent of the cavity and its evolution with time. The effect of rift or crevasse dimensions are more systematically investigated in the following section.

4.5 Effect of cavity dimensions

The examples of observed rifts and crevasses presented in the simulations of the next chapter testify to the variety of sizes that rifts and crevasses exhibit. In this section, the effects of changing each of the two dimensions of the cavity on the output ambient temperature, salinity and ice accumulation are investigated. The Jutulgryta data set is used with the entrainment constant set to 0.0720. All other experiment specifications are the same as those used in the above study of the entrainment constant variation and 50-year runs are simulated.

The main consequence of changing the width of the cavity is to modify the thickness of accumulated ice and water layers according to equations (3.26) and (3.27). In studying the vertical extent of the cavity, on the other hand, two effects that could simultaneously result from its change should be distinguished. First, the shift in the location of the cavity as a whole in the vertical direction. This affects the relative location of the ambient freezing depth and that of the lower-most point of the cavity wall and thus the temperature difference between the local freezing point and the ambient water. Second, the change in the distance along which the plume reacts with the ice wall and entrains ambient fluid. Hence, rather than, for example, just testing rifts that have different vertical extents measured from the surface, experiments are designed to identify the role of each factor separately.

4.5.1 Fixed starting depth with different wall lengths

In this series of experiments, first a rift that opens along the whole thickness of an ice shelf with an initial vertical extent of 600 meters is tested. Then, this is halved and a test is run with a 300-meter rift that still has its most-lower point at a depth of 600 meters. This would be equivalent to a basal crevasse that opened at the bottom of the same ice shelf but only managed to reach half way up the thickness of the shelf. In a third experiment, the vertical extent is halved again to 150 meters. The results are presented in Table 4.3.

Rather expectedly, especially after the discussion of the stratification section above, these results show that the larger the vertical extent of the cavity, the larger the amount of ice generated and accumulated at the top and, consequently, the warmer and more saline the resulting ambient fluid. It is interesting to notice that, to a good approximation, each time the vertical extent is doubled, the amount of accumulating ice quadruples.

vertical extent (m)	*ambient temperature (°C)*	*ambient salinity*	*total ice accumulation (m)*
600	-2.0665	34.3023	138.9892
300	-2.1937	34.2448	30.1771
150	-2.2761	34.2122	7.2336

Table 4.3: Results for 50-year runs for different values for the rift's vertical extent. Parameter values are those existing in the cavity at the end of the experiments.

vertical extent (m)	*flux (m^2/s)*	*supercooled ambient thickness (m)*	*supercooling at top of cavity (°C)*
600	0.9084	103.0321	0.0784
300	0.3797	83.3222	0.0634
150	0.1381	66.9989	0.0510

Table 4.4: Factors that explain the results shown in Table 4.3. All values are taken at the last time step of the 50-year run in all experiments. The flux is taken at the point where the plume reaches the top of the cavity and starts spreading its water. The supercooled ambient thickness is the vertical distance between the ambient freezing depth and the top of the cavity in each case.

The factors that could explain these observations are organized in Table 4.4. Cavities that are closer to the surface obviously provide a better setting for their ambient fluids of having a larger degree of supercooling in the part of the water that lies above the ambient freezing depth. The upper section of the cavity containing supercooled ambient fluid tends also to be longer the bigger the vertical extent. Both these trends are clear from the data of Table 4.4. This data also show that, the longer the path of the plume is the more opportunity it has to entrain ambient water and the larger its flux at the top becomes. All these factors acting together combine their effects to produce the trend of increased ice generation, and the associated effects on ambient properties, with longer ice walls.

4.5.2 Fixed wall lengths with varying vertical location

In this series of experiments, the initial vertical extent of the cavity is kept constant but the location at which the cavity is located below sea level is made to vary. Three different configurations are used and the results are presented in Table 4.5.

vertical location of cavity (m)	*ambient temperature (°C)*	*ambient salinity*	*total ice accumulation (m)*
0-300	-1.9719	34.3415	31.5453
300-600	-2.1937	34.2448	30.1771
600-900	-2.4160	34.1508	29.2303

Table 4.5: Results for 50-year runs for different rift locations in the vertical direction. The numbers in the first column indicate the depths, below sea level, between which the initial cavity was extending at the beginning of the run. Parameter values are those existing in the cavity at the end of the experiments.

vertical location of cavity (m)	*flux (m^2/s)*	*supercooled ambient thickness (m)*	*supercooling at top of cavity (°C)*
0-300	0.3762	83.2147	0.0633
300-600	0.3797	83.3222	0.0634
600-900	0.3830	83.4627	0.0635

Table 4.6: Other parameters related to the results shown in Table 4.5. All values are taken at the last time step of the 50-year run in all experiments. The flux is taken at the point where the plume reaches the top of the cavity and starts spreading its water. The supercooled ambient thickness is the vertical distance between the ambient freezing depth and the top of the cavity in each case.

It is interesting to note that despite the decreasing trends in ambient temperature and salinity with increased depth of cavity location, the differences in the thickness of accumulated ice are relatively small. This closeness becomes more evident when the parameters used to explain the results for different wall lengths above are presented for the current case in Table 4.6.

Part of the explanation is the general fact that all three situations have identical initial vertical extents and ambient properties. Then, there are the details of the interaction among the plume, the ice and the ambient water.

According to equation (3.3), the flux of the plume depends on the quantity of fluid it acquires or looses. Equation (3.8) shows that the entrainment rate is not a function of pressure. As for the melting rate, an expression for this parameter can be obtained by solving simultaneously equations (3.10), (3.11) and (3.1), using in the process the expression for the temperature gradient in the ice which is estimated in section 3.2.2. The result is a quadratic equation in the melting rate of which one solution is valid. That solution reveals that the melting rate is not explicitly a function of pressure and that, furthermore, it is a function of the "difference" between the temperature of the plume and the local freezing point. The analysis of *Lane-Serff* [1995] shows that the water in the plume tends toward the local equilibrium values of temperature and salinity. Deviation in either direction is corrected by melting or freezing. *Lane-Serff* [1995] explains that these equilibrium values are depth-dependent. Therefore, in the current work, pushing the cavity down shifts equilibrium levels accordingly. Under the new pressure conditions, plume temperature and salinity will continue to fluctuate around their new local equilibrium values in the same manner. Hence, the difference between plume water temperature and the local freezing point would be expected to remain rather stable, producing the close results observed for ice accumulation, flux and supercooling levels.

However, the values of ambient temperature, salinity and ice accumulation are not the same and they do show consistent trends. At the origin is the fact that, initially, only in the cavity between sea level and 300 meters depth is ice generation possible. In the other two cases, the ambient freezing depth is above the top end of the cavity which consequently lies entirely in the melting zone. In the first case, therefore, ice accumulation begins earlier which accounts for its higher final value. In the other two cases, increased pressure means that the equilibrium freezing point is lower and thus melting is much more active initially. This pushes temperature and salinity down, more so the deeper the cavity as can be seen from Table 4.5. Additional support for this idea comes from examining the thickness of ice ablated at the lowest point of the wall of the cavity, an amount which increases with increased melting. In the case of the cavity located between 0 and 300 meters depth, 17.4754 meters of ice were melted, in the 300 to 600 meters case, this figure stands at 18.9379 meters, while in the 600 to 900 meters case, 20.9413 meters of ice were missing at the end of the 50-year run.

4.5.3 Variation of initial cavity width

With a time step set to 5 days, plume flux at the point where it spreads is usually sufficient to fill the whole cavity beneath it. Under such conditions, changing the initial cavity width would only change the thickness of accumulated ice by an amount that is inversely proportional to the width change. Ambient temperature and salinity would stay the same. In this series of experiments, the time step is reset to 1 day in order to allow for plume water to be inserted at the top of the cavity without completely filling it. Thus, an ambient fluid structure stratified in temperature and salinity develops with time as each successive plume spreads its water. Three different cavity widths are used in experiments that simulate 10 years each, since the higher time resolution made it difficult to go up to the usual 50 years. The program was instructed not to allow more than six ambient layers to accumulate. If this limit is exceeded, then the lower-most two layers in the water column are mixed appropriately. The results are compiled in Table 4.7.

initial cavity width (m)	*ambient temperature (°C)*	*ambient salinity*	*total ice accumulation (m)*
170	-1.9611	34.3463	15.2683
340	-1.9555	34.3495	6.8651
680	-1.9531	34.3525	3.1745

Table 4.7: Results for 10-year runs for different initial rift widths. The time step is set to 1 day.

In the 170-meter experiment, as a result of the relative narrowness of the rift, the plume was still capable of filling the cavity totally. In the other two cases, on the other hand, the smaller time step ensured that stratification of the ambient fluid did occur with time. More so in the case of the 680-meter case, due to the larger rift.

The discussion of the entrainment section shows that the general long term trend is for the ambient water to become colder and fresher. In the current experiments, this means that, in the 340-meter and 680-meter cases, the plume will be entraining warmer and saltier water for longer, since more time is needed to completely replace the initial ambient fluid. These differences are reflected in the trends manifested by the output data of Table 4.7. The larger the rift, the warmer and more saline its final output ambient water is. In addition, doubling the initial rift width results in the total ice output being reduced by more than half instead of just being halved as would be expected in the case of no stratification. This is again the result of the more prolonged entrainment of warmer and saltier ambient water. The enhanced reduction of ice generation can be understood in the light of the results of the preceding sections, where the inverse correlation between ice output and the ambient temperature and salinity is revealed.

4.5.4 Conclusion

The experiments of this section highlight the importance of the vertical extent of the cavity under study relative to the other aspects of the configuration of the cavity.

4.6 Crystal size specification

Jenkins and Bombosch [1995] describe how, in reality, the plume at any given time would be containing crystals of different sizes. They underline the need to make the simplification, albeit major, of assuming that all crystal have the same spatial dimensions, in order to render possible the modeling of the problem. Consequently, the authors thoroughly test their plume model with different crystal sizes.

4.6.1 Results and discussion

In this work, the laboratory analysis results presented in chapter 2 are used to help select an appropriate crystal size for use in the rift model. Figure 2.7 shows that most of the NIS core crystals have radii that are in the range from 0.60mm to 1.10mm with an average value around 0.86mm. These three values are tested and the results are organized in Table 4.8. The Jutulgryta data set is used with the entrainment constant set to 0.0720. All other experiment specifications are the same as those used in the above study of the entrainment constant variation and 50-year runs are simulated.

crystal radius (mm)	*ambient temperature (°C)*	*ambient salinity*	*total ice accumulation (m)*
0.60	-1.9523	34.3319	42.5991
0.85	-1.9625	34.3413	36.9060
1.10	-1.9719	34.3415	31.5453
values from observations at Jutulgryta	-1.9750 to -1.9649	34.3350 to 34.3449	approx. 25

Table 4.8: Results for 50-year runs of different choices for the crystal radius. Parameter values are those existing in the cavity at the end of the experiments.

The results show a noticeable increase of total ice output with decreased crystal size. Smaller radius, for the same given concentration, increases crystal edge area at which heat and salt exchanges take place, as noted by *Jenkins and Bombosch* [1995]. Salinity, on the other hand, shows the opposite behavior. Although increased ice accumulation should be associated with increased salinity, this accumulation is also blocking the upper portion of the cavity where direct freezing takes place. This removes an additional source of salinity and its effect on the final output level of this parameter, associated with enhanced melting at lower portion due to higher temperatures, outweighs that of higher frazil generation. The reduction in temperature with increased crystal radius reflects the adjustment of the system to the lowering of the freezing point due to higher salinity.

4.6.2 Conclusion

Comparing the results of the different crystal radii tested with the observations at Jutulgryta suggests that a radius of 1.1mm gives an experimental result that agrees most with the field study. This crystal size is therefore adopted in the simulations of the next chapter and, with hindsight, in the above sensitivity studies, keeping in mind that the aspect ratio of the crystals is always kept constant.

Chapter 5

Rift processes: Support in the literature and applications

The first main objective of this chapter is to make an attempt to apply the model in such a way as to provide reasonable representation of natural conditions in open rifts and basal crevasses. Instead of relying solely on constructing hypothetical idealized settings, effort is made to examine the available literature in order to find field observations that could serve as input for the model. This would involve records of the temperature and salinity profiles in rifts or bottom crevasses of known dimensions. Rifts open in ice shelves are on occasions used to provide easier access for sampling water from under the shelf, consequently, the literature contains some accounts, although few, that could be useful in the current context. In the case of bottom crevasses, however, their relative inaccessibility means that only an approximate idea of their possible dimensions, measured by radio echo sounding methods, is available while the input temperatures and salinities involved should be inferred from the available data of sub-ice shelf conditions or measurements taken at the front of the ice shelves concerned.

In the previous chapter, model dependence on several parameters is studied. From this first group of tests, a combination of parameters is chosen to be used during the second main set of simulations presented in this chapter. Therefore, in all of the following experiments, a non-stratified water column, an entrainment constant set to 0.072 and a crystal radius of 1.1mm are used. These choices are suggested by the comparisons, in Tables 4.1, 4.2 and 4.8, among experiment output ambient temperature and salinity and the Jutulgryta data set. The time step is 5 days throughout.

Figure 5.1: A schematic map of Antarctica showing the locations, indicated by crosses, of the rifts and bottom crevasses being discussed in this chapter.

The other main objective of this chapter is to present field study observations which serve to support the principal thesis of this work. This is achieved by considering rifts or bottom crevasses which exhibit indications of an ice pump process active inside their cavities. Such evidence includes direct or indirect observations of ice formation, the relation of the extent of this formation to the properties of the adjacent ocean and modified cavity dimensions and shapes. In fact, the following review shows that many investigators were already aware of the possibility of "local ice pumps" taking place inside rifts and bottom crevasses, even if they did not all hypothesize on the details of the process.

Figure 5.1 provides a map that shows the approximate locations of the features being studied in this chapter.

5.1 Rift at Jutulgryta near the grounding line

The work of *Orheim et al.* [1990] and that of *Osterhus and Orheim* [1992] provide an observed data set which is so far relatively the most detailed available in the literature for the purposes of this study.

5.1.1 Setting and observations

Working on the Fimbulisen Ice Shelf (Dronning Maud Land, East Antarctica), *Orheim et al.* [1990] discovered a rift located in the fracture zone of Jutulgryta, 71°18.6'S, 00°17.2'E. They measured the temperature and salinity from the top of the water column down to the sea floor and recorded the depth and width of the rift. This information is presented in Figure 5.2. *Osterhus and Orheim* [1992] returned 23 months later to collect instruments that had been left in place for further measurements which allowed them to observe the changes in ice thickness and conditions that occurred in the mean time.

The first point of interest to the current work is that this rift is located near the grounding line of the ice shelf as can be seen from the map in Figure 5.1, which is the only such example that could be found in the literature.

Then, there is the fact that temperature and salinity were measured from the top of the water column down to the sea floor, thus revealing differences between the conditions of the water inside the rift, its lower edge being situated around 300 meters below the surface, and the properties of the ocean beneath. These differences, apart from the properties of the top 40 to 50 meters affected by melting, cannot be explained by "natural" stratification.

Figure 5.2 shows rather stable profiles inside the rift with salinity values slightly fluctuating around 34.34 and in situ temperatures around -1.97°C. Once outside the rift, these values increase noticeably toward the sea bed to 34.38 for salinity and to -1.89°C for temperature. At this temperature, the water at the sea bed is at its surface freezing point, calculated from equation (3.1) to be -1.8868°C. However, its salinity is lower than what authors usually consider to be characteristic of High Salinity Shelf Water (HSSW), which is higher than about 34.70 [e.g. *Jacobs et al.*, 1985].

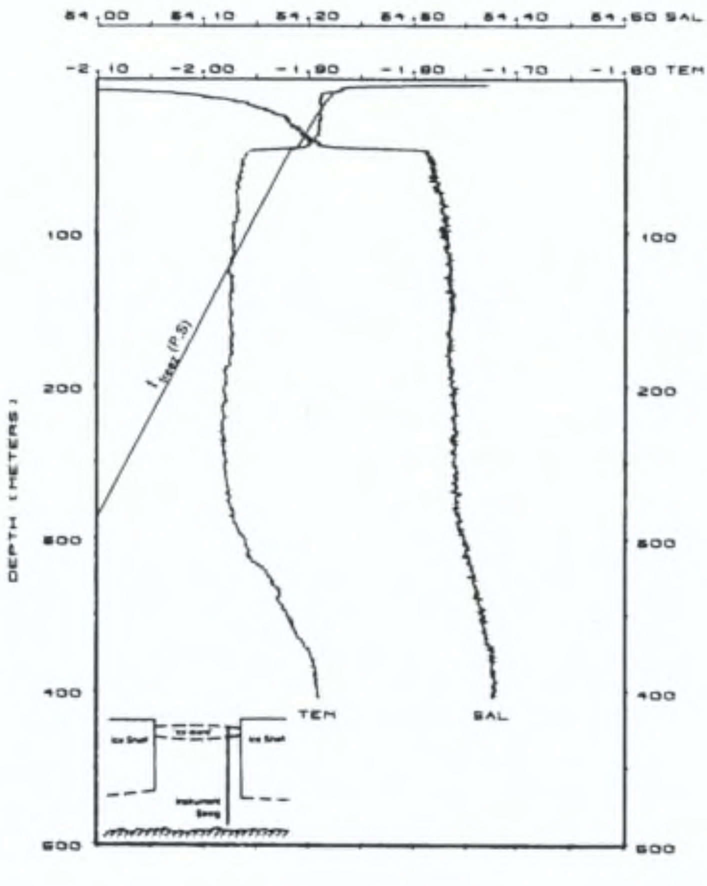

Figure 5.2: Temperature and salinity profiles in the Jutulgryta rift. The line of the freezing point, as a function of pressure and salinity, reveals the supercooled state of the upper section of the water column. The inset in lower left corner shows the rift, to scale, in relation to the surrounding ice shelf [from *Orheim et al.*, 1990].

The accounts of the thickness of ice accumulation in the rift given by *Orheim et al.* [1990] and *Osterhus and Orheim* [1992] are less clear. The former authors report finding 11.1 meters of solid ice underlain by 27 meters of slushy ice intercepted with what they describe as thick water layers, which gives a total ice and slush thickness of 38.1 meters. The latter authors explain how 23 months later they found 40 meters of solid ice and they do not mention whether any slush was present beneath. They conclude that considerable ice had accumulated in the intervening period, despite the fact that the difference in ice thickness between the two observations is 1.9 meters.

This conclusion, however, should be assessed with some skepticism. It is difficult to imagine a process capable of transforming more than 27 meters of slush into a solid body of ice in less than two years. Sea ice studies [e.g. *Weeks and Ackley*, 1982] show that heat loss to the atmosphere produces a layer of ice at a rate of 1 to 2 cm per day for the first meter or so of ice. Such rates, which are bound to get lower the thicker the ice grows, are not sufficient to account for the observations of *Osterhus and Orheim* [1992]. Nor is heat loss to the ice shelf, a process that is discussed in more detail above in section 3.2.2. One plausible explanation is that the authors were actually witnessing the effect of heat loss through their instrument cable or this cable having been the platform for ice formation and the supercooling release of the water through which it was suspended. *Lewis and Perkin* [1985] report on, and provide the photograph of, an ice cylinder 80cm in diameter which formed in 30 days around a current meter deployed below sea ice. Such an explanation could account also for the fact that *Osterhus and Orheim* [1992] have not observed any slush beneath the solid ice. If this is the case, then it is impossible to distinguish the quantity of ice formed directly on the cable from that has formed as an accumulation of frazil crystals. Therefore, what can be inferred from the observations of the two groups of authors above is that no more than 1.9 meters of frazil ice had accumulated in the 23-month period.

Uncertainty also surrounds the amount of ice reported by *Orheim et al.* [1990], which would be the ice that accumulated in the rift since its opening. The authors do not indicate the thickness of the water layers that they observed intercepting the slush. Furthermore, a part of the 11.1 meters of solid ice on the top must be made of normal sea ice, snow, and ice shelf fragments that has fallen into the rift. Taking account of this in addition to the intercepting water layers, one could suppose very approximately that no more than about 25 meters of frazil ice crystals accumulated from the moment the rift opened. As for most of the rifts and crevasses considered in the simulations below, no estimate of the age of the rift is available.

From the data provided by *Orheim et al.* [1990], the width of the rift at the top can be calculated to be 340 meters and its initial vertical extent from sea level is 300 meters.

5.1.2 Experiment and discussion

Among the components of the Jutulgryta observations, ambient temperature and salinity are already used in the last chapter to fix model parameter values employed in the current simulations. Furthermore, the above discussion shows that there is some doubt concerning the total amount of ice accumulating in the rift. Also uncertain is the time span it took to build up this accumulation. Less doubtful, however, is the maximum amount of ice that accumulated in the 23 months separating the observations of *Orheim et al.* [1990] from those of *Osterhus and Orheim* [1992].

As can be seen from Figure 4.10a, for the case of an entrainment constant of 0.0720, the amount of ice accumulated during a one month period is lowest at the end of the 50-year run and is equal to 0.0487 meters/month for month 600. The highest rate occurs just after the turning point and has the value of 0.0592 meters/month for month 21. For a time interval of 23 months, these values correspond to a total thickness of deposited ice ranging between 1.1201 and 1.3616 meters. This compares rather favorably with the maximum 1.9 meters inferred from the Jutulgryta observations.

Such relatively good agreement suggests that the model acceptably simulates the rate of frazil ice accumulation.

5.2 Rift near the front of the Ronne Ice Shelf

Located some 30km inland from the front of the northwest corner of the Ronne Ice Shelf (Figure 5.1), at 75°30'S, 59°00'W, this rift is a good candidate for being the location at which a future calving event will take place. The interest of studying the case of this rift is further enhanced by the fact that it contains a relatively thick layer of ice.

5.2.1 Setting and observations

The description of the rift comes from the work of *King* [1994]. The author used an electronic distance meter to obtain the above-surface profile of the rift while the underneath configuration was revealed by seismic methods. He measured the width of the rift to be 340 meters and its vertical extent below sea level to cover 300 meters. This creates the fortunate coincidence of both the Ronne rift and the Jutulgryta one having the same dimensions, thus facilitating comparison. The rift profile compiled by *King* [1994] is presented in Figure 5.3 and it shows two interesting features from the point of view of the current work.

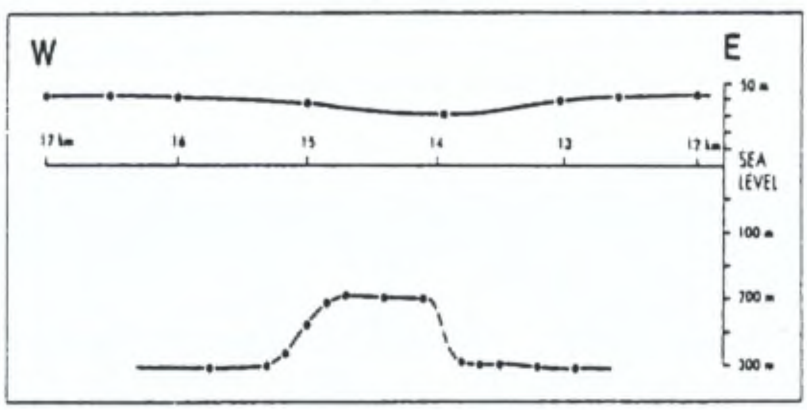

Figure 5.3: Profile of the rift at the northwest corner of the Ronne Ice Shelf. The profile crosses the rift at an oblique angle, therefore, the 1km width shown corresponds in reality to 340 meters [from *King*, 1994].

The first is the gently curved shapes of the bottom edges of the walls of the rift, rather than the sharp angular edges that one would expect from a fracture in ice. This is a strong indication that melting is taking place at the bottom portion of the ice wall/ocean interface and that, furthermore, net mass loss increases progressively downwards. Both characteristics are predicted by the rift model as demonstrated in the previous chapter.

The second interesting feature of the profile in Figure 5.3 is the large thickness of the ice layer filling what used to be an open rift, an occurrence over which *King*

[1994] does not hypothesize. The profile shows that there are more than 200 meters of ice in the rift below sea level, compared to about 40 meters in the case of Jutulgryta. A possible explanation is a difference in age between the two rifts. The proximity of Jutulgryta to the grounding line suggests that it might be relatively young. Another possible explanations, in light of the discussion of the previous chapter, is that the discrepancy between the two rifts results from a difference in the initial ambient temperature and salinity. Therefore, one of the objectives of the current experiment is to examine whether the model would simulate abundant ice deposition in the Ronne rift as a result of ambient conditions. For that, the possible initial ambient properties in the cavity need to be determined.

5.2.2 Initial ambient temperature and salinity

King [1994] did not access the water in the rift, consequently, the initial properties of the ambient fluid filling it have to be inferred from other sources.

Vaughan et al. [1994] review the oceanographic surveys that have been done off the front of the Ronne Ice Shelf. All these studies agree in revealing that there is a plume of Ice Shelf Water (ISW) passing exactly beneath the site of the Ronne rift. Furthermore, *Vaughan et al.* [1994] note how the available observations show that the plume emerges at the level of the ice shelf base, which implies that it hugs the underside of the shelf and that it fills part, if not all, of the water column at that point. Subsequent oceanographic profiles from the same region obtained by *Nicholls et al.* [1998] demonstrate that the ISW emerging at that point from beneath the Ronne Ice Shelf does indeed fill all of the water column.

Therefore, the temperature and salinity of the ISW emerging from beneath the ice shelf at the location of the rift are adopted as those of the fluid initially filling the cavity in the simulation. The values of these two parameters can be found from the profiles measured by *Foldvik et al.* [1985]. At 300 meters depth in these profiles, ISW temperature is -2.08°C and the corresponding salinity is 34.68.

5.2.3 Standard experiment and discussion

With the above information on the initial dimensions and ambient water properties of the rift, a 100-year simulation is performed and the results are plotted in Figure 5.4.

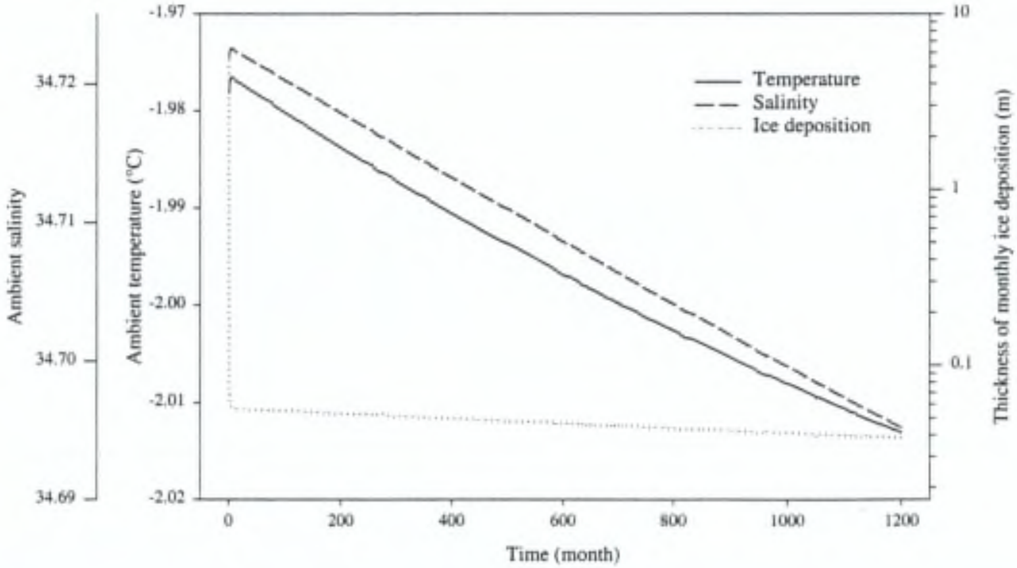

Figure 5.4: The 100-year evolution of monthly ice deposition, ambient temperature and salinity for the Ronne rift experiment. Notice that the scale for ice thickness is logarithmic.

Compared to Jutulgryta (Figure 4.10), the qualitative difference in parameter evolution during the first few months is immediately apparent. Most striking is the large amount of ice (5.8514 meters) already deposited after the first month. Obviously, in light of the results of section 4.2.1, this is a consequence of the relatively low initial ambient temperature in the Ronne rift case. Indeed, inequality 4.4 indicates that this is a high-ice production system. Predictably, enhanced ice generation pushes the ambient temperature and salinity at the end of the first month up compared to their initial values as can be seen from Figure 5.4. After the first month, the upward temperature and salinity trends persist while ice generation continues to fall. However, the system quickly reaches a turning point around month 4 where parameters enter a long phase of much slower change. The underlying mechanism of such evolution is a chain of interdependent processes that progresses in the opposite direction to that of the Jutulgryta situation exposed in section 4.4.2. In the current situation, initially, water which is relatively near the freezing point at the base of the rift engenders high frazil generation. The large quantities of emitted heat and salt render conditions much less favorable for continued high crystal output and for direct freezing on the rift's wall. Simultaneously, ambient conditions become more and more suitable for enhanced melting at the ice/water interface of the bottom section of the cavity. These processes are illustrated in Figure 5.5. Consequently, around month 4, the effects of melting and freezing in the system achieve a near balance and the turning point is reached.

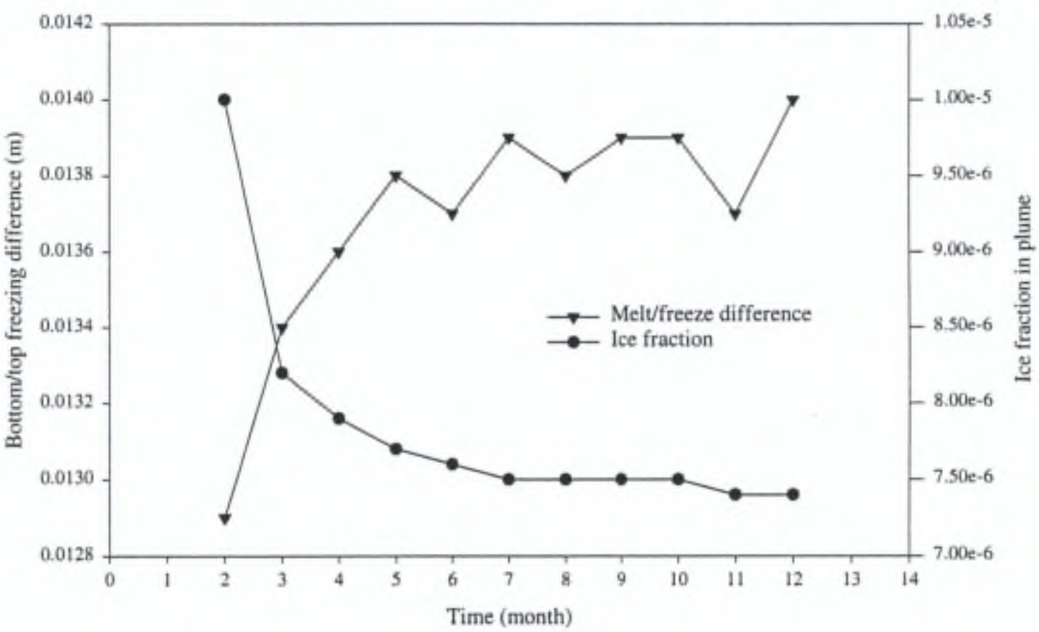

Figure 5.5: The change during the first 12 months in the crystal fraction of the plume at the moment of its termination at the top of the cavity and the wall's melt/freeze difference. This latter parameter, which is discussed in detail in section 4.4.2 is the thickness of ice directly freezing on the wall at top of the cavity subtracted from the thickness of ice ablated from lower-most point of the wall. Points for the first month are not included since they are largely off scale. Notice how the relative importance of melting increases with time while ice formation in the plume decreases. These tendencies are opposite to those shown in Figure 4.11 for the early months of the Jutulgryta case.

Beyond the turning point, temperature, salinity and ice generation rate begin to fall slowly as can be seen from Figure 5.4. From this point onward, the system evolves in the same manner as in the Jutulgryta situation discussed in section 4.4.3.

This similarity is not a coincidence. Its basic general reason is the tendency of the system, through phase changes, to regulate itself to achieve a certain near-balance situation. In the Jutulgryta case, the system was "too warm", hence, it is brought closer to near-balance through prevalent melting in the early months. In the Ronne rift, on the other hand, the system was too far off in the other direction, and near-balance was attained through prolific freezing. As a result, the ambient parameters of the two systems, at the turning points of each one, are closer to each other than they were at the beginning of their respective simulations and their subsequent declines are comparable. Temperature in the Jutulgryta case drops by 0.0379°C between month 19, just after the turning point, and month 1200, while the equivalent value for the Ronne rift case is 0.0366°C in the period from month 5 to 1200. Salinity in the former case drops by 0.0270 and in the latter by 0.0274. After a 100-year simulation, a total thickness of 58.0243 meters of frazil crystals had accumulated in Jutulgryta, compared to 61.9516 meters in the case of Ronne.

5.2.4 Simulation of ambient water periodic renewal

At the beginning of section 4.3, the idea is proposed that high-ice output rifts or bottom crevasses could, on the long term, have significantly thicker accumulations of frazil crystals if their ambient waters were to undergo seasonal renewal. The Ronne rift setting offers the occasion to test this idea.

The above standard experiment is repeated here, except that the program is modified to allow the ambient temperature and salinity to revert to their initial values every 12 months throughout the 100-year run. All other changes occurring during the intervening periods between renewals are maintained, including ice accumulation at the top of the water column and modified cavity dimensions.

From the data contained in Table 5.1, periodic annual renewal of ambient water results in more than doubling the final amount of accumulated ice at the end of a

100-year simulation. A glimpse at Figure 5.6 immediately gives an idea of the explanation.

Experiment description	*initial ambient temperature (°C)*	*initial ambient salinity*	*total ice accumulation (m) without renewal*	*total ice accumulation (m) with renewal*
Ronne rift with ISW	-2.0800	34.6800	61.9516	129.7831
Ronne rift with MWDW	-1.5000	34.5000	56.0303	0.0425

Table 5.1: Total thickness of ice accumulated at the end of 100-year runs covering four experiments: Ronne rift with Ice Shelf Water (ISW) initially filling the cavity; Ronne rift with Modified Weddell Deep Water (MWDW) initially filling the cavity; and both these experiments repeated with a periodic, 12-months cycle, renewal of ambient water.

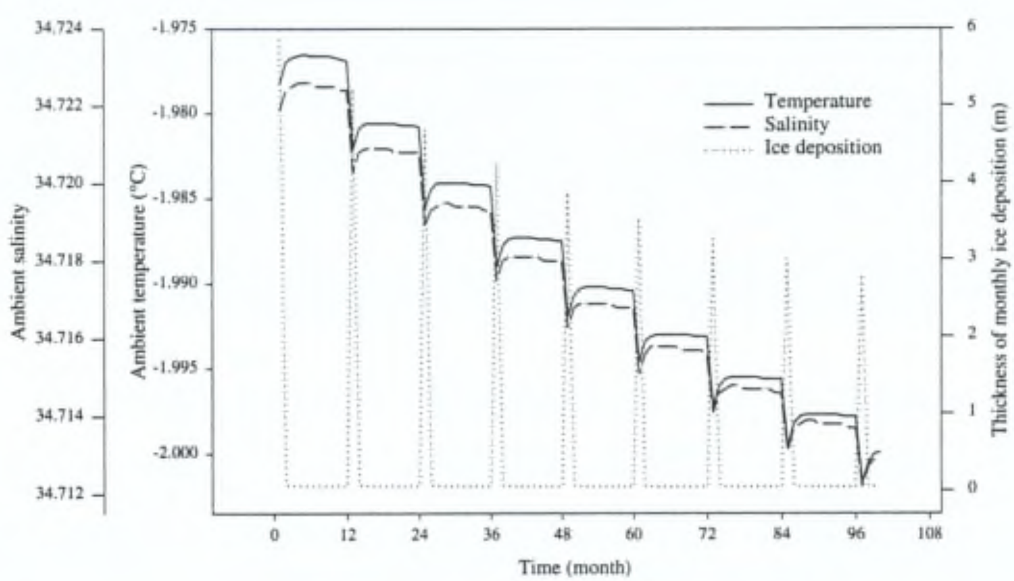

Figure 5.6: Evolution of monthly ice deposition, ambient temperature and salinity for the Ronne rift experiment with periodic ambient water renewal, which, in this case, occurred every 12 months. Only the first 100 months of the 100-year simulation are shown in order to render parameter patterns more visible.

The standard experiment above shows that the initial intense burst of ice generation is capable, through its effect on ambient temperature and salinity, to create conditions that sharply bring down ice output. In the current experiment, however, the fact that every 12 months initial conditions are restored in the cavity means that the high-ice output regime is reactivated each time. In Figure 5.6, this is manifested by the spikes, at the beginning of each period, in the monthly ice deposition profile. The same figure also shows how temperature, salinity and ice generation rate qualitatively evolve in the same manner exhibited during the leading months of the standard experiment (Figure 5.4). Hence, ice output quickly falls back after the first month of each new period in the current situation.

Furthermore, Figure 5.6 reveals how the amplitude of the ice-production spikes decreases progressively with time. This is obviously a consequence of the same mechanism, discussed in section 4.4.3, responsible for the long-term decline of ice output in the Jutulgryta case. Namely, the truncation of the vertical extent of the cavity due to ice accumulation at the top.

5.2.5 Experiment with MWDW

Vaughan et al. [1994] note that the studies they review suggest that the positions of ISW plumes emerging at the front of the Ronne Ice Shelf, including the one that passes beneath the rift being simulated here, appear to be stable. However, they do not manage to conclusively explain this by the topography of the ice shelf underside or the thickness of the water column.

To the east of the ISW plumes, about half way across the front of the ice shelf, *Vaughan et al.* [1994] describe how a core of Modified Weddell Deep Water (MWDW) enters the cavity beneath the ice shelf at that location. On the other hand, the oceanographic profiles measured by *Nicholls et al.* [1998] reveal the presence of a body of MWDW some 250km north of the ice shelf front, opposite the location of the rift. This body of water, which was detected at a depth of around 150 meters, overrides the denser Western Shelf Water (WSW). The same profiles show that the WSW, which extends to the ice shelf front, is blocked from entering the cavity at that location by the emerging ISW.

Since the factors determining the trajectories of ISW plumes are not yet fully understood, it would be interesting to simulate the possibility by which an ISW current would stop passing beneath the Ronne rift, thus no longer blocking the path of other water masses. In such a case, the relative proximity of the rift to the front might mean that it could be reached by the MWDW described above, hence changing the properties of the ambient water in the rift. Alternatively, such an experiment could also simulate a rift opening at the location mentioned above where MWDW does already have access to the sub ice shelf cavity.

Hence, a 100-year simulation of the Ronne rift with MWDW as initial ambient water is carried out. Representative temperature and salinity values of MWDW are obtained from the profiles of *Nicholls et al.* [1998] and they are shown in Table 5.1. It can be seen that MWDW is 0.5800°C warmer and 0.1800 less saline than ISW. With the discussion of section 4.2 in mind, the result of the simulation, displayed in the same table, indicate that it is the former difference that has the more influential effect on ice output. Thus, the Ronne rift underlain with MWDW registers approximately a 10% decrease in the total thickness of ice accumulation in the cavity over the 100-year period compared with the standard experiment.

It would also be interesting to test what would happen if, like in the case with ISW, the Ronne rift were allowed to be filled with MWDW which is periodically renewed. A 100-year run of such a configuration is performed and its result is shown in Table 5.1 along with the result of the ISW periodically-renewed experiment. The comparison between the two shows that the disparity is dramatic. In contrast with the almost 130 meters of ice forming in the rift when it is fed with ISW on a yearly basis, less than 5 centimeters managed to accumulate in the case of annually-renewed MWDW.

The reason for this is obvious. When the Ronne rift is filled with MWDW, the resulting regime, according to inequality 4.4, is a low-ice output one, even more so than the Jutulgryta case because of its higher temperature and salinity. Therefore, ambient parameter evolution during the first few months of a simulation is similar to that of Jutulgryta (Figure 4.10). This means that the monthly ice generation rate starts from a low level and increases until the turning point. However, with ambient water being renewed every 12 months, the system is never given enough time to increase its ice production levels, thus the very low final ice accumulation. This process is the exact opposite to what takes places in a high-output regime with renewed ambient water, as shown above.

5.2.6 Conclusion

The current series of experiments show that the relatively thick ice layer in the Ronne rift observed by *King* [1994] could be explained by the passage of an ISW plume beneath the rift and its interaction with it. The resulting ice production of this interaction is especially intense when ambient water is replenished on regular basis. The simulations also show that replacing ISW with MWDW, which is also allowed to be periodically renewed, results in almost no ice accumulating. The application presented in the next section considers an actual observed case where conditions are such that another low ice formation situation also occurs.

5.3 Rifts near the front of George VI Ice Shelf

The discussion of this section is based on the observations of *Lennon et al.* [1982] and *Potter and Paren* [1985]. The interpretation of field observations offered by the latter authors is particularly interesting since it is done, in part at least, with rift processes in mind.

5.3.1 Setting and observations

Lennon et al. [1982] conducted temperature and salinity measurements through the George VI Ice Shelf at seven sites situated around 70°00'S, 69°00'W. Several of the readings were taken through rifts open in the northern part of the ice shelf, while the others were taken at the ice shelf front. All rifts were located within 13km of the front. The authors describe the rifts as typically being 300 meters wide and 5km long, with a floor of "sea ice" 1 to 5 meters thick in the summer.

Potter and Paren [1985], on the other hand, estimate the typical width of the rifts to be 400 meters and the bottom of the ice shelf in that area to be located around 85 meters below sea level.

The account that *Potter and Paren* [1985] give of the surface topography of the rifts echoes that of *King* [1994]. They describe how, close to the rifts, the ice shelf is thinner than some few hundred meters back with the cliffs separating the edge of a rift from the sea ice being rounded. The authors hypothesize that this local thinning is caused by preferential melting of the exposed corner at the ice shelf base. This is further evidence, like the Ronne rift case discussed above, that melting is taking place at the bottom portion of the ice wall/ocean interface of the rift.

Potter and Paren [1985], however, then exclude the possibility that a full ice pump cycle (melting at depth and ice deposition higher in the water column) could be in action. The authors argue that the flux of sensible heat is too large to permit the development of supercooling and its relief through crystal formation.

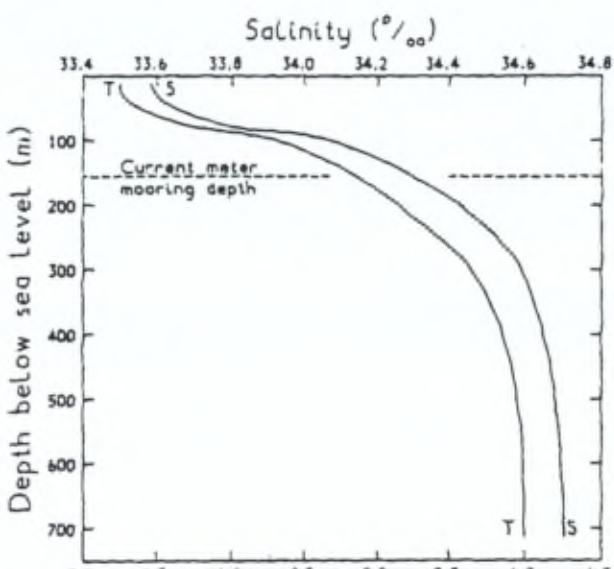

Figure 5.7: Representative temperature and salinity profiles in the George VI Ice Shelf rifts and in the ocean beneath [from *Potter and Paren*, 1985].

Indeed, as stated by *Talbot* [1988], the water beneath the George VI Ice Shelf is warmer than is found under any major Antarctic ice shelf. This is due to the fact that Circumpolar Deep Water (CDW) penetrates under the ice shelf. *Talbot* [1988] emphasizes that this is one of the few places around the Antarctic continent where such penetration occurs. The author explains this situation by the absence of HSSW which usually blocks the intrusion of CDW elsewhere due to its higher salinity.

Based on the measurements of *Lennon et al.* [1982], *Potter and Paren* [1985] compile averaged representative temperature and salinity profiles with depth which are shown in Figure 5.7.

The analysis of this information by the latter authors, in their attempt to model the circulation beneath the ice shelf, leads them to a result of interest to the current work. The formulation of *Potter and Paren* [1985] shows that the vertical velocity of the water in the rift must be downward. The authors conclude that this is feasible if melting occurs at the ice walls of the rift causing upwelling at each side which should be balanced by downwelling elsewhere. This, for the authors, explains the downward flow in the middle of the rift where the profiles were taken. Such arguments based on field observations create further support to the model being presented here.

5.3.2 Experiment and discussion

Employing the above details, an experiment is constructed to simulate one of the rifts at the northern part of George VI Ice Shelf.

The rift is taken to be 350 meters wide and to have an initial vertical extent of 85 meters. The choice of initial temperature and salinity is guided by the structure of the water column as presented by *Potter and Paren* [1985] and illustrated by the profiles of Figure 5.7. Warm CDW occupies the water column below 200 meters depth, while the volume between that depth and the base of the ice shelf is filled by a convective layer driven by the ice melt. Therefore, the initial temperature and salinity values of the ambient water filling the rift are taken to be those at 100 meters depth in Figure 5.7. This is the depth just beyond the sharp gradients in the two parameters and where the mixed layer seems to begin. Initial temperature is set to -0.7500°C while initial salinity is taken equal to 34.1000.

The experiment simulated a period of 100 years and the first noticeable aspect of the results is the relatively very low ice output. At the end of the run, only 3.9964 meters of ice had accumulated compared to 58.0243 meters in the case of Jutulgryta. Obviously, the main reason is the relatively high initial temperature of the ambient water which, at time zero, insures that the ambient freezing depth (equation (4.1)) is not even located within the rift. Consequently, all of the path of the plume is in the melting zone for a relatively longer period of time.

Compared to the rather stable profiles at Jutulgryta (Figure 5.2), observed temperature and salinity in the George VI rift cover a wide range (Figure 5.7, between sea level and 85m depth) which suggests that extensive mixing is taking place. This is not surprising in view of the low aspect ratio of the rift (the ratio of its vertical extent to its width) which renders it more accessible to the water underneath. Such a situation makes simple comparisons among observed and simulated temperatures and salinities difficult. Alternatively, in further analyzing the experiment results, use is made of the gradients of temperature and salinity profiles, which is a tool applied by the authors cited above.

Lennon et al. [1982] produced a temperature-salinity (T-S) diagram based on the measurements of five sites, of which three are rifts, in the northern George VI zone. The gradient of the T-S line, dT / dS, they calculated for the water between sea level and 85 meters depth (i.e. inside the rift) is 2.23 ± 0.10°C/psu. Furthermore, *Potter and Paren* [1985] obtained a T-S gradient of 2.30 ± 0.05°C/psu from the 5-month measurements of a device left during the Antarctic winter at a depth of 156 meters as shown in Figure 5.7. The maps provided by the authors show that the device was beneath one the rifts considered here.

Both groups of authors test their calculated gradients with the value derived theoretically by investigators such as *Gade* [1979] whose work is already mentioned and used in section 3.2.3 above. Based on this work, *Potter and Paren* [1985] estimate that the theoretical gradient of a T-S line for the range of temperature and salinity presented in Figure 5.7 is 2.50 ± 0.05°C/psu. The authors consider that the discrepancy between the theoretical and observed gradients to be small. They think that the difference may be due to surface melt water percolating into the rift cavity thus diluting salinity without absorbing latent heat.

The experiment of this section, however, shows how rift processes could offer another plausible explanation. In fact, a T-S line is obtained for the temperatures and salinities of the first 51 months of the simulation. This is the period before frazil ice output begins to pick up. The gradient of the line is 2.53°C/psu, which shows excellent agreement with the theoretical gradient. This is expected since the period considered represents fresh ice melting in ocean water, which is the assumption of the theoretical gradient. Moreover, the gradient of the T-S line for the period from the beginning of significant ice production to the turning point, months 52 to 65, is obtained. The result, 2.33°C/psu, also agrees very well with the values observed by *Lennon et al.* [1982] and *Potter and Paren* [1985].

5.3.3 Conclusion

As it is mentioned above, *Potter and Paren* [1985] excluded the possibility that ice crystals are being formed in the ascending plumes inside the rifts. However, the discussion of this section shows that allowing for some formation, and the ensuing modification of temperature and salinity, could actually explain the observed T-S gradients. The simulation shows that the gradients after the turning point fall far below the theoretical and observed values. This could be taken as an indication that mixing with ocean water occurs on a time scale comparable to the time necessary to reach the turning point for monthly ice deposition. At that point in this simulation, only 0.0443 meters of frazil had accumulated.

5.4 The disappearing basal crevasses of the Ross Ice Shelf

Jezek and his coworkers conducted subsurface surveys at several locations of the Ross Ice Shelf. The electromagnetic sounding techniques they used reveal the presence of bottom crevasses and give an idea about their shapes and dimensions. Some of the observations strongly suggest that these crevasses are being filled with ice. The lack of information about the temperatures and salinities of the water filling them means that the comparison with simulations will concentrate on ice accumulation rates.

5.4.1 Bottom crevasses at J9

A series of electromagnetic sounding profiles obtained by *Jezek et al.* [1979] revealed the presence of several bottom crevasses or groups of crevasses beneath site J9 (82°22′S, 168°37′W) of the Ross Ice Shelf. The collected profiles showed that these crevasses are not merely thin wedges in the lower part of the ice shelf, but that they actually have extensive widths as well as heights. As an example, the largest crevasses detected by *Jezek et al.* [1979] at J9 are 120 meters high, almost as large at their bases and have a lateral extent of at least 2.3km. The authors describe the vertical cross section of the crevasses as triangular. In the simulations below, however, such a shape cannot be used since inequality (3.25) would be violated at the apex of the triangle and the top narrow section of the cavity. Therefore, in the experiments, a rectangular cavity shape is used as an approximation. In doing so, two quantities from the observed triangular crevasse dimensions are nevertheless preserved, namely, the total area of the vertical cross section and the vertical extent. The importance of maintaining the latter quantity is emphasized by the work of section 4.5. In such a setup, a triangular bottom crevasse of which the width at the base is equal to its vertical extent would result in a rectangular cavity with the same vertical extent and a constant width of one half the basal width of the observed triangular crevasse.

During further investigation of bottom crevasses in the Ross Ice Shelf, *Jezek and Bentley* [1983] noticed that, in most cases, crevasses are no longer detectable about 100km down-flow. The authors estimate that this distance is covered in about 250 years. *Jezek and Bentley* [1983] present a calculation which shows that such a disappearance is too rapid to be explained by simple vertical strain. Hence, they conclude that the crevasses become undetectable because they "freeze closed". The authors do not hypothesize on the nature of that freezing.

To test this idea using the current model, a simulation of one of the large triangular crevasses observed at J9 by *Jezek et al.* [1979] is performed. The rectangular cavity used in the experiment has a vertical extent of 120 meters and a width of 60 meters. Its lower edge is located at the ice shelf/water interface at J9 which is found to be at 360 meters below sea level by *Jacobs et al.* [1979]. The work of these latter authors, which is based on measurements conducted when the ice shelf at J9 was cored all the way to the ice/ocean boundary, also gives the appropriate parameter values for the water filling the crevasse initially. Hence, ambient temperature at the beginning of the experiment is fixed at -2.1000°C while the corresponding salinity is 34.3900.

The experiment simulated 250 years, the period after which *Jezek and Bentley* [1983] could no longer detect the majority of crevasses. At the end of the run, 68.0264 meters of ice had accumulated (74.6606 meters in the case of annual renewal of ambient water). This is a significant quantity which covers more than half of the cavity's vertical extent. However, that leaves the other part of the crevasse which could be detected, especially that *Jezek et al.* [1979] were able to detect crevasses that are only 30 meters high.

With the assumption that the model is producing a reasonable amount of ice, other possible reasons should then be invoked to account for the disappearing crevasses. Even more so in light of the results of sections 4.4.3 and 5.2.4 above, which show that ice output in the cavity is continuously diminishing with decreasing vertical extent, including in high-ice output cavities such as the one at J9. Consequently, the model presented here could never completely fill a cavity anyhow.

The main explanations that Jezek and his coworkers present to elucidate crevasse disappearance could themselves be related to freezing processes in the crevasses. For example, *Jezek and Bentley* [1983] describe how some large crevasses could penetrate all the way up to permeable ice layers thus permitting the percolation of brine into these layers. The authors state that the brine masks crevasses beneath it rendering them undetectable to sounding methods. Brine layers described here are comparable to the slushy ice that *Orheim et al.* [1990] reported finding in the Jutulgryta rift. It is therefore possible to hypothesize that crystal/sea water mixtures that are likely to be formed as a result of the processes described in this model mask the crevasses in which they form.

Furthermore, *Jezek and Bentley* [1983] cite an unpublished work by Jezek in which he uses models to compare reflected signals from water filled crevasses to those from what he describes as frozen ones. The author concludes that the detection methods he is employing will not be able to discern the presence of "frozen" crevasses.

Vertical strain of the ice shelf, which *Jezek and Bentley* [1983] consider but is not included in the current rift model, is another factor that could play a partial role in reducing basal crevasse heights. However, the details of the calculation made by the authors should be treated with caution since they take into account only mass accumulation at the top surface of the ice shelf and do not include possible mass accumulation (or indeed ablation) at the ice/ocean interface.

5.4.2 Bottom crevasses at the Ross Ice Shelf grounding line

The observations and experiments discussed in this section present further evidence towards the arguments of the previous section concerning crevasse disappearance.

In fact, the field observations of *Jezek and Bentley* [1983] provide the opportunity for an interesting comparison. The authors describe how large crevasse (more than 200 meters high) opening at the grounding line of the Ross Ice Shelf disappear downstream while crevasses less than 50 meters high persist to the front of the ice shelf.

In this experiment, therefore, two crevasses of different sizes at the grounding line are simulated. A detailed map of the Ross Ice Shelf bottom crevasse distribution presented by *Jezek* [1984] shows a large crevasse, 210 meters high, at the grounding line midway between the Nimrod Glacier and Beardmore Glacier. *Jezek and Bentley* [1983] do not explicitly discuss the width of the crevasses at the grounding line. However, a diagram by *Jezek* [1984] shows that the assumption is that, like the observed cases of J9 crevasses, grounding line crevasses have same height and width at the base. Hence, the large crevasse is simulated by a cavity 210 meters high and 105 meters wide. This is compared to a small crevasse simulated by a cavity 40 meters high and 20 meters across.

The starting depth of the two cavities in the simulation is taken to be 700 meters below sea level. This is deduced from a contour map of the sea floor topography beneath the Ross Ice Shelf provided by *Clough and Hansen* [1979].

Initial ambient water parameters in the cavities are those taken at 700 meters depth from the temperature and salinity profiles of the ocean at the front of the ice shelf compiled by *Jacobs et al.* [1979]. The reasoning is that these profiles show that HSSW properties measured beneath site J9 at the lower portion of the water column, far from the ice shelf/water interface, agree well with the properties of the same water type at the front of the shelf. The analysis of *MacAyeal* [1984] demonstrates that HSSW penetrates into most parts of the sub-ice shelf cavity including the location near the grounding line at which the cavities in this simulation are supposed to be initially. *MacAyeal* [1984] also states that the properties of HSSW at the front remain relatively preserved beneath the shelf until ice is encountered and melting takes place. Hence, the initial ambient water temperature in the cavities is fixed at -1.8900°C and the salinity at 34.8600.

After a run simulating 250 years, 122.6513 meters of ice had accumulated in the larger ice shelf against 10.7269 meters only in the smaller one. Such a result is not surprising in light of the findings of section 4.5.1.

5.4.3 Conclusion

The field observations of disappearing bottom crevasses cited in this section provide additional strong evidence to support the main hypothesis of this work. The disappearance, however, cannot be explained by a complete filling of the crevasse by frazil crystals but rather by the effects, discussed above, associated with a significant partial accumulation of ice in the cavity.

On the other hand, the model presented here provides a plausible explanation for the different observed behavior of small crevasses, which remain detectable until the ice front, from larger ones which disappear relatively quickly down stream from the grounding line.

Furthermore, the fact that smaller crevasses remain detectable is an indication that whatever is making their larger counterparts disappear, despite following the same trajectory in space, must be independent from any exterior, path-dependent, factors. Inner cavity processes, and their associated masking effects, are again a plausible explanation.

5.5 Possible implications for the Grand Chasm

One of the largest fracture features in an ice shelf ever recorded, the Grand Chasm was a giant rift that traversed the northern part of the Filchner Ice Shelf in a southeasterly-northwesterly direction between Coats Land and Berkner Island. Indeed, it was so impressive that it was declared "the grandfather of all crevasses" by *Neuburg et al.* [1959]. These investigators, who were among the first to give an account of the rift, estimated its length at the time to be 100km and its largest width to be 5km. *Swithinbank et al.* [1988] describe how in 1973 the rift's length had grown to 115km and its widest point to 11km and then to 19km in 1985. The following year, the rift was at the origin of a major calving event which produced three giant icebergs.

Grosfeld et al. [1998] employ a multidisciplinary approach to establish the existence of marine ice beneath the Filchner Ice Shelf. Two investigative tools that the authors use are a 3-dimensional model for sub-ice shelf oceanic circulation and a 2-dimensional ice dynamic model. The oceanic model shows that HSSW flows under the eastern part of the ice shelf while ISW emerges from under the western part of the front along the east coast of Berkner Island. Both the oceanic and ice dynamic models predict that marine ice would form preferentially beneath the northwestern part of the Filchner Ice Shelf while little ice accumulation would occur beneath the northeastern section of the shelf. However, direct observation of the Grand Chasm, including its eastern part, indicate that it contains at least tens of meters of ice. Furthermore, a green iceberg, which the significance as a clue to marine ice formation is discussed in chapter 1, has been identified as having originated from the easternmost iceberg among the three that resulted from the calving event of 1986. Therefore, *Grosfeld et al.* [1998] explicitly propose the idea that the Grand Chasm has provided the environment for a local ice pump to take place which produced the marine ice under the northeastern Filchner Ice Shelf. This conclusion is supported by the work of the previous sections of this chapter which shows that both HSSW and ISW are associated with frazil crystal production.

This same work, as well as that of section 4.2, also demonstrates that ISW is accompanied with a higher output of ice crystals than HSSW, especially when ambient water is periodically renewed in the cavity. This observation leads to another possible application of the current model to the Grand Chasm case, albeit a more speculative one.

A photograph taken by *Neuburg et al.* [1959] of the Grand Chasm in 1957, and is reproduced in Figure 5.8, clearly shows what the authors called an "offset" near the rift's center. The Chasm had been divided into two halves and the western half is more advanced to the north than the eastern one. It is tempting to apply the results of the current model to account, at least partially, for the occurrence of such a configuration.

Figure 5.8: The Grand Chasm viewed from the east in 1957 with the offset clearly apparent near its center [form *Neuburg et al.*, 1959].

The argument proceeds as follows. The eastern part of the Grand Chasm was underlain by HSSW while beneath its western part ISW was flowing. This would result in more ice accumulating in the western part than in the eastern one. The remaining volume of the cavity would obviously be filled with water and there would be less of that in the western section since the ice is thicker there. Due to the lower density of ice, the total mass (ice and water) filling the volume of the western section would be less than that of the eastern section. If the force applied to all sections of the rift is equal, then this force would be acting on lesser mass in the west, thus pushing that part of the rift further north than the eastern part in the same period of time and producing the observed offset in the middle.

Chapter 6

General conclusions

This work puts forward a new possible setting for the formation of marine ice in the vicinity of the grounding line, a zone where hitherto melting from the Deep Thermohaline Circulation was thought to prevail. It also demonstrates that marine shelf ice could be more readily recovered and studied by exploiting a combination of climatic and formation conditions of certain ice shelves.

Recent ice-ocean modeling and field work efforts are increasingly underlining the importance of marine ice formation and accretion beneath Antarctic ice shelves. Improved comprehension of these processes is indispensable for accurate mass balance estimations of ice shelves. It is shown here that an important segment of the bulk of small to medium Antarctic shelves could be formed of marine ice. An ice shelf such as Nansen, which is located further to the north than the Ross Ice Shelf, could show signs of global warming earlier than its much larger counterpart by virtue of its location. The thermal properties of Antarctic shelves, and thus their heat exchange with the atmosphere and/or the ocean, could be modified if a certain proportion of their mass were composed of saline, bubble free ice instead of fresh, bubbly continental ice.

The modeling effort undertaken here serves to define the main parameters necessary for the process of frazil ice formation in rifts and basal crevasses to occur and identifies the conditions that control the extent of ice accumulation. An attempt is also made to devise an empirical tool by which the ice producing potential of a certain site could be assessed.

More specifically, this work could have important implications for the following aspects of Antarctic research.

First, keeping in mind that rifts and basal crevasses are quite common, it is possible that observations of "thick" marine ice accumulation beneath ice shelves could in fact be marine ice formations in bottom crevasses. The effect can be further enhanced since, in many locations, bottom crevasses occur as a series of closely-spaced fractures. This point can be relevant when theoretical investigators use such observations to test their models of sub-ice shelf circulation. Hence, the results of these models could be incorrectly validated or rejected by the presence of marine ice that had not been produced by the general circulation simulated in the experiments.

Second, although the relative fraction of an ice shelf occupied by a single rift or basal crevasse is always small, this does not exclude the possibility that a higher portion of the ice shelf is made of marine ice as a result of the process explored in this work. This can take place as follows. The grounding zone of an ice shelf is a point of obligatory passage for continental ice on its way to the sea. The fact that a fracture has occurred at the grounding line indicates that the conditions for such an occurrence had been satisfied and there is nothing that prevents them from continuing to be so after that first fracture moved downstream. Consequently, rifts or bottom crevasses will continue to open, be filled with marine ice before pursuing their paths towards the front. The result is that the grounding zone could become a point for manufacturing marine ice and exporting it downstream where it becomes an integral part of the ice shelf body.

Third, rifts are common features in the frontal zones of ice shelves where, very often, they are precursors for iceberg calving events. Calving is by far the most important manner in which Antarctica looses mass. Studies of the dynamic stability of Antarctic shelves and their fragmentation mechanisms would benefit from better insight into the interaction between shelf rifts and crevasses with the ocean. Specifically, It is quite plausible that the dynamic properties of the ice filling the rifts and its response to atmospheric and/or oceanic variations would be different if this glue or cement was mainly composed of a homogeneous body of marine ice resulting from a process such as the one described in this work rather than the mixture described by the authors cited in the first chapter. Furthermore, with global change in mind, model experiments conducted here clearly show how changing oceanic conditions could have a drastic effect on the amount of ice accumulating in frontal rifts.

Finally, and this last remark is related to the very first paragraph of this dissertation, rifts could and are indeed being used as valuable access to the water beneath the ice shelves in which they occur. However, this work shows that the results of any measurements conducted through such an access should be interpreted with caution. Measured parameters could be reflecting the effects of the local processes discussed here rather than the properties of the main body of water in the sub-ice shelf cavity.

This aside, there is no disputing the remainder of Barrett's quote; crevassed areas on ice shelves are indeed worth a closer look, and perhaps their scientific value is beginning to show.

References

Baines, W. D., and J. S. Turner, Turbulent buoyant convection from a source in a confined region, *J. Fluid Mech., 37*(1), 51-80, 1969.

Barkov, N. I., *Ice shelves of Antarctica*, A. A. Balkema, Rotterdam, 1986.

Baroni, C., ed. *Mount Melbourne quadrangle, Antarctic geomorphological and glaciological 1:250.000 map series*. Siena, Museo Nazionale Dell'Antartide, 1996.

Barrett, P. J., Seawater near the head of the Ross Ice Shelf, *Nature, 256*, 390-392, 1975.

Boltz, D. F., *Selected topics in modern instrumental analysis*, Printice-Hall, New York, 1952.

Bombosch, A. and A. Jenkins, Modeling the formation and deposition of frazil ice beneath Filchner-Ronne Ice Shelf, *J. Geophys. Res., 100*(C4), 6983-6992, 1995.

Bombosch, A., Interactions between floating ice platelets and ocean water in the southern Weddell Sea, in *Ocean, ice, and atmosphere: interactions at the Antarctic continental margin, Antarct. Res. Ser.*, vol. 75, edited by S. S. Jacobs and R. F. Weiss, pp. 257-266, AGU, Washington, D. C., 1998.

Bo Pederson, F., Dense bottom currents in rotating ocean, *J. Hydraul. Div. Am. Soc. Civ. Eng., 106*, 1291-1308, 1980.

Borfecchia, F., and M. Frezzotti, *Satellite Image Mosaic of the Terra Nova Bay Area (Victoria Land, Antarctica)*, ENEA, 1991.

Bowen, R., *Isotopes and climates*, Elsevier Applied Science, London, 1991.

Cipra, B., Mathematicians open the black box of turbulence, *Science*, 269, 1361-1362, 1995.

Clark, I., and P. Fritz, *Environmental isotopes in Hydrogeology*, Lewis Publishers, Boca Raton, 1997.

Clough, J. W., and B. L. Hansen, The Ross Ice Shelf project, *Science, 203*, 433-434, 1979.

Cox, G. F., and W. F. Weeks, Numerical simulations of the profile properties of undeformed first-year sea ice during the growth season, *J. Geophys. Res., 93*(10), 12449-12460, 1988.

Daly, S. F., Frazil ice dynamics, *CRREL monograph, 84-1*, 46 pp., U. S. Army Cold Reg. Res. Eng. Lab., Hanover, N. H., 1984.

Determann, J., and R. Gerdes, Melting and freezing beneath ice shelves: implications from a three-dimensional ocean-circulation model, *Ann. Glaciol., 20*, 413-419, 1994.

Doake, C. S. M., Thermodynamics of the interaction between ice shelves and the sea, *Polar Rec., 18*, 37-41, 1976.

Doake, C. S. M., and D. G. Vaughan, Rapid disintegration of the Wordie Ice Shelf in response to atmospheric warming, *Nature, 350*, 328-330, 1991.

Eicken, H., H. Oerter, H. Miller, W. Graf, and J. Kipfstuhl, Textural characteristics and impurity content of meteoric and marine ice in the Ronne Ice shelf, Antarctica, *J. Glaciol., 40*(135), 386-398, 1994.

Eicken, H., H. Fischer, and P. Lemke, Effects of the snow cover on Antarctic sea ice and potential modulation of its response to climate change, *Ann. Glaciol., 21*, 369-376, 1995.

Eicken, H., Driving modes and rates of ice growth in the Weddell sea from microstructural, salinity, and stable-isotope data, *Antarct. Res. Ser., 74*, 89-122, 1998.

Elder, S. A., and J. Williams, *Fluid physics for oceanographers and physicists, Second edition*, Butterworth-Heinemann, Oxford, 1996.

Ellison, T. H., and J. S. Turner, Turbulent entrainment in Stratified flows, *J. Fluid Mech., 6*, 423-448, 1959.

Engelhardt, H., and J. Determann, Borehole evidence for a thick layer of basal ice in the central Ronne Ice Shelf, *Nature, 327*(6120), 318-319, 1987.

Eskinazi, S., *Fluid mechanics and thermodynamics of our environment*, Academic Press, New York, 1975.

Faure, G., *Principles of isotope geology, Smith and Wyllie intermediate geology series*, John Wiley & Sons, New York, 1977.

Fofonoff, N. P., and R. C. Millard, Algorithms for computation of fundamental properties of seawater, *UNESCO Tech. Pap. Mar. Sci., 44*, 29-30, 1983.

Foldvik, A., and T. Kvinge, Conditional instability of sea water at the freezing point, *Deep-Sea Res., 21*, 169-174, 1974.

Foldvik, A., T. Gammelsrod, and T. Torresen, Circulation and water masses on the southern Weddell Sea shelf, in *Oceanology of the Antarctic continental shelf, Antarct. Res. Ser.*, vol. 43, edited by S. S. Jacobs, pp. 5-20, AGU, Washington, D. C., 1985.

Frezzotti, M., Fluctuations of ice tongues and ice shelves derived from satellite images in Terra Nova Bay area, Victoria Land, Antarctica, *In* Y. Yoshida et al., eds. *Recent Progress in Antarctic Earth Science*, Tokyo, Terra Scientific Publishing Company, 733-739, 1992.

Frezzotti, M., Glaciological study in Terra Nova Bay, Antarctica, inferred from remote sensing analysis, *Ann. Glaciol., 17*, 63-71, 1993.

Fujino, K., E. L. Lewis, and R. Perkin, The freezing point of seawater at pressure up to 100 bars, *J. Geophys. Res., 79*(12), 1792-1797, 1974.

Gade, H. G., Melting of ice in sea water: a primitive model with application to the Antarctic ice shelf and icebergs, *J. Phys. Oceanogr., 9*, 189-198, 1979.

Germeles, A. E., Forced plumes and mixing of liquids in tanks, *J. Fluid Mech., 71*(3), 601-623, 1975.

Gow, A. J., and S. Epstein, On the use of stable isotopes to trace the origin of ice in a floating ice tongue, *J. Geophys. Res., 77*(33), 6552-6557, 1972.

Greisman, P., On upwelling driven by the melt of ice shleves and tidewater glaciers, *Deep-Sea Res., 26A*, 1051-1065, 1979.

Grosfeld, K., H. Hellmer, M. Jonas, H. Sandhäger, M. Schulte, and D. G. Vaughan, Marine ice beneath Filchner Ice Shelf: evidence from a multi-disciplinary approach, *Antarct. Res. Ser., 75*, 319-339, 1998.

Gross, G. W., P. M. Wong, and K. Humes, Concentration dependent solute redistribution at the ice-water phase boundary. III. Spontaneous convection. Chloride solutions. *J. Chem. Phys., 67*(11), 5264-5274, 1977.

Hanley, T. O'D., and G. Tsang, Formation and properties of frazil in saline water, *Cold Regions Science and Technology, 8*, 209-221, 1984.

Hellmer, H. H., and D. J. Olbers, A two-dimensional model for the thermohaline circulation under an ice shelf, *Antarct. Sci., 1*, 325-336, 1989.

Hellmer, H. H., and S. S. Jacobs, Ocean interactions with the base of Amery ice shelf, Antarctica, *J. Geophys. Res., 97*(C12), 20305-20317, 1992.

Hobbs, P. V., *Ice Physics*, Claredon Press, Oxford, 1974.

Hoekstra, P., T. E. Osterkamp, and W. F. Weeks, The migration of liquid inclusions in single ice crystals, *J. Geophys. Res., 70*(20), 5035-5041, 1965.

Holland D. M., and A. Jenkins, Modeling thermodynamic ice-ocean interaction at the base of an ice shelf, *J. Phys. Ocean., 29*, 1787-1800, 1999.

Hughes, T., On the disintegration of ice shelves: the role of fracture, *J. Glaciol., 29*(101), 98-117, 1983.

Huppert, H. E., and J. S. Turner, Ice blocks melting into a salinity gradient, *J. Fluid Mech., 100*(2), 367-384, 1980.

Jacobs, S. S., A. L. Gordon, and J. L. Ardai, Circulation and melting beneath the Ross Ice Shelf, *Science, 203*, 439-443, 1979.

Jacobs, S. S., R. G. Fairbanks, and Y. Horibe, Origin and evolution of water masses near the Antarctic continental margin: evidence from $H_2^{18}O/H_2^{16}O$ ratios in seawater, in *Oceanology of the Antarctic continental shelf, Antarct. Res. Ser.*, vol. 43, edited by S. S. Jacobs, pp. 59-85, AGU, Washington, D. C., 1985.

Jenkins, A., A one-dimensional model of ice shelf-ocean interaction, *J. Geophys. Res., 96*(C11), 20,671-20,677, 1991.

Jenkins, A., The melting of continental ice in the ocean and its implications on surface and bottom waters, *Ice in the climate system, Nato ASI Series*, vol. I 12, edited by W. R. Peltier, pp. 217-235, Springer-Verlag, Berlin, 1993.

Jenkins, A., and A. Bombosch, Modeling the effects of frazil ice crystals on the dynamics and thermodynamics of ice shelf water plumes, *J. Geophys. Res.*, *100*(C4), 6967-6981, 1995.

Jezek, K. C., C. R. Bentley, and J. W. Clough, Electromagnetic sounding of bottom crevasses on the Ross Ice Shelf, Antarctica, *J. Glaciol.*, *24*(90), 321-330, 1979.

Jezek, K. C., and C. R. Bentley, Field studies of bottom crevasses in the Ross Ice Shelf, Antarctica, *J. Glaciol.*, *29*(101), 118-126, 1983.

Jezek, K. C., A modified theory of bottom crevasses used as means for measuring the buttressing effect of ice shelves on inland ice sheets, *J. Geophys. Res.*, *89*(B3), 1925-1931, 1984.

Josberger E. G., and S. Martin, Q laboratory and theoretical study of the boundary layer adjacent to a vertical melting ice wall in salt water, *J. Fluid Mech.*, *111*, 439-473, 1981.

Keys, H. J. R., S. S. Jacobs, and D. Barnett, The calving and drift of iceberg B-9 in the Ross Sea, Antarctica, *Antarctic Science*, 2(3), 243-257, 1990.

Killworth, P. D., Mixing on the Weddell Sea continental slope, *Deep-Sea Res.*, *24*, 427-448, 1977.

King, E. C., Observations of a rift in the Ronne Ice Shelf, Antarctica, *J. Glaciol.*, *40*(134), 187-189, 1994.

Kipfstuhl, J., G. Dieckmann, H. Oerter, H. Hellmer, and W. Graf, The origin of green icebergs in Antarctica, *J. Geophys. Res.*, *97*(C12), 20,319-20,324, 1992.

Lane-Serff, G. F., On meltwater under ice shelves, *J. Geophys. Res.*, *100*(C4), 6961-6965, 1995.

Lennon, P. W., J. Loynes, J. G. Paren, and J. R. Potter, Oceanographic observations from George VI Ice Shelf, Antarctic Peninsula, *Ann. Glaciol.*, *3*, 178-183, 1982.

Lewis, E. L., and R. A. Lake, Sea ice and supercooled water, *J. Geophys. Res.*, *76*, 5836-5841, 1971.

Lewis, E. L., and R. G. Perkin, The winter oceanography of McMurdo Sound, Antarctica, in *Oceanology of the Antarctic continental shelf, Antarct. Res. Ser.*, vol. 43, edited by S. S. Jacobs, pp. 145-165, AGU, Washington, D. C., 1985.

Lewis, E. L., and R. G. Perkin, Ice pumps and their rates, *J. Geophys. Res.*, *91*(C10), 11,756-11,762, 1986.

Lock, G. S. H., *The growth and decay of ice*, Cambridge University Press, Cambridge, 1990.

MacAyeal, D. R., Thermohaline circulation below the Ross Ice Shelf: a consequence of tidally induced vertical mixing and basal melting, *J. Geophys. Res.*, *89*(C1), 597-606, 1984.

MacAyeal, D. R., Evolution of tidally triggered meltwater plumes below ice shelves, in *Oceanology of the Antarctic Continental Shelf*, *Antarct. Res. Ser.*, vol. 43, edited by S. S Jacobs, pp. 133-143, AGU, Washington, D. C., 1985.

MacAyeal, D. R., E. Rignot, and C. L. Hulbe, Ice-shelf dynamics near the front of the Filchner-Ronne Ice Shelf, Antarctica, revealed by SAR interferometry: model/interferogram comparison, *J. Glaciol.*, *44*(147), 419-428, 1998.

Mahrt, L., Momentum balance of gravity flows, *J. atmos. Sci.*, *39*, 2701-2711, 1982.

Manins, P. C., Turbulent buoyant convection from a source in a confined region, *J. Fluid Mech.*, *91*(4), 765-781, 1979.

Martin, S., and P. Kauffman, A field and laboratory study of wave damping by grease ice, *J. Glaciol.*, *27*, 283-313, 1981.

Martin, S., Frazil ice in rivers and oceans, *Ann. Rev. Fluid Mech.*, *13*, 379-397, 1981.

Maykut, G. A., and N. Untersteiner, Some results from a time-dependent thermodynamic model of sea ice, *J. Geophys. Res.*, *76*(6), 1550-1575, 1971.

Millero F. J., Freezing point of sea water, Eighth Report of the Joint Panel of Oceanographic Tables and Standards, appendix 6, *UNESCO Tech. Pap. Mar. Sci.*, *28*, 29-31, 1978.

Morgan, V.I., Oxygen isotope evidence for bottom freezing on the Amery Ice Shelf, *Nature*, *238*(5364), 393-394, 1972.

Neuburg, H. A., E. Thiel, P. T. Walker, J. C. Behrendt, and N. B. Aughenbaugh, The Filchner Ice Shelf, *Ann. Ass. Am. Geogr.*, *49*(2), 110-119, 1959.

Nicholls, K., L. Padman, and A. Jenkins, First physical oceanography results from the ROPEX98 cruise to the southern Weddell Sea, in *Filchner-Ronne Ice Shelf Programme, Report 12*, edited by H. Oerter, pp. 51-58, Alfred-Wagner Inst. For Polar and Marine Res., Bremerhaven, 1998.

Nost, O. A., and A. Foldvik, A model of ice shelf-ocean interaction with application to the Filchner-Ronne and Ross Ice Shelves, *J. Geophys. Res., 99*(C7), 14243-14254, 1994.

Oerter, H., J. Kipfstuhl, J. Determann, H. Miller, D. Wagenbach, A. Minikin, and W. Graf, Evidence for basal marine ice in the Filchner-Ronne ice shelf, *Nature, 358*(6385), 399-401, 1992.

Oerter, H. , H. Eicken, J. Kipfstuhl, and H. Miller, Comparison between ice core B13 and B15, in *Filchner-Ronne Ice Shelf Programme, Report 7,* edited by H. Oerter, pp. 29-36, Alfred-Wagner Inst. For Polar and Marine Res., Bremerhaven, 1994.

Orheim, O., Flow and thickness of Riiser-Larsenisen, Antarctica, in the Norwegian Antarctic Research Expeditions (1978/79), Publication 49, pp. 5-13, Norsk Polarinstitutt, Oslo, 1986.

Orheim, O., J. O. Hagen, S. Osterhus, and A. C. Saetrang, Glaciological and oceanographic studies on Fimbulisen during NARE 1989/90, in *Filchner-Ronne Ice Shelf Programme, Report 4,* edited by H. Oerter, pp. 120-129, Alfred-Wagner Inst. For Polar and Marine Res., Bremerhaven, 1990.

Osterhus, S., and O. Orheim, Studies through Jutulgryta , Fimbulisen in the 1991/92 season, in *Filchner-Ronne Ice Shelf Programme, Report 6,* edited by H. Oerter, pp. 103-109, Alfred-Wagner Inst. For Polar and Marine Res., Bremerhaven, 1992.

Ozum, B., and D. J. Kirwan, Impurities in ice crystals grown from stirred solutions, *A. I. Ch. E. Symp. Ser., 72*(153), 1-6, 1976.

Paterson, W. S. B., *The physics of glaciers, Third edition*, Elsevier, Oxford, 1994.

Penrose, J. D., M. Conde, and T. J. Pauly, Acoustic detection of ice crystals in Antarctic waters, *J. Geophys. Res., 99*(C6), 12573-12580, 1994.

Potter, M. C., *Mathematical methods in the physical sciences,* Prentice-Hall, Englewood Cliffs, N. J., 1978.

Potter, J. R., and J. G. Parren, Interaction between ice shelf and ocean in George VI Sound, Antarctica, in *Oceanology of the Antarctic continental shelf, Antarct. Res. Ser.*, vol. 43, edited by S. S. Jacobs, pp. 35-58, AGU, Washington, D. C., 1985.

Reeh, N., On the calving of ice from floating glaciers and ice shelves, *J. Glaciol., 7*(50), 215-232, 1968.

Rignot, E., and D. R. MacAyeal, Ice-shelf dynamics near the front of the Filchner-Ronne Ice Shelf, Antarctica, revealed by SAR interferometry, *J. Glaciol., 44*(147), 405-418, 1998.

Rist, M. A., Fracture mechanics of ice shelves, in *Filchner-Ronne Ice Shelf Programme, Report 10,* edited by H. Oerter, pp. 102-105, Alfred-Wagner Inst. For Polar and Marine Res., Bremerhaven, 1996.

Rist, M. A., P. R. Sammonds, S. A. F. Murrell, P. G. Meredith, C. S. M. Doake, H. Oerter, and K. Matsuki, Experimental and theoretical fracture mechanics applied to Antarctic ice fracture and surface crevassing, *J. Geophys. Res., 104*(B2), 2973-2987, 1999.

Robin, G. de Q., Glaciology III. Seismic shooting and related investigations, *Norwegian-British-Swedish Antarctic Expedition 1949-52. Scientific results, 5,* p. 120, 1958.

Robin, G. de Q., Formation, flow, and disintegration of ice shelves, *J. Glaciol., 24*(90), 259-271, 1979.

Ronveaux, D., *The dynamics of a small Antarctic ice shelf as indicated by an ice composition study, Ph.D. Thesis,* Université Libre de Bruxelles, 1992.

Seidensticker, R. G., Comments on paper by P. Hoekstra, T.E. Osterkamp, W. F. Weeks, The migration of liquid inclusions in single ice crystals, *J. Geophys. Res., 71*(8), 2180-2181, 1966.

Shabtaie, S., and C. R. Bentley, Tabular icebergs: implications from geophysical studies fo ice shelves, *J. Glaciol., 28*(100), 413-430, 1982.

Sheduikat, M., and D. J. Olbers, A one-dimensional mixed layer model beneath the Ross Ice Shelf with tidally induced vertical mixing, *Antarct. Sci., 2,* 29-42, 1990.

Souchez, R., J.-L. Tison, and J. Jouzel, Deuterium concentration and growth rate of Antarctic first-year sea ice, *Geophys. Res. Lett., 15*(12), 1385-1388, 1988.

Souchez, R., M. Meneghel, J.-L. Tison, R. Lorrain, D. Ronveaux, C. Baroni, A. Lozej, I. Tabacco, and J. Jouzel, Ice composition evidence of marine ice transfer along the bottom of a small Antarctic ice shelf, *Geophys. Res. Lett., 18*(5), 849-852, 1991.

Souchez, R., and R. Lorrain, *Ice composition and glacier dynamics*, Springer-Verlag, Berlin, 1991.

Stephenson, S. N., and H. J. Zwally, Ice-shelf topography and structure determined using satellite-radar altimetry and landsat imagery, *Ann. Glaciol., 12,* 161-164, 1989.

Swithinbank, C., K. Brunk, and J. Sievers, A glaciological map of the Filchner-Ronne Ice Shelf, Antarctica, *Ann. Glaciol., 11,* 150-155, 1988.

Talbot, M. H., Oceanic environment of George VI Ice Shelf, Antarctic Peninsula, *Ann. Glaciol., 11,* 162-169, 1989.

Tison, J.-L., D. Ronveaux, and R. D. Lorrain, Low salinity frazil ice generation at the base of small antarctic ice shelf, *Antarct. Sci., 5*(3), 309-322, 1993.

Tison, J.-L., T. Thorsteinsson, R. D. Lorrain, and J. Kipfstuhl, Origin and development of textures and fabrics in basal ice at Summit, Central Greenland, *Earth Planet. Sci. Lett., 125,* 421-437, 1994.

Tison, J.-L., R. D. Lorrain, A. Bouzette, M. Dini, A. Bondesan, and M. Stiévenard, Linking landfast sea ice variability to marine ice accretion at the Hells Gate Ice Shelf, Ross Sea, *Antarctic Res. Ser., 74,* 375-407, 1998.

Turner, J. S., *Buoyancy effects in fluids,* Cambridge University Press, London, 1973.

Turner, J. S., Turbulent entrainment: the development of the entrainment assumption, and its application to geophysical flows, *J. Fluid Mech., 173,* 431-471, 1986.

UNESCO, International system of units (SI) in oceanography. Report of IAPSO working group on symbols and units, *UNESCO Technical Papers in Marine Science, 45,* 1985.

Untersteiner, N., Natural desalination and equilibrium salinity profile of perennial sea ice, *J. Geophys. Res., 73*(4), 1251-1257, 1968.

Vaughan, D. G., Relating the occurrence of crevasses to surface strain rates, *J. Glaciol., 39,* 255-266, 1993.

Vaughan, D. G., J. Sievers, C. S. M. Doake, H. Hinze, D. R. Mantripp, V. S. Pozdeev, H. Sandhager, H. W. Schenke, A. Solheim, and F. Thyssen, Subglacial and seabed topography, ice thickness and water column thickness in the vicinity of Filchner-Ronne-Schelfeis, Antarctica, *Polarforschung, 64*(2), 75-88, 1994.

Wadia, P. H., *Mass transfer from spheres and discs in turbulent agitated vessels, Ph.D. Thesis,* Massachusetts Institute of Technology, 1975.

Warren, S. G., C. S. Roesler, V. I. Morgan, R. E. Brandt, I. D. Goodwin, and I. Allison, Green icebergs formed by freezing of organic-rich seawater to the base of Antarctic ice shelves, *J. Geophys. Res., 98*(C4), 6921-6928, 1993.

Weeks, W. S., and G. Lofgren, The effective solute distribution coefficient during the freezing of NaCl solutions, In *Physics of snow and ice, Proceedings of the International conference on low temperature science,* vol. 1, edited by H. Oura, pp. 579-597, Inst. Low Temp. Sci., Hokkaido, 1967.

Weeks, W. S., and S. F. Ackley, *The growth, structure and properties of sea ice, CRREL monograph, 82-1,* 130 pp., U. S. Army Cold Reg. Res. Eng. Lab., Hanover, N. H., 1982.

Weertman, J., Bottom crevasses, *J. Glaciol., 25,* 185-188, 1980.

Williams, M. J. M., A. Jenkins, and J. Determann, Physical controls on ocean circulation beneath ice shelves revealed by numerical models, in *Ocean, ice, and atmosphere: interactions at the Antarctic continental margin, Antarct. Res. Ser.,* vol. 75, edited by S. S. Jacobs and R. F. Weiss, pp. 285-299, AGU, Washington, D. C., 1998.

Worster, M. G., and H. E. Huppert, Time-dependent density profiles in a filling box, *J. Fluid Mech., 132,* 457-466, 1983.

Zotikov, I. A., V. S. Zagorodnov, and J. V. Raikovsky, Core drilling through the Ross Ice Shelf (Antarctica) confirmed basal freezing, *Science, 207*(4438), 1463-1465, 1980.